(87)

Polarization Transfer Measurements of $D(\vec{e}, e'\vec{p})$ reaction in the dip region at $Q^2 = -0.31$ GeV^2/c^2

by

Kyungseon Joo

B.S., Physics
Seoul National University
February 1986
M.S., Computer and Electrical Engineering
University of Utah
June 1989

Submitted to the Department of Physics
in partial fulfillment of the requirements for the degree of

Doctor of Philosophy

at the

MASSACHUSETTS INSTITUTE OF TECHNOLOGY

June 1997

Signature of Author.....
Department of Physics
March 19, 1997

Certified by.....
William Bertozzi
Professor of Physics
Thesis Supervisor

Accepted by.....
Professor George F. Koster
Chairman, Physics Graduate Committee

Polarization Transfer Measurements of $D(\vec{e}, e'\vec{p})$ reaction in the dip region at $Q^2 = -0.31$ GeV^2/c^2

by

Kyungseon Joo

Submitted to the Department of Physics
on March 19, 1997, in partial fulfillment of the
requirements for the degree of
Doctor of Philosophy

Abstract

The recoil proton polarization from deuteron electrodisintegration via longitudinally polarized electrons was measured in the dip region at $Q^2 = -0.31$ GeV^2. In this kinematical region non-nucleonic effects are expected to be important. The protons were detected in the parallel kinematics with a recoil momentum of 100 MeV/c. In parallel kinematics, three response functions, $R^t_{LT'}$ $R^l_{TT'}$ and R^n_{LT} can be determined because each is proportional to a component of the recoil proton polarization. A focal plane polarimeter (FPP) at M.I.T.-Bates Laboratory was used in this polarization measurements in coincidence electron scattering.

Thesis Supervisor: William Bertozzi
Title: Professor of Physics

To my parents, wife and son

Contents

List of Figures

List of Tables

Chapter 1

Introduction

The strong interaction is the fundamental force underlying the dynamics of the nuclear constituents in the nuclear medium. It is believed that the strong interaction is described in the framework of Quantum Chromo-Dynamics (QCD), the fundamental quantum field theory, in which gluons act as the mediators of the interaction between the quarks, the alleged elementary constituents of baryons and mesons. In practice, it is very difficult to describe even the simplest nuclear system, the deuteron, a bound neutron-proton pair, starting from the basic principles of QCD. On the other hand, the conventional framework of nuclear physics, with nucleons, mesons, and isobar degrees of freedom, has been used as an effective theory to describe most of the experimental data on nuclear properties, and has been found quite appropriate up to a scale of energy of about 1 GeV. In order to gain knowledge on the dynamics and properties of the nuclear constituents in the nuclear medium, the conventional framework should first be developed as accurately and as comprehensively as possible. Then signatures of the underlying fundamental quark-gluon degrees of freedom might be identified and eventually interpreted in the framework of QCD.

Within the context of such fundamental investigations, the deuteron, the two-body system, is particularly well suited. In principle, exact non-relativistic calculations with relativistic corrections are available including meson exchange currents, internal degrees of freedom of the nucleon and final state interactions, although computational complications usually enforce the use of certain approximations. The deuteron serves, together with nucleon-nucleon (NN) scattering, as a basis for fixing any realistic model of the effective NN force. Once the force has been fixed, one can try to describe other properties of the two nucleon system. In this sense, the electrodisintegration of the deuteron has

provided very stringent constraints on understanding of nuclear structure of the bound two nucleon system. Since the character of the electromagnetic interaction is well understood, the electromagnetic properties of the deuteron can be expressed in terms of charge and current matrix elements.

The previous studies of electron scattering show that the quasifree nucleon processes are expected to be dominant for for large energy and momentum transfers, i.e., for energy transfers large compared with nuclear single particle energies ($\omega \geq 50$ MeV) and momentum transfers large compared with typical nuclear momenta ($|\vec{q}| \geq 100$ MeV/c). This idea is confirmed by the quasifree (QF) and Δ excitation peaks which are centered at approximately the energy loss for elastic scattering and Δ-excitation from unbound nucleons. Despite a success of the quasifree picture in providing basic framework, other reaction mechanisms have been recognized as having substantial strength. The introduction of spin observables to the study of the electron scattering opens up a new level of tests and constraints for modern nuclear theory. These spin observables involve the real and imaginary parts of amplitudes in different combinations and generate new sensitivities to features in the nuclear electromagnetic current. Polarization observables are manifested as asymmetries and therefore systematic errors can be substantially reduced compared to absolute cross section measurements. There is a new theoretical challenge with these new polarization observables since the expected results are more subtle than the estimation with simple models.

This thesis is organized as follows. Chapter 1 presents a general introduction and theory for this experiment. Chapter 2 describes the experimental apparatus and data acquisition system. Chapter 3 then details the data analysis procedures. Chapter 4 presents the results of the experiment and conclusions about the observed physics.

1.1 Electron Scattering

Electron scattering has proved to be a powerful tool for investigating the electromagnetic structure of nuclei and nucleons. In an electron scattering experiment the electrons are accelerated to a certain energy and scattered from the target of interest. The scattered particles are detected at particular angles and momenta. If no particles other than the scattered electron are detected, then the measurement is *inclusive* or *single arm*. If particles are detected in coincidence with the electron, then the measurement is *exclusive*

or *coincidence*. The experiment described in this thesis is an exclusive coincidence measurement since both the scattered electron and proton are detected. Electron scattering has been used for probing nuclear physics for the following reasons: [1]

1. The interaction of the electron with the nucleus is described by Quantum Electrodynamics (QED), a well understood and calculable theory. This feature allows the details of nuclear current J_μ, which is extremely complicated and not well understood, to be probed.
2. The electromagnetic interaction is relatively weak. This allows the interaction to be described by the Born (one-photon-exchange) approximation for the lighter nuclei ($Z\alpha \ll 1$). Because of the weakness of the interaction, the electron can probe the entire nuclear volume instead of primarily the nuclear surface as in hadron-nucleus scattering.
3. The 3-momentum transfer $\vec{q}$ and the energy transfer (ω) can be varied independently of each other subject to only the restriction that the exchanged virtual photon is spacelike ($Q^2 = \omega^2 - |\vec{q}|^2 < 0$). This freedom allows the $\vec{q}$ dependence of the transition matrix elements to be mapped out. By Fourier-transforming this map, the spatial distribution of the charge and current density of the nucleus under study can be determined. This is different from real photon absorption experiments where $\omega = |\vec{q}|$.

There are also disadvantages in electron scattering.

1. The fact that a high energy electron radiates in the presence of the target nuclei makes the analysis of electron scattering complicated. These radiative effects need to be unfolded so that the experimental results can be compared with theoretical predictions.
2. The weakness of the interaction implies that the cross section is small. The small cross section and correspondingly low counting rate can make coincidence experiments difficult.

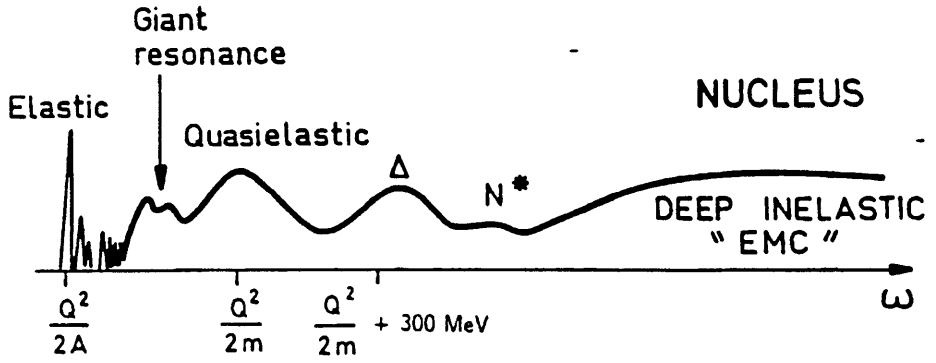

Figure 1-1: A typical inclusive electron scattering spectrum.

1.2 Inclusive Electron Scattering

A typical inclusive (e, e') spectrum is shown in Figure 1-1. This shows the cross section as a function of energy transfer ω for a fixed Q^2. Different regions of this spectrum can be associated with different physical processes. Starting at the lowest value of ω, the first peak is the elastic scattering peak where the nucleus is left in its ground state. Next are sharp peaks of inelastic electron scattering corresponding to discrete bound states. At larger ω a set of broad bumps is associated with collective modes of nuclear motion, called *the giant resonances.* Next is the quasielastic peak where the virtual photon interacts primarily with a single nucleon which is subsequently emitted from the nucleus. This peak, which would otherwise be a sharp peak, is spread out by Fermi motion of the nucleon. Next peaks correspond to the excitation of hadronic states such as Δ and the N^*. Between the quasielastic peak and the Δ peak is the *dip region* which is the kinematic region of this thesis. Beyond these peaks is the large region of Deep Inelastic Scattering (DIS). At this continuum area scattering from individual constituent quarks has been observed.

In the first Born (one-photon-exchange) approximation, the inclusive (e, e') cross section can be written as:

$$\frac{d^3\sigma}{d\varepsilon' d\Omega_e} = \frac{4\pi\sigma_M}{M_A}\left\{\frac{Q^4}{\vec{q}^4}R_L\left(|\vec{q}|,\omega\right) + \left(\frac{-Q^2}{2\vec{q}^2} + \tan^2\left(\frac{\theta_e}{2}\right)\right)R_T\left(|\vec{q}|,\omega\right)\right\}, \qquad (1.1)$$

where R_L and R_T are the longitudinal and transverse response functions, respectively, ε', Ω_e and θ_e is the energy, solid angle and angle of the detected electron. σ_M is the Mott cross section, given by

$$\sigma_M = \frac{\alpha^2 \cos^2(\theta_e/2)}{4\varepsilon^2 \sin^4(\theta_e/2)} , \tag{1.2}$$

where $\alpha \equiv 1/137$ and ε is the energy of the incident electron.

1.3 Coincidence Electron Scattering

In a coincidence or exclusive electron scattering experiment, a scattered particle is detected in coincidence with the scattered electron. This exclusive measurement allows the selection of a particular final state and, hence, a more detailed study of nuclear structure. The advantage of this study is that the experiment can be designed to be sensitive to a particular part of reaction mechanisms which restrict and clarify the possible theories.

1.3.1 Kinematics

The initial and final electron 4-momenta are denoted by $K^\mu = (\varepsilon, \vec{k})$ and $K'^\mu = (\varepsilon', \vec{k'})$, respectively.[1] The corresponding 4-momentum transfer is the difference between the initial and final electron 4-momenta:

$$Q^\mu = K^\mu - K'^\mu = (\omega, \vec{q}) = (\varepsilon - \varepsilon', \vec{k} - \vec{k'}) , \tag{1.3}$$

where ω is the energy transfer and $\vec{q}$ is the 3-momentum transfer. The initial target momentum is $P_A^\mu = (E_A, \vec{p}_A)$; the target is at rest in the laboratory frame, so that $\vec{p}_A = 0$ and $E_A = M_A$ is the mass of the target. The scattered proton has 4-momentum $P_p^\mu = (E_p, \vec{p}_p)$ and the residual nucleus (of mass M_X) has 4-momentum $P_X^\mu = (E_X, \vec{p}_X)$.

[1] The convention of the metric $g_{\mu\nu}$ where $g_{00} = +1$ and $g_{ij} = -\delta^i_j$. δ^i_j, the Kronecker delta symbol, equals 1 for $i = j$ and 0 otherwise. The product of two 4-vectors $A^\mu = (A^0, \vec{A})$ and $B^\mu = (B^0, \vec{B})$ is $A \cdot B \equiv A^\mu B_\mu = A^0 B^0 - \vec{A} \cdot \vec{B}$.

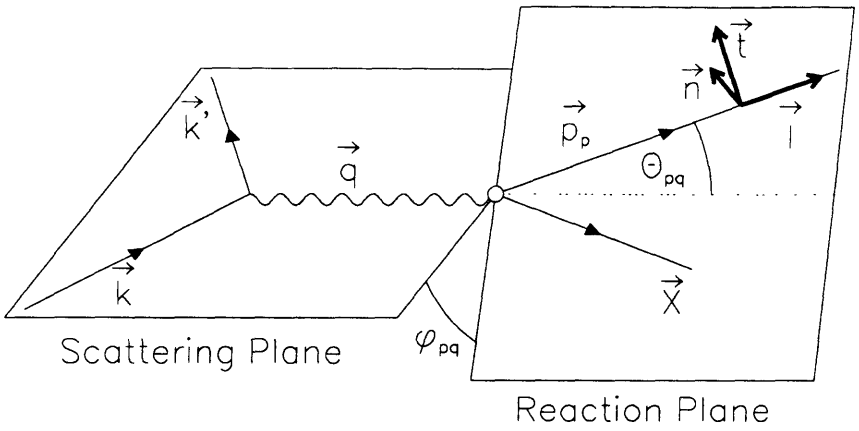

Figure 1-2: Diagram of the scattering and reaction planes for A$(e, e'p)$X. The final state polarization vectors are also shown. Both $\hat{l}$ and $\hat{t}$ are in the reaction plane while $\hat{n}$ is normal to the reaction plane. X is the residual system.

In Figure 1-2 the A$(\vec{e}, e'\vec{p})$X reaction is graphically displayed. The scattering plane is defined by the initial and final 3-momenta, $\vec{k}$ and $\vec{k'}$, and the reaction plane is defined by 3-momentum transfer, $\vec{q}$ and the scattered proton 3-momentum, $\vec{p}_p$. θ_{pq} is defined by the angle between the $\vec{q}$ and $\vec{p}_p$ while ϕ_{pq} is defined by the angle between the reaction plane and the scattering plane. An *in-plane* measurement is made when a proton is detected at $\phi_{pq} = 0°$or $180°$. A *parallel kinematics* measurement is made when a proton is detected at $\theta_{pq} = 0°$.

The recoil proton polarization is referred to a coordinate system defined with respect to the reaction plane. $\hat{l}$, is parallel to $\vec{p}_p$ and $\hat{n}$, is normal to the reaction plane in the direction of $\vec{q} \times \vec{p}_p$. For parallel kinematics in which $\vec{q}$ is parallel to $\vec{p}_p$, the normal component is defined to be normal to the scattering plane and pointing up. The transverse, or sideways, direction is defined as $\hat{t} = \hat{n} \times \hat{l}$, so that $\hat{t}$ lies in the reaction plane but is perpendicular to $\vec{p}_p$.

Some useful quantities can be defined for the analysis. 4-momentum conservation implies

$$Q^\mu + P_A^\mu = P_p^\mu + P_X^\mu \ . \tag{1.4}$$

Separating the 3-momentum and energy terms of Equation 1.4 gives

$$\vec{q} = \vec{p}_p + \vec{p}_X \tag{1.5}$$

$$\begin{aligned} \omega + M_A &= E_p + E_X \\ &= M_p + T_p + M_X + T_X \ , \end{aligned} \tag{1.6}$$

where M_p and M_X are the masses of the scattered proton and residual nucleus, respectively and T_p and T_X are the kinetic energies of the scattered proton and residual nucleus, respectively. Now the missing momentum $\vec{p}_m$ and missing energy E_m may be defined

$$\vec{p}_m \equiv \vec{p}_p - \vec{q} \tag{1.7}$$

$$\begin{aligned} E_m &\equiv M_p + M_X - M_A \\ &= E_p - T_p + E_X - T_X - M_A \\ &= \omega - T_p - T_X \ . \end{aligned} \tag{1.8}$$

For the $D(e, e'p)$ reaction, the target is the deuteron of mass M_D and the residual nucleus is the neutron of mass M_n. Then the missing energy E_m is

$$\begin{aligned} E_m &= M_p + M_n - M_D \\ &= \varepsilon_b \ , \end{aligned} \tag{1.9}$$

where $\varepsilon_b \approx 2.225\ MeV$ is the absolute value of the binding energy of the deuteron.

1.3.2 Born Approximation

The electromagnetic scattering process for light nuclei and high $\vec{q}$ can be approximated by assuming the one-photon-exchange approximation, or First Born approximation. A diagram of this process is shown in Figure 1-3. The general formalism of the $(\vec{e}, e'\vec{p})$ reaction is reviewed in detail by A. S. Raskin and T. W. Donnelly. [3]. A brief outline of their work for the derivation of the cross section including the effects of spin degrees of freedom is presented in this section. As shown in Figure 1-3, the spinors $u(K, S)$ and $\bar{u}(K', S')$ of initial and final electrons are labeled with the corresponding 4-momenta K and K' and spins S, and S'. The initial and final 4-momenta of the nucleus are

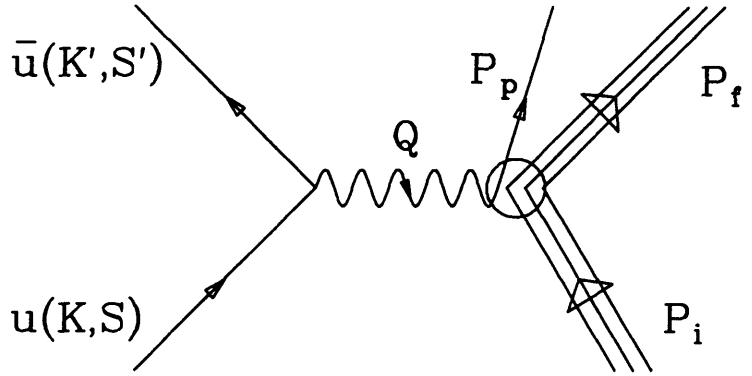

Figure 1-3: The One-Photon-Exchange $(e, e'p)$ Reaction

$P_i = (M_i, 0)$ and $P_f = (M_f, \vec{p}_f)$, respectively, while the 4-momentum of the exclusive proton is $P_p = (E_p, \vec{p}_p)$. Following Bjorken and Drell [2], the differential cross section in the laboratory frame is

$$\begin{aligned} d\sigma &= \frac{m_e}{\varepsilon}\overline{\sum_{if}} \mid \mathcal{M}_{fi}\mid^2 \frac{m_e}{\varepsilon'}\frac{d^3\vec{k}'}{(2\pi)^3}\frac{M_p}{E_p}\frac{d^3\vec{p}_p}{(2\pi)^3}\frac{M_f}{E_f}\frac{d^3\vec{p}_f}{(2\pi)^3} \\ &\quad \times(2\pi)^4\delta^4(K + P_i - K' - P_p - P_f), \end{aligned} \tag{1.10}$$

where the electrons are ultra-relativistic ($\beta = 1$) and $\overline{\sum}_{if}$ corresponds to the average over initial states and sum over final states. All of the particle states are assumed to be normalized to unity. [2] The invariant matrix element, $\mathcal{M}_{fi}$, corresponding to the given process is

$$\mathcal{M}_{fi} = \frac{ie}{Q^2} j_\mu(K', S'; K, S) J^\mu(P_p, P_f; P_i)_{fi}, \tag{1.11}$$

where the electron electromagnetic current, j_μ is given by

$$j^\mu(K', S'; K, S) = -e\bar{u}(K', S')\gamma^\mu u(K, S), \tag{1.12}$$

and J^μ is the nuclear electromagnetic transition current. Since the residual nucleus is assumed not to be detected, the integration over $\vec{p}_f$ must be performed. Then the integration over the scattered proton momentum, p_p is performed to get

$$\frac{d\sigma}{d\varepsilon' d\Omega_e d\Omega_{p_p}} = \frac{m_e^2 M_p M_f}{(2\pi)^2 M_i} \frac{k' p_p}{k} f_{rec}^{-1} \overline{\sum_{if}} \mid \mathcal{M}_{fi} \mid^2 , \tag{1.13}$$

where the recoil factor is

$$f_{rec} = \left| 1 + \frac{\omega p P - E_p q \cos\theta_{pq}}{M_i p_p} \right| . \tag{1.14}$$

Consider now the invariant matrix element, $\mathcal{M}_{fi}$. The square of the invariant matrix element is proportional to two second-rank tensors, a leptonic tensor, $\eta_{\mu\nu}(K', S'; K, S)$, and the hadronic tensor, $W_{\mu\nu}(Q)$:

$$\overline{\sum_{if}} \mid \mathcal{M}_{fi} \mid^2 = \frac{(4\pi\alpha)^2}{(Q^2)^2} \eta_{\mu\nu} W_{fi}^{\mu\nu} . \tag{1.15}$$

Then the differential cross section can be expressed as

$$\frac{d\sigma}{d\omega d\Omega_e d\Omega_p} = \frac{\alpha^2 m_e^2 M_f M_p}{2\pi^3 M_i} \frac{k' p_p}{k (Q^2)^2} f_{rec}^{-1} \eta_{\mu\nu} W_{fi}^{\mu\nu} . \tag{1.16}$$

The leptonic tensor, $\eta_{\mu\nu}$ which can be determined from QED, is

$$\eta_{\mu\nu} = \frac{1}{e^2} \frac{\varepsilon\varepsilon'}{m_e^2} \overline{\sum_{if}} j_\mu^* j_\nu , \tag{1.17}$$

$$= \overline{\sum_{if}} \left[\bar{u}(K, S) \gamma_\mu u(K', S') \right] \left[\bar{u}(K', S') \gamma_\nu u(K, S) \right] . \tag{1.18}$$

Considering only purely longitudinally polarized electrons and taking the ultra-relativistic limit where $\beta = 1$, the leptonic tensor, $\eta_{\mu\nu}$ becomes

$$\eta_{\mu\nu} = \frac{1}{4m_e^2}\left[K_\mu K'_\nu + K'_\mu K_\nu - g_{\mu\nu} K \cdot K' - ih\epsilon_{\mu\nu\alpha\beta}K^\alpha K'^\beta\right] , \tag{1.19}$$

where $h = \pm 1$, is the electron helicity and $\epsilon_{\mu\nu\alpha\beta}$ is the anti-symmetric tensor.

Similarly, the hadronic tensor $W_{\mu\nu}$ is constructed in terms of the nuclear electromagnetic current J_μ

$$W_{\mu\nu} = \overline{\sum_{spins} J^*_\mu J_\nu} . \tag{1.20}$$

The nuclear electromagnetic current, $J^\mu = (\rho, J^x, J^y, J^z)$ in Cartesian coordinate, can be expressed in a spherical basis. Choosing the z-direction along the direction of $\vec{q}$, the nuclear electromagnetic current can be decomposed into the longitudinal and transverse components via

$$J(0,\vec{q}) \equiv J^z(\vec{q}) \tag{1.21}$$

$$J(\pm 1,\vec{q}) \equiv \mp\frac{1}{\sqrt{2}}(J^x(\vec{q}) \pm iJ^y(\vec{q})) \tag{1.22}$$

From the continuity equation for the nuclear electromagnetic current,

$$Q_\mu J^\mu = \omega\rho(\vec{q}) - qJ(0,\vec{q}) = 0, \tag{1.23}$$

so that $J(0,\vec{q}) = (\omega/q)\rho(\vec{q})$; thus, the fact that the nuclear electromagnetic current is conserved implies that only three of the components of the 4-current J^μ are independent quantities.

After performing the contraction of the leptonic and hadronic tensors indicated in Equation 1.16, the differential cross section can be written as follows:

$$\begin{aligned}\frac{d^5\sigma}{d\Omega_e d\Omega_p d\omega} &= K\sigma_{Mott}\{(v_L\mathcal{R}_L + v_T\mathcal{R}_T + v_{TT}\mathcal{R}_{TT} + v_{LT}\mathcal{R}_{LT}) \\ &\quad + h(v_{LT'}\mathcal{R}_{LT'} + v_{TT'}\mathcal{R}_{TT'})\},\end{aligned} \tag{1.24}$$

where the L and T in the above subscripts refer to the longitudinal and transverse components of the virtual photon polarization, respectively and the L, T, LT and TT denote the longitudinal, transverse, longitudinal-transverse interference and the transverse-transverse interference terms respectively. The primed terms are helicity dependent. σ_{Mott} is the cross section for scattering from a structureless Dirac particle. The constant K is given

$$K = \frac{M_p M_f \; p_p}{8\pi^3 M_i} \; f_{rec}^{-1}. \tag{1.25}$$

The $v's$ are kinematic factors given by

$$\begin{aligned}
v_L &= \left(\frac{Q^2}{\vec{q}^2}\right)^2 \\
v_T &= -\frac{1}{2}\left(\frac{Q^2}{\vec{q}^2}\right) + \tan^2(\theta_e/2) \\
v_{LT} &= \frac{1}{\sqrt{2}}\left(\frac{Q^2}{\vec{q}^2}\right)\sqrt{\left(-\frac{Q^2}{\vec{q}^2}\right) + \tan^2(\theta_e/2)} \\
v_{TT} &= \frac{1}{2}\left(\frac{Q^2}{\vec{q}^2}\right) \\
v_{LT'} &= \frac{1}{\sqrt{2}}\left(\frac{Q^2}{\vec{q}^2}\right)\tan(\theta_e/2) \\
v_{TT'} &= \sqrt{\left(-\frac{Q^2}{\vec{q}^2}\right) + \tan^2(\theta_e/2)}\tan(\theta_e/2) \quad .
\end{aligned} \tag{1.26}$$

The response function $\mathcal{R}$'s are expressed in terms of the nuclear electromagnetic current via

$$\begin{aligned}
\mathcal{R}_L &= |\rho(\vec{q})|^2 \\
&= (q/\omega)^2 |J(0,\vec{q})|^2 \\
\mathcal{R}_T &= |J(+1,\vec{q})|^2 + |J(-1,\vec{q})|^2 \\
\mathcal{R}_{TT} &= 2\mathrm{Re}(J(+1,\vec{q})^* J(-1,\vec{q})) \\
\mathcal{R}_{LT} &= -2\mathrm{Re}[\rho(\vec{q})^*(J(+1,\vec{q}) - J(-1,\vec{q}))] \\
&= -2(q/\omega)\mathrm{Re}[J(0,\vec{q})^*(J(+1,\vec{q}) - J(-1,\vec{q}))] \\
\mathcal{R}_{LT'} &= -2(q/\omega)\mathrm{Re}[J(0,\vec{q})^*(J(+1,\vec{q}) + J(-1,\vec{q}))] \\
\mathcal{R}_{TT'} &= |J(+1,\vec{q})|^2 - |J(-1,\vec{q})|^2 \quad .
\end{aligned} \tag{1.27}$$

Each of the six response functions can be further separated into terms with different dependence on the out-of-plane angle, ϕ_{pq}, and on the spin components of the recoil proton, $\vec{\mathcal{S}}$. This separation is a property of the system under rotation about the momentum transfer vector in angular momentum space. There are 18 response functions for A$(\vec{e}, e'\vec{p})$X reaction:

$$\begin{aligned}
\mathcal{R}_L &= R_L + \mathcal{S}_n R_L^n \\
\mathcal{R}_T &= R_T + \mathcal{S}_n R_T^n \\
\mathcal{R}_{TT} &= \cos 2\phi_{pq} R_{TT} + \sin 2\phi_{pq} \mathcal{S}_l R_{TT}^l + \sin 2\phi_{pq} \mathcal{S}_t R_{TT}^t + \cos 2\phi_{pq} \mathcal{S}_n R_{TT}^n \\
\mathcal{R}_{LT} &= \cos \phi_{pq} R_{LT} + \sin \phi_{pq} \mathcal{S}_l R_{LT}^l + \sin \phi_{pq} \mathcal{S}_t R_{LT}^t + \cos \phi_{pq} \mathcal{S}_n R_{LT}^n \\
\mathcal{R}_{LT'} &= \sin \phi_{pq} R_{LT'} + \cos \phi_{pq} \mathcal{S}_l R_{LT'}^l + \cos \phi_{pq} \mathcal{S}_t R_{LT'}^t + \sin \phi_{pq} \mathcal{S}_n R_{LT'}^n \\
\mathcal{R}_{TT'} &= \mathcal{S}_l R_{TT'}^l + \mathcal{S}_t R_{TT'}^t \ , \qquad (1.28)
\end{aligned}$$

where the response functions R's are dependent on $\vec{q}$, ω, T_p and θ_{pq}, which are related as discussed in the previous section.

Regarding the recoil nucleon polarization, the cross section can be written in terms of the polarization vector [62]

$$\sigma\left(\vec{\mathcal{S}}\right) = \frac{\sigma_0}{2}\left(1 + \vec{P}\cdot\hat{\mathcal{S}} + h\vec{P}'\cdot\hat{\mathcal{S}}\right), \qquad (1.29)$$

where σ_0 is the unpolarized cross section, $\sigma_0 = \sigma(\vec{\mathcal{S}}) + \sigma(-\vec{\mathcal{S}})$, h is the electron beam helicity, $\vec{P}$ is the induced polarization vector of the nucleon and $\vec{P}'$ is the helicity dependent polarization vector of the nucleon. By comparing Equations 1.24 and 1.29, each of the polarization observables can be described in terms of kinematical factors, v's, and response functions, R's

$$\begin{aligned}
\sigma_0 P_n &= K\sigma_{Mott}\left[v_L R_L^n + v_T R_T^n + v_{LT} R_{LT}^n \cos\phi_{pq} + v_{TT} R_{TT}^n \cos 2\phi_{pq}\right] \\
\sigma_0 P_m &= K\sigma_{Mott}\left[v_{LT} R_{LT}^m \sin\phi_{pq} + v_{LT} R_{LT}^m \sin 2\phi_{pq}\right] \ ; \ m = l,\ t \\
\sigma_0 P_n' &= K\sigma_{Mott} v_{LT'} R_{LT'}^n \sin\phi_{pq} \\
\sigma_0 P_m' &= K\sigma_{Mott}\left[v_{LT'} R_{LT'}^m \cos\phi_{pq} + v_{TT'} R_{LT'}^m\right] \ ; \ m = l,\ t \ . \qquad (1.30)
\end{aligned}$$

For in-plane kinematics where the scattered proton is detected at $\phi_{pq} = 0°$or $180°$, Equation 1.30 simplifies to:

$$\begin{aligned}
\sigma_0 P_n &= K\sigma_{Mott}\left[v_L R_L^n + v_T R_T^n + v_{LT} R_{LT}^n \cos\phi_{pq} + v_{TT} R_{TT}^n \cos 2\phi_{pq}\right] \\
\sigma_0 P_m &= 0 \;;\; m = l,\, t \\
\sigma_0 P_n' &= 0 \\
\sigma_0 P_m' &= K\sigma_{Mott}\left[v_{LT'} R_{LT'}^m \cos\phi_{pq} + v_{TT'} R_{LT'}^m\right] \;;\; m = l,\, t \;. \qquad (1.31)
\end{aligned}$$

The fact that in in-plane kinematics, only the normal component of the recoil proton polarization is helicity independent, implies that all three components of recoil proton polarization can be separated in a single measurement, assuming a favorable spin precession angle. In addition, by making measurements on either side of $\vec{q}$, the even and odd contributions can be separated. In parallel kinematics where ϕ_{pq} is not well defined, azimuthal symmetry around $\vec{q}$ eliminates those response functions whose contributions to the observables depend on the orientation of the reaction plane, ϕ_{pq}, and also requires that $R_{LT}^n = R_{LT}^t$ and $R_{LT'}^n = -R_{LT'}^t$. Measurement of P_t' or P_l' ,therefore, yields $R_{TT'}^t$or $R_{LT'}^l$, respectively while the induced polarization P_n' yields R_{LT}^n.

1.4 Deuteron Electromagnetic Disintegration

The most systematic formalism of a non-relativistic model for deuteron electrodisintegration was developed in the late seventies and early eighties by Arenhövel and coworkers. [5, 6, 7] It can be used in conjunction with any standard parameterization of the NN interaction such as the Paris potential. [10] The calculation also includes the effects due to the final state interaction, meson exchange current and isobar configurations. It has been refined and extended to include polarization observables and relativistic corrections by Arenhövel et al. [8, 9] In this section, the basic ingredients of his framework are presented.

Arenhövel has determined the differential cross section in terms of five independent variables: energy transfer ω^{lab} in the laboratory frame, electron solid angle $\Omega_e^{lab} = (\theta_e^{lab}, \phi_e^{lab})$ in the laboratory frame and the solid angle $\Omega_{np}^{cm} = (\theta_{np}^{cm}, \phi_{np}^{cm})$. By specifying the direction the relative neutron-proton(np) momentum $\vec{p}_{np}^{\,cm}$ in the center of mass of

the final np state with z-axis along $\vec{q}^{\,cm}$, $\vec{p}_{np}^{\,cm}$ is defined by $\vec{p}_{np}^{\,cm} = (\vec{p}_p^{\,cm} - \vec{p}_n^{\,cm})/2$. The coincidence differential cross section is

$$\frac{d\sigma}{d\omega^{lab} d\Omega_e^{lab} d\Omega_{np}^{cm}} = \frac{\alpha}{2\pi^2}\frac{1}{Q^4}\frac{\varepsilon'}{\varepsilon}\sum_{\mu\mu',s,m,m_d} T_{sm,\mu' m_d}\,\rho_{\mu\mu'}\,T^*_{sm,\mu m_d}\ , \tag{1.32}$$

where ε and ε' are the initial and final electron energies in the laboratory frame, respectively, and α is the electromagnetic fine structure constant. The ρ's are components of the virtual photon polarization density matrix and functions of the electron kinematics only, and are given by

$$\begin{aligned}
\rho_L &\equiv \rho_{00} = \beta^2 Q^2 \tfrac{\xi^2}{2\eta}\ , & \rho_T &\equiv \rho_{11} = \tfrac{1}{2}Q^2\left(1+\tfrac{\xi}{2\eta}\right)\\
\rho_{LT} &\equiv \rho_{01} = \beta^2 Q^2 \tfrac{\xi}{\eta}\left(\tfrac{\xi+\eta}{8}\right)^{\frac{1}{2}}\ , & \rho_{TT} &\equiv \rho_{-11} = -Q^2\tfrac{\xi}{4\eta}\\
\rho_{LT'} &\equiv \rho'_{01} = \tfrac{1}{2}Q^2\left(\tfrac{\xi}{\eta}\right)^{\frac{1}{2}}\ , & \rho_{TT'} &\equiv \rho'_{-11} = \tfrac{1}{2}Q^2\left(\tfrac{\xi+\eta}{\eta}\right)^{\frac{1}{2}}\ ,
\end{aligned} \tag{1.33}$$

where

$$\beta = \frac{|\vec{q}^{\,lab}|}{|\vec{q}^{\,cm}|}\ , \quad \xi = \frac{Q^2}{(\vec{q}^{\,lab})^2}\ , \quad \eta = \tan^2\left(\frac{\theta_e}{2}\right)\ . \tag{1.34}$$

The T-matrix elements are related to the hadronic-current matrix elements by

$$T_{sm,\mu m_d} = -2\pi\left(\frac{1}{2}p_{np}^{cm} M\right)^{1/2}\langle sm_s|\hat{J}_\mu(\vec{q})|m_d\rangle\ . \tag{1.35}$$

where the initial state is characterized by the four-momentum of the virtual photon q_μ, its longitudinal ($\mu = 0$) and transverse ($\mu = \pm 1$) polarizations, and the deuteron spin projection m_d with respect to $\vec{q}^{\,lab}$. The final state is characterized by the relative np momentum $\vec{p}_{np}^{\,cm}$, the total spin s and its projection on $\vec{p}_{np}^{\,cm}$. The T-matrix elements depend on the direction of $(\theta_{np}^{cm},\ \phi_{np}^{cm})$ of the relative momentum of the final np state. The dependence on ϕ_{np}^{cm} can be separated:

$$T_{sm,\mu m_d}\left(\theta_{np}^{cm}, \phi_{np}^{cm}\right) = e^{i\mu\phi_{np}^{cm}} t_{sm,\mu m_d}\left(\theta_{np}^{cm}\right)\ , \tag{1.36}$$

where the *reduced* t-matrix depends only on θ_{np}^{cm} in addition to energy and momentum transfer.

Using equations 1.36, the expression for the differential cross section of Equation 1.32 becomes

$$\begin{aligned}\frac{d\sigma}{d\omega^{lab}d\Omega_e^{lab}d\Omega_{np}^{cm}} &= C\{\ \rho_L\,(f_L+g_L^y)+\rho_T\,(f_T+g_T^y)\\ &+\ \rho_{LT}\,[(f_{LT}+g_{LT}^y)\,cos\phi_{np}+(g_{LT}^x+g_{LT}^z)\,sin\phi_{np}]\\ &+\ \rho_{TT}\,[(f_{TT}+g_{TT}^y)\,cos2\phi_{np}+(g_{TT}^x+g_{TT}^z)\,sin2\phi_{np}]\\ &+\ h\rho'_{LT}\,[(f'_{LT}+g_{LT}^{\prime y})\,cos\phi_{np}+(g_{LT}^{\prime x}+g_{LT}^{\prime z})\,sin\phi_{np}]\\ &+\ h\rho'_{TT}\,(f'_{TT}+g_{TT}^{\prime z})\}\ ,\end{aligned} \tag{1.37}$$

where the factor C is a function of the electron kinematics,

$$C=\frac{\alpha}{6\pi^2}\frac{1}{Q^4}\frac{\varepsilon'}{\varepsilon}\ . \tag{1.38}$$

The response function f's can be given in terms of t-matrix elements

$$\begin{aligned}f_L\equiv f_{00} &= \sum_{s,m,m_d} t_{sm,0m_d}t^*_{sm,0m_d}\\ f_T\equiv f_{11} &= 2\sum_{s,m,m_d} t_{sm,1m_d}t^*_{sm,1m_d}\\ f_{LT}\equiv f_{01} &= 4\ \mathrm{Re}\sum_{s,m,m_d} t_{sm,0m_d}t^*_{sm,1m_d}\\ f_{TT}\equiv f_{11} &= \sum_{s,m,m_d} t_{sm,-1m_d}t^*_{sm,1m_d}\\ f_{LT'}\equiv f'_{01} &= 4\ \mathrm{Im}\sum_{s,m,m_d} t_{sm,0m_d}t^*_{sm,1m_d}.\end{aligned} \tag{1.39}$$

The polarization response function g's are defined in terms of p-functions by

$$\begin{aligned}g_{\mu\nu}^{x/y} &= -\sqrt{2}\frac{1+\delta_{\mu+\nu,1}}{1+\delta_{\nu0}}\ \mathrm{Im}\left(p_{\mu\nu}^{1}\mp p_{\mu\nu}^{-1}\right)\\ g_{\mu\nu}^{\prime x/y} &= -\sqrt{2}\frac{1+\delta_{\mu+\nu,1}}{1+\delta_{\nu0}}\ \mathrm{Re}\left(p_{\mu\nu}^{1}\mp p_{\mu\nu}^{-1}\right)\\ g_{\mu\nu}^{z} &= 2(1+\delta_{\nu0})\ \mathrm{Im}\left(p_{\mu\nu}^{0}\right)\\ g_{\mu\nu}^{\prime z} &= 2(1+\delta_{\nu0})\ \mathrm{Re}\left(p_{\mu\nu}^{0}\right)\end{aligned} \tag{1.40}$$

with $(\mu,\nu) = (0,0)$, $(1,1)$, $(0,1)$, *and* $(-1,1)$ corresponding to L, T, LT *and* TT and the p-functions are given by

$$p^{\lambda}_{\mu\mu'} = \sum_{s,m,m_d} t_{sm,\mu' m_d} t^{*}_{sm,\mu m_d} \langle s m_s | \hat{\sigma}_{\lambda} | s m_s \rangle \quad . \tag{1.41}$$

The coordinate system to which the polarization components refer in the center of mass of the final np state has its z-axis along the relative np momentum $\vec{p}^{\,cm}_{np}$ and y-axis parallel to $\vec{q} \times \vec{p}^{\,cm}_{np}$. The response function f's and g's contain all the information on the dynamics of the two-nucleon system.

It is instructive to separate the electron helicity dependent part from the polarization response functions:

$$\frac{d\sigma}{d\omega^{lab} d\Omega_e^{lab} d\Omega_{np}^{cm}} P_j = S_0 \left(P_j^0 + h P_j' \right) \quad ; \; j = x,\; y,\; z \; , \tag{1.42}$$

where

$$P^0_{x/z} = \frac{C}{S_0} \left(\rho_{LT} g^{x/z}_{LT} sin\phi_{np} + \rho_{TT} g^{x/z}_{TT} sin2\phi_{np} \right) \tag{1.43}$$

$$P^0_{y} = \frac{C}{S_0} \left(\rho_{L} g^{y}_{L} + \rho_{T} g^{y}_{T} + \rho_{LT} g^{y}_{LT} cos\phi_{np} + \rho_{TT} g^{y}_{TT} cos2\phi_{np} \right) \tag{1.44}$$

$$P'_{x/z} = \frac{C}{S_0} \left(\rho'_{LT} g'^{x/z}_{LT} cos\phi_{np} + \rho'_{TT} g'^{x/z}_{TT} \right) \tag{1.45}$$

$$P'_{y} = \frac{C}{S_0} \rho'_{LT} g'^{y}_{LT} sin\phi_{np} \tag{1.46}$$

and $S_0 = C \left(\rho_L f_L + \rho_T f_T + \rho_{LT} f_{LT} cos\phi_{np} + \rho_{TT} f_{TT} cos2\phi_{np} \right)$.

As discussed in the previous section, in in-plane kinematics where $\phi_{np} = 0$, P_y is the only non-vanishing component of recoil proton polarization for an unpolarized electron beam. For polarized electron beam, $P'_{x/z}$ survive in in-plane kinematics. It may also noted that if the final state interaction were switched off, the polarization response functions $g^x_{\mu\nu}$, $g^y_{\mu\nu}$ and $g^z_{\mu\nu}$ would be identically zero because of Watson's theorem according to which the reduced t-matrix must be real. For these response functions, the final state

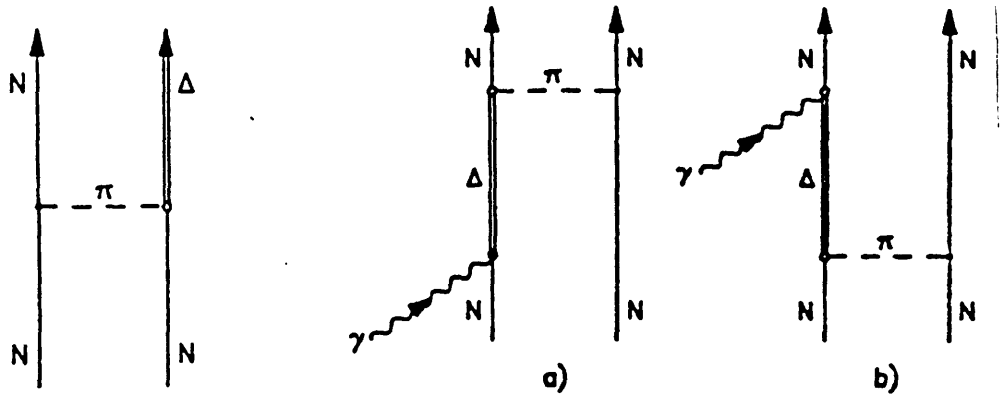

Figure 1-4: Feynman diagrams for isobar configuration contributions to nuclear current.

interaction becomes important. On the other hand, $g'^{x}_{\mu\nu}$, $g'^{y}_{\mu\nu}$ and $g'^{z}_{\mu\nu}$ would not vanish even if final state interactions were switched off.

In the model developed by Arenhövel, the nucleon-nucleon system is described in a non-relativistic framework. The wave function for the bound state deuteron is calculated using the non-relativistic Schrödinger equation and a realistic model of the nucleon-nucleon (NN) potential, *e.g.* the Paris [10] and Bonn [11] Potentials. The nuclear current density can be expanded in terms of Coulomb and transverse electric and magnetic multipoles. To evaluate the multipole moments, the explicit expressions for the various contributions to the nuclear current are needed. The charge and current densities are taken to be the non-relativistic one-body charge and current densities including nucleon form factors. Note that explicit terms of order $1/M$ are only included in the nucleonic current $\vec{j}$, while a relativistic correction of order $1/M^2$ is included in the nucleon form factors. Correspondingly, the response functions can be expressed in terms of the multipole moments. In practical computations of the t-matrix, these multipole expansions are truncated at a cutoff angular momentum L_{max} assuming that the contributions from higher order terms are small. To account for final state interactions, the final np state wave function is calculated using the same NN potential used to find the bound state wave function. Final state interactions (FSI) are included up to L_{max} partial waves, while all higher partial waves are calculated in the First Born Approximation. To account for internal nucleon degrees of freedom in the form of isobar configurations (IC), several types of transition currents, e.g. transition NN^* and N^*N^* currents are included as shown in Figure 1-4. [5, 12] In the non-relativistic limit, the transition current for $N\Delta$ is

given by

$$\rho^{N\Delta} = \frac{i}{4MM_\Delta} G_M^{N\Delta} (\vec{\sigma}_{N\Delta} \times \vec{q}) \cdot \vec{P} \tag{1.47}$$

$$\vec{j}^{N\Delta} = \frac{i}{4} \frac{M + M_\Delta}{MM_\Delta} G_M^{N\Delta} \vec{\sigma}_{N\Delta} \times \left(\vec{q} - \frac{M_\Delta - M}{M_\Delta + M} \vec{P} \right) , \tag{1.48}$$

where M and M_Δ are the nucleon and $\Delta(1232)$ masses, respectively, $\vec{\sigma}_{N\Delta}$ is a transition spin operator, and $\vec{P}$ is the sum of the nucleon and Δ momenta. The transition form factor $G_M^{N\Delta}$ is given by

$$G_M^{N\Delta} = \tau_3^{N\Delta} \frac{2M_\Delta}{M_\Delta + M} \frac{2}{\sqrt{3}} 1.3 G_M^p , \tag{1.49}$$

where $\tau_3^{N\Delta}$ is the third component of a transition isospin operator.
For $\Delta\Delta$,

$$\rho^{\Delta\Delta} = G_E^{\Delta\Delta}, \tag{1.50}$$

$$\vec{j}^{\Delta\Delta} = \frac{i}{2M_\Delta} \left(G_E^{\Delta\Delta} \vec{P} + i G_M^{\Delta\Delta} (\vec{\sigma}_{\Delta\Delta} \times \vec{q}) \right) , \tag{1.51}$$

where $\vec{\sigma}_{\Delta\Delta}$ is a transition spin operator. The transition form factor $G_{E/M}^{\Delta\Delta}$ is given by

$$G_{E/M}^{\Delta\Delta} = \frac{1}{2} \left(1 + \tau_3^{\Delta\Delta} \right) G_{E/M}^p . \tag{1.52}$$

Similar components of the nuclear current are included to account for $NN^*(1470)$ and $N^*(1470)N^*(1470)$configurations. Detailed expressions for the resulting matrix elements can be found in References. [13, 14]

With respect to meson exchange currents (MEC), only the lowest order terms are included as shown in Figure 1-5. In this order a two-body contribution to the nuclear current $\vec{j}$ is only considered and the charge density is not affected. The π-exchange current has the longest range and gives the dominant contribution to meson exchange currents (MEC) in the kinematics range which are considered in this thesis. To estimate effects of heavier meson exchange currents, the one-boson-exchange (OBE) potential model for

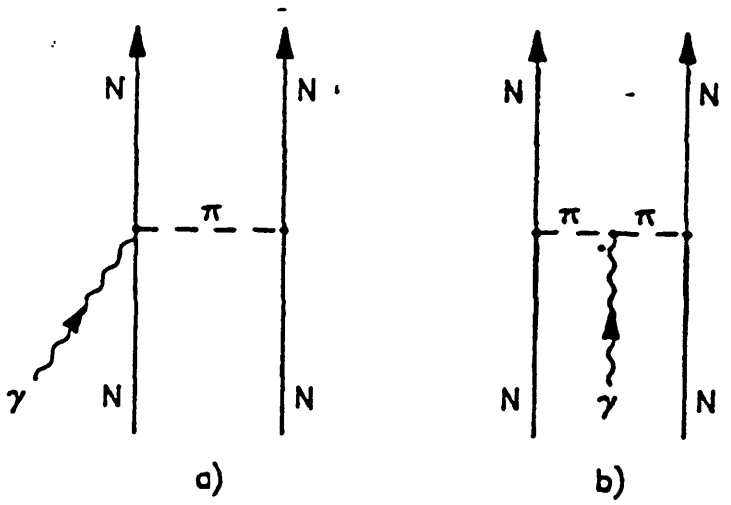

Figure 1-5: Feynman diagrams for meson exchange current processes.

contributions from ρ- and ω-exchange currents, is considered. Explicit expressions for the π, ρ and ω exchange currents can be found in Reference. [5]

The effects of relativistic corrections (RC) are included in the form of a lowest-order corrections by starting from a non-relativistic description. Although this method is a more limited and more phenomenological way than a fully relativistic method, it can be applied to more complex nuclei where a full relativistic description is not feasible. The influence of relativistic corrections is discussed in more detail in References. [15, 16]

1.5 The experiment

A Focal Plane Polarimeter (FPP) was installed in the One Hundred Inch Proton Spectrometer (OHIPS) at MIT-Bates to study the recoil proton polarization in $(\vec{e}, e'\vec{p})$ reactions. A series of measurements have been made to address a range of issues in nuclear physics including the structure of the nucleon (both its elastic and inelastic states), the few body system, and complex nuclei. The following is the summary of the experiment (88-21) performed at the MIT-Bates Linear Accelerator Center in Middleton, Massachusetts and completed in May of 1995.

- $H(\vec{e}, e'\vec{p})$: Q^2 of -0.38 GeV^2/c^2 and -0.50 GeV^2/c^2. The ratio of G_E/G_M for the proton is determined in these experiments by measuring the recoil proton polarization. [17]

- $D(\vec{e}, e'\vec{p})$: Q^2 of -0.38 GeV^2/c^2 and -0.50 GeV^2/c^2. The recoil protons were detected at on the quasieleastic peak and in parallel kinematics at p_r=0. To test the validity of the quasifree hypothesis and the impulse approximation at these kinematics, a comparison of spin coefficients from hydrogen were made with those from deuteron. [18]

- $D(\vec{e}, e'\vec{p})$: Q^2 of -0.38 GeV^2/c^2. The recoil protons were detected on the quasieleastic peak but in perpendicular kinematics at p_r=100 MeV/c. [19]

- $D(\vec{e}, e'\vec{p})$: Q^2 of -0.31 GeV^2/c^2. The recoil protons were detected in the dip region and in parallel kinematics at p_r=100 MeV/c.

This thesis describes the last experiment, a measurement of the recoil proton polarization in deuteron electrodisintegration via longitudinally polarized electrons in the dip region at $Q^2 = -0.31$ GeV^2/c^2. Electrons of incident energy 579 MeV were scattered at an angle of 80.0°. The momentum transfer ($\vec{q}$) was 613 MeV/c and energy transfer (ω) was 248 MeV. Scattered protons of momentum 713 MeV/c were detected at an angle of 32.0° in the parallel kinematics with a recoil momentum of 100 MeV/c. The recoil proton polarization was also measured using a Focal Plane Polarimeter (FPP).

The electron kinematics of this experiment correspond to the *dip region* between the quasielastic and Δ peaks. The origin of excess strength observed in this region by inclusive (e, e') experiments for various targets has not been well understood in electromagnetic nuclear physics. Theoretical attemps to predict the cross section, based on the reaction processes of quasielastic nucleon knockout, Δ production, meson exchange currents and coherent pion production have been insufficient to explain the data. [20, 21, 22] The ratio of transverse and longitudinal response functions does not agree with quasifree expectations for ^{12}C. [23] In contrast to longitudinal response, the transverse response shows considerable additional strength well beyond the s-shell knockout peak, characteristic of non-quasifree processes. Consequently, it is clear that two-body, and possibly many body, effects must come into play. These may be associated with nuclear ground state correlations not contained in the mean field picture, with final state interactions (FSI), or explicit involvement of sub-nucleonic degrees of freedom. The measurement

of the electrodisintegration of the deuteron in this kinematic region will provide a basic foundation for understanding these missing strengths.

The measurement of all three components of the recoil proton polarization is detailed in this thesis. A brief introduction to the Focal Plane Polarimeter (FPP) is discussed in the following section.

1.5.1 The Focal Plane Polarimeter

The recoil proton polarization is measured by a secondary scattering of the proton. A proton knocked out from the nuclear target by the primary electron scattering, traverses the spectrometer to the focal plane. At the focal plane, the proton is scattered from the carbon nuclei in graphite blocks in the polarimeter. The spin-orbit force in the nucleon-nucleon interaction produces the asymmetry which is proportional to the transverse components of the recoil proton polarization. The ability of the secondary scattering to measure the recoil proton polarization is defined by its analyzing power, A_y. Distribution of the secondary scattering in the polar angle, θ_{scat} is shown in Figure 1-6. At small angles, $\theta_{scat} \leq 5°$, most events from the secondary scattering come from Coulomb scattering which has zero analyzing power. Nuclear scattering events which have a large analyzing power occur for a wide range of polar scattering angles. An empirical fit for the analyzing power A_y in the polar angle of secondary scattering angle, θ_{scat}, is shown in Figure 1-7.

Only polarization components which are perpendicular to the proton's motion, can be determined by the polarimeter at the focal plane. If the spin of the proton precesses due to spectrometer magnetic fields between the target and the focal plane, however, three polarization components at the target can be extracted by flipping the helicity of the polarized electron. More details on the analysis of the recoil proton polarization will be discussed in Chapter 3.

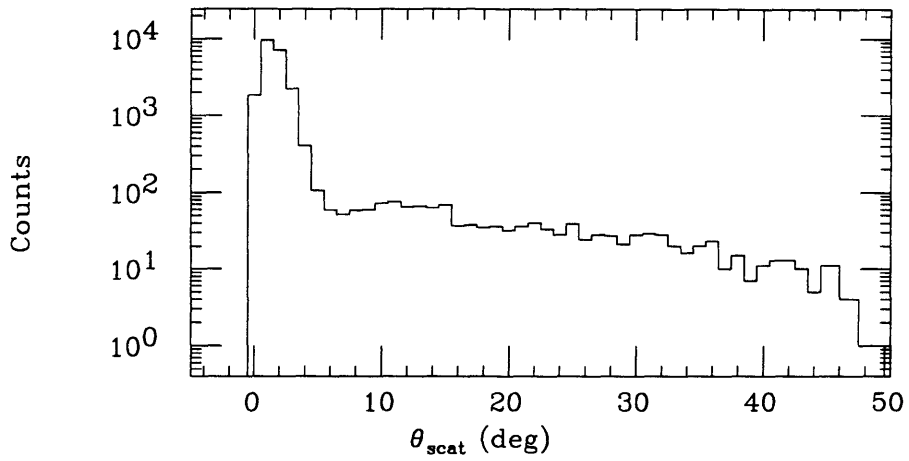

Figure 1-6: Distribution of events in the polar angle of secondary scattering angle, θ_{scat}, in FPP. Note that the vertical axis is a logarithmic scale.

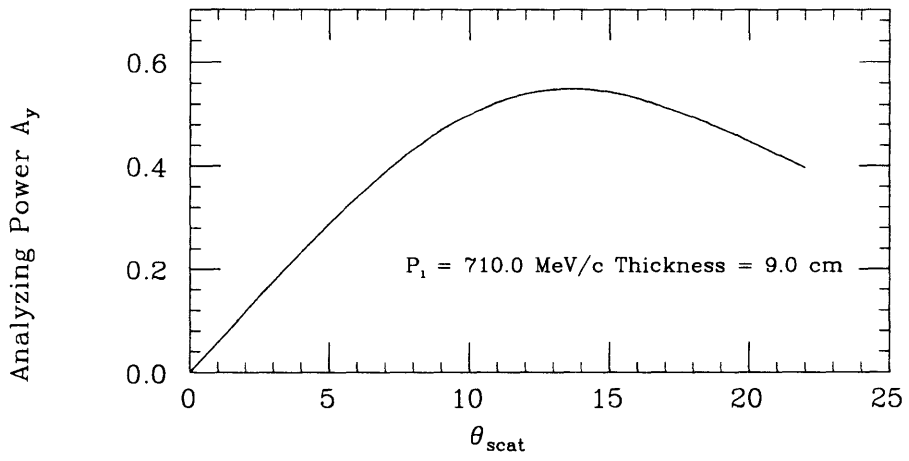

Figure 1-7: Empirical fit for the analyzing power A_y in the polar angle of secondary scattering angle, θ_{scat}. Fit parameter is taken from Reference [54]

Chapter 2

Experimental Setup

This experiment was performed on B-line in the South Hall of the M.I.T.-Bates Linear Accelerator Center, in Middleton, Massachusetts during May, 1995. A polarized electron was scattered off a liquid deuteron target and the scattered electron was detected in coincidence with the recoil proton. The recoil proton polarization was also measured. The Medium Energy Pion Spectrometer (MEPS) was used to detect the scattered electron, the One Hundred Inch Proton Spectrometer (OHIPS) to detect the recoil proton, and the OHIPS Focal Plane Polarimeter (FPP) to measure the recoil proton polarization. The electron beam polarization was measured by the B-line Møller polarimeter.

This chapter will describe the experimental setup that was used for this experiment, including the accelerator, the polarized electron source, and Møller polarimeter, the target system, the MEPS and OHIPS spectrometers, and the OHIPS Focal Plane Polarimeter (FPP). It will also describe the data acquisition electronics and software.

2.1 Accelerator

An overview of the M.I.T.-Bates Accelerator Center is given in Figure 2-1. The accelerator was designed to deliver a 1% duty factor and 40% longitudinally polarized electron beam with energies up to 1 GeV and currents up to 50 μA. It is currently being upgraded to be capable of deliver a continuous beam (near 85% duty factor) with internal target capabilities by using of a stretcher ring. This experiment used polarized electrons of

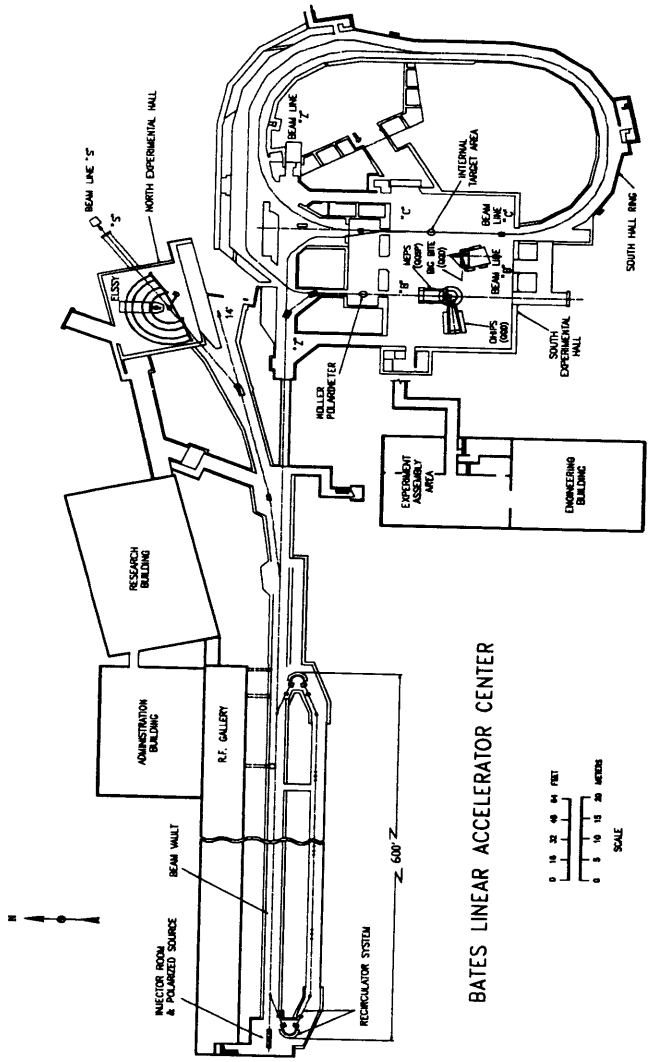

Figure 2-1: The M.I.T.-Bates Linear Accelerator Center, Middleton MA

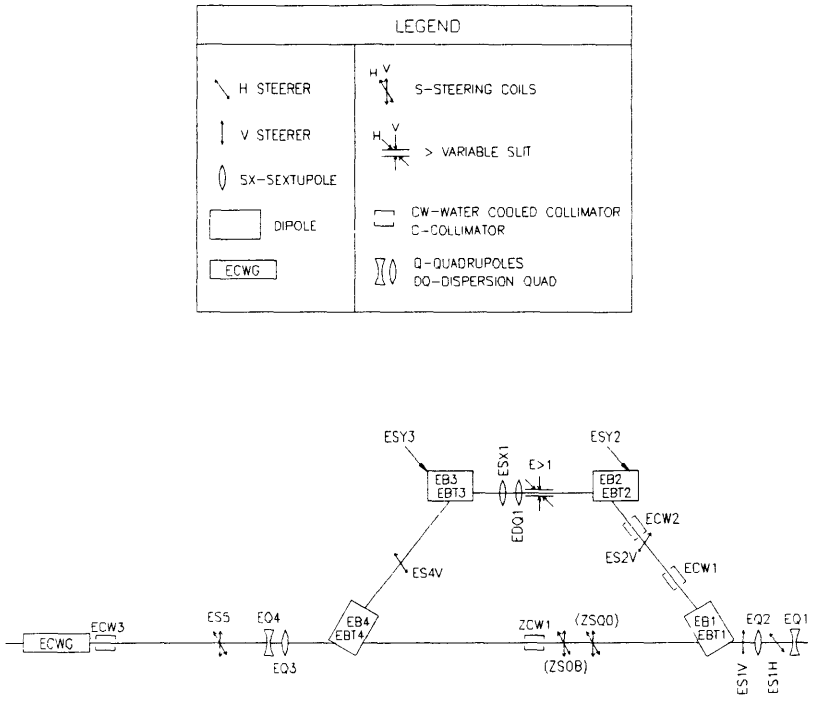

Figure 2-2: Schematic of the Energy Compression System.

approximately 580 MeV at a nominal average current of 17μA with a typical pulse width of 14μs and a pulse repetition rate of 600 Hz.

The accelerator section starts with a 360 keV injector producing beam pulses and the injector is followed by a series of cavities to boost the energy of electron beam to a maximum of approximately 500 MeV. For energies larger than 500 MeV, the beam is *recirculated* by being rerouted through the linear accelerator a second time to the maximum energy of approximately 1 GeV. This experiment used the recirculator. After the accelerator section, the electrons enter the Energy Compression System (ECS) which consists of 4 dipole magnets, an energy defining slit and a RF cavity as shown in Figure 2-2. The ECS reduces the energy spread of the beam while defining the beam energy up to the 0.3% level. After the ECS section, the beam enters the beam switch yard where the beam is transported to either South Hall (B-line), the 14°area (also used as a beam dump) or the North Hall (S-line). This experiment was performed on the B-line in the South Hall.

The beam current is monitored using three beam toroids, BT1, BT2 and BT3. BT1 is located at the beam entrance to the South Hall, and BT2 and BT3 are positioned just before the target chamber. The signals from BT1 and BT2 which are inhibited during the dead time of the experiment, are measured on a burst-by-burst basis. The signal from BT3 is sent to a Brookhaven Instruments Co. (BIC) charge integrator. This signal is not inhibited and therefore measures the total charge delivered by the accelerator.

The position and size of the beam can be visually monitored by the beryllium-oxygen (BeO) flip target that is removed during data taking, located 1 m upstream from the target chamber. The beam position and halo are recorded for each live burst by the beam position monitors (BPM) and photo-multiplier tubes (PMT). One BPM and PMT are upstream of the target chamber. The other BPM and PMT are upstream of the Møller Polarimeter. These BPMs can measure the vertical and horizontal position of the electron beam with a 1 mm resolution.

2.2 Polarized Electron Source

The polarized electron source used for this experiment is based on the design from the SLAC. [25] Basically, it utilizes the photoemission of polarized electrons from a GaAs crystal. GaAs has two very important properties that make it useful as a polarized electron source.

1. Its band structure permits a given spin state to be preferentially pumped into the conduction band.
2. Its surface can be treated to develop a negative work function (so called *negative electron affinity*).

The band gap between the energy maximum of the valence band and energy minimum of conduction band is $E_g = 1.52$ eV. The electron wave function has S symmetry at the minimum of the conduction band and P symmetry at the maximum of the valence band. The spin-orbit splitting of the valance band of GaAs makes the otherwise degenerate P state to be split into the four-fold degenerate $P_{3/2}$ states and the two-fold degenerate $P_{1/2}$ states which are located lower in energy by an amount $\Delta = 0.34$ eV. For circularly

polarized light, the selection rules require that $\Delta m_j = +1$ for the positive helicity and $\Delta m_j = -1$ for the negative helicity.

Assume that a circularly polarized photon of positive helicity is incident upon a GaAs crystal. If the photon energy E_γ is in the range $E_g \leq E_\gamma \leq E_g + \Delta$, then the transitions can only be allowed from $P_{3/2}$ states to $S_{1/2}$ states. There are two possible transitions

$$m_j = -3/2 \; in \; P_{3/2} \longrightarrow m_j = -1/2 \; in \; S_{1/2}$$
$$m_j = -1/2 \; in \; P_{3/2} \longrightarrow m_j = +1/2 \; in \; S_{1/2}$$

as shown in Figure 2-3. In the first case, the spin of emitted electron is antiparallel to the incident photon direction (or parallel to its emitted direction). In the second case, it is parallel to the incident photon direction (or antiparallel to its emitted direction). The calculation of Clebsch-Gordon coefficients for two cases shows that the transition probability of the first case is three times more likely than that of the second case such that

$$P = \frac{3-1}{3+1} = 50\% \; , \tag{2.1}$$

where P is the spin polarization of the emitted electrons for a circularly polarized photon of positive helicity. A very important feature of this process for a polarized electron source is the ease of polarization reversal. The helicity of the incident photon can be easily reversed external to the system such that no parameter of the electron beam is changed except the spin polarization direction. More details on the principle of the GaAs source can be found in Refrence [26].

In order to make a polarized electron source, polarized electrons in the conduction band, which are created with circularly polarized photons, must leave a GaAs crystal. In normal GsAs, the energy gap from the bottom of the conduction band to the free electron state is about 2.5 eV. By treating the surface of GaAs with Cs and NF_3, the energy gap from the bottom of the conduction band to the free electron state decreases below zero, so that a *negative electron affinity* is developed. The typical quantum efficiencies [1] were in the range $0.5\% \sim 2.0\%$ for polarized electron production in this experiment.

[1]The definition of quantum efficiency is the probability that an electron is emitted when a photon is incident upon the photocathode surface.

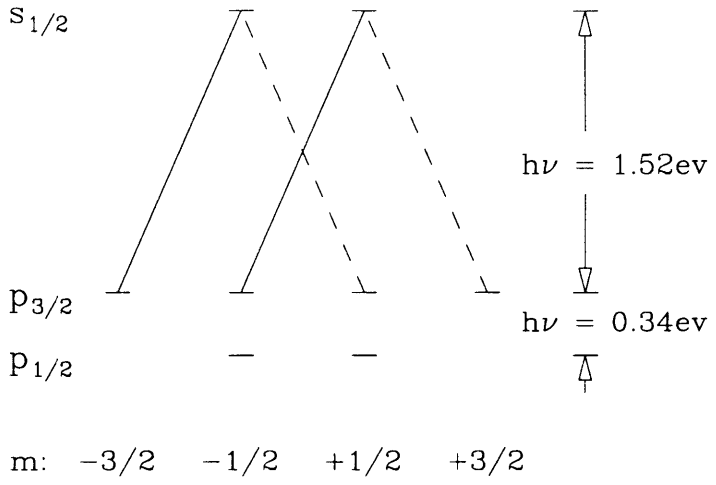

Figure 2-3: Allowed Transitions in GaAs. The solid (dashed) lines indicate allowed transitions for circularly polarized photon of positive (negative) helicity.

A Ti-sapphire crystal laser driven by an argon laser, delivers a continuous beam up to 9 W at about 750 nm. The intensity of this light is modulated by a special electro-optical device called a Pockels cell which rapidly rotates the axis of linear polarization by 90°in response to an externally applied high voltage. In this way, the pulsed beam is obtained whose pulse width and repetition rate can be controlled electronically to match the requirements of the experiment. The typical pulse width is $\sim 15\mu s$ and the repetition rate is 600 Hz. The pulsed beam is circularly polarized with either positive helicity or negative helicity when it passes a second Pockels cell, depending on the polarity of the applied high voltage. This circularly polarized light is incident on a GaAs crystal which is placed in an ultra-high vacuum (10^{-14} atm) in a Faraday cage. The electrons photo-emitted from a GaAs crystal are pre-accelerated by an electrostatic field to 360 keV and are longitudinally polarized. The polarized electron source is shown in Figure 2-4.

The helicity is selected randomly on a pulse by pulse basis. For operating the accelerator with the polarized source, the accelerator is phase-locked to the frequency of 60 Hz. To eliminate any correlation between the helicity and time dependent properties of the accelerator, the helicity selection is done in a quasi-random fashion. For accelerator operation at a repetition rate of 600 Hz, the helicity of beam pulse is selected randomly

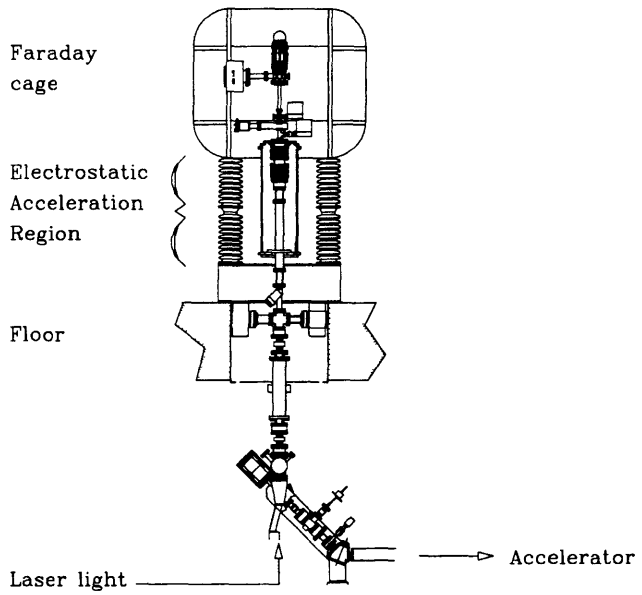

Figure 2-4: A Diagram of the Polarized Electron Source and Injector.

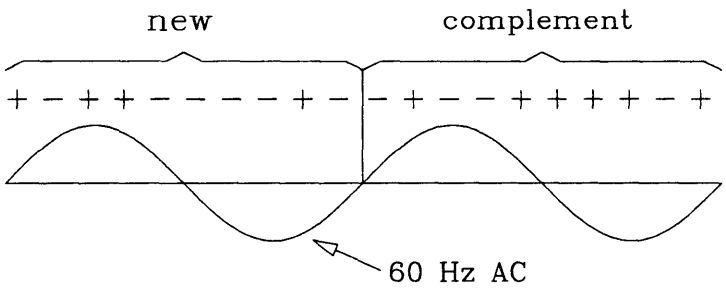

Figure 2-5: A selection of helicity sequence.

in each of the first ten pulses, then chosen to be the opposite helicity of those values for the next 10 pulses. For example, as shown in Figure 2-5, if the first 10 random order is chosen as *new*, then the next ten pulses would have the helicities as *complement.*

For this experiment, the beam energy is chosen to provide longitudinally polarized electrons at the target after spin precession through bending magnets along the beam transport line. Since a recirculator is used in this experiment, the spin precession comes from the 360° bend of the recirculator and the 90° bend of the switching magnet that directs the beam into the B line of the South Hall as shown in Figure 2-6. The spin precession angle θ with respect to the momentum of the electron can be found for a given bend angle, θ_{bend}

$$\theta = \frac{g-2}{2}\gamma\theta_{bend} \ . \tag{2.2}$$

Note that γ is the relativistic factor, E/m_e and g is the Lande g factor for the electron magnetic dipole moment where $g/2 - 1 = 1.1596\times10^{-3}$. Electrons from the polarized source are accelerated to $E_0 = 20$ MeV before entering the main accelerating section of variable energy impulse E_1. If the electron undergoes acceleration to an energy $E_1 + E_0$ during the first pass through the linac, then it gains an additional energy of E_1 during the second pass so that the total spin precession is

$$\theta = \frac{g-2}{2m_e}\left(\frac{E_1+E_0}{2}\right)2\pi + \frac{g-2}{2m_e}E_{inc}\,\frac{\pi}{2} \ , \tag{2.3}$$

where $E_{inc} = 2E_1 + E_0$ is the incident beam energy at the target. To obtain longitudinally polarized electrons at the target, one chooses the incident electron energy such that $\theta = n\pi$, where n is an integer. For $E_0 = 20$ MeV and $n = 2$, the *magic energy* that yields longitudinally polarization at the target is 574 MeV.

2.3 Møller Polarimeter

The Møller polarimeter was used to measure the spin polarization of the electron beam. [27] The spin polarization of the electrons in the beam is measured by elastical scattering with polarized atomic electrons. The spin dependence of this scattering is well known, so the

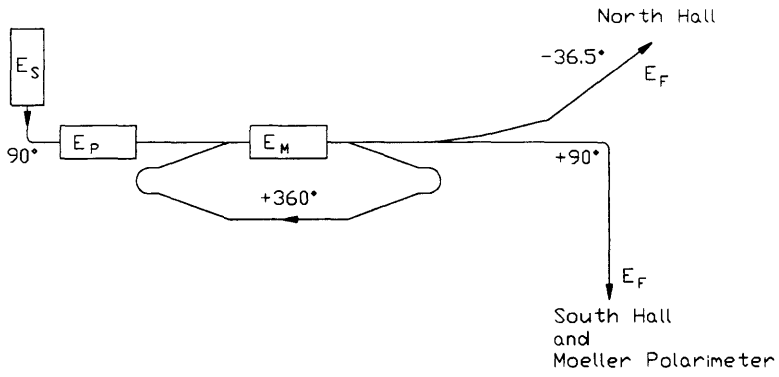

Figure 2-6: A simple schematic of beam transport line from injector to end station.

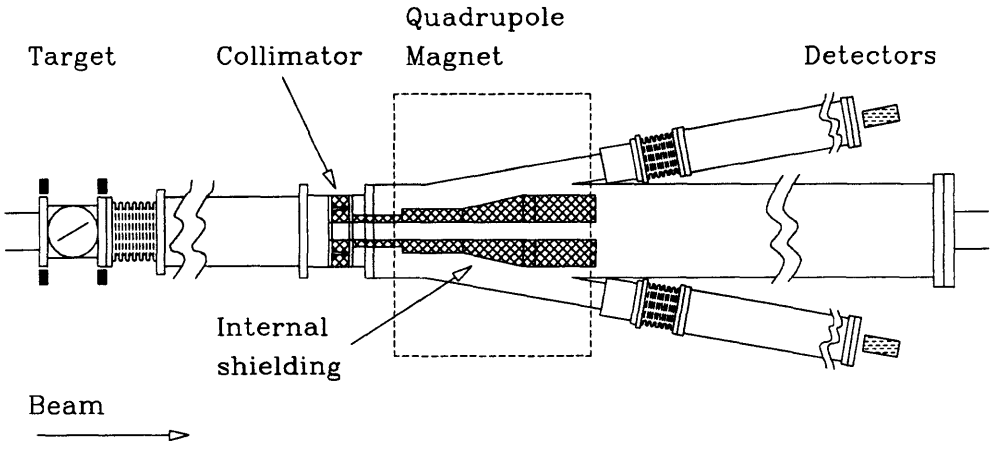

Figure 2-7: Top view of Møller polarimeter on the B-line in the South Hall.

measurement of the scattering cross section can reveal the spin polarization of the electron beam. The cross section of the elastic electron-electron scattering is

$$\frac{d\sigma}{d\Omega} = \frac{d\sigma_o}{d\Omega}\left(1 + \sum_{i,j} P_B^i A_{ij} P_T^j\right) , \tag{2.4}$$

where where P_B^i and P_T^j are the components of the beam and target polarization as measured in the rest frame of the electron. The cross section consists of the spin independent term $\frac{d\sigma_o}{d\Omega}$ and nine asymmetries A_{ij} which determine the polarization dependence of the cross section. In the extreme relativistic limit, the asymmetries, A_{ij}, are to lowest order in QED:

$$A_{zz} = -\frac{(7+\cos^2\theta_{cm})\sin^2\theta_{cm}}{(3+\cos^2\theta_{cm})^2} \tag{2.5}$$

$$A_{xx} = -A_{yy} = -\frac{\sin^4\theta_{cm}}{(3+\cos^2\theta_{cm})^2} \tag{2.6}$$

$$A_{zx} = A_{xz} = -\frac{2\sin^3\theta_{cm}}{\gamma(3+\cos^2\theta_{cm})^2} \tag{2.7}$$

$$A_{xy} = A_{yx} = A_{yz} = A_{zy} = 0 , \tag{2.8}$$

where θ_{cm} is the scattering angle in the center of mass frame and γ is the Lorentz factor relating the laboratory and center of mass frames. The coordinate system is defined such that the z-axis is along the momentum of incident electron beam and the x-axis lies in the scattering plane. At $\theta_{cm} = 90°$ where A_{zz} is the largest and is relatively flat, $A_{zz} = -7/9$, $A_{xx} = -1/9$, and $A_{yy} = 1/9$ with the cross terms, A_{zx} and A_{xz}, going to zero. By choosing the kinematics to maximize A_{zz} with respect to θ_{cm}, uncertainties due to variations in the scattering angle and finite acceptance can be reduced and minimized.

In the general case at $\theta_{cm} = 90°$, the physics asymmetry is

$$A_{phy} = -\frac{7}{9}P_B^z P_T^z + \frac{1}{9}P_B^x P_T^x - \frac{7}{9}P_B^y P_T^y . \tag{2.9}$$

Under the assumption that both the beam and the target are polarized only along the beam momentum and that there is no background, the asymmetry simplifies to

$$A_{phy} = -\frac{7}{9} P_B^z P_T^z \ . \tag{2.10}$$

The electron beam polarization is experimentally determined by measuring the asymmetry for both positive and negative helicities of longitudinally polarized electron. The measured asymmetry is given by

$$A_{meas} = \frac{N_+ - N_-}{N_+ + N_-} \ , \tag{2.11}$$

where N_+ and N_- are the yields for the positive and negative helicities, respectively, normalized with total beam charge. In addition to the Møller scattering, there exist other processes such as Mott scattering off the nuclei. For an electron energy of 574 MeV, the Mott cross section is much larger than the Møller cross section. The Møller polarimeter is constructed to accept only electrons of the correct energy for Møller scattering, but there exists spin independent background. The measured asymmetry diluted by the background is related to the true asymmetry by

$$A_{meas} = A_{phy} \left(\frac{1}{1 + B/S} \right) \ , \tag{2.12}$$

where B is the background yield and S is the Møller signal yield.

The Møller Polarimeter is located on the B-line upstream from the main target area. The main elements of the Møller Polarimeter as shown in Figure 2-7 are:

1. A magnetized foil target.
2. A collimator to define the scattering angles.
3. A magnet and aperture to select the momentum range to be accepted.
4. Čerenkov detectors for measuring the scattered electrons.

The target is made of Supermendur, an alloy of 49% Fe, 49% Co and 2% Va by mass. The target electrons are polarized with a 150 Gauss magnetic field using Helmholtz coils.

The target is magnetized to near saturation. The spins of the outer electrons of the alloy align with the magnetic field. The target polarization was found to be $8.02 \pm 0.12\%$ in an earlier measurement at MIT-Bates.

The scattering angle in the lab frame is 2.42°. Then they are bent outward by a 25cm diameter quadrupole magnet which has its defocussing plane in the same plane as detectors. Thus the scattered electrons are bent to reach the Čerenkov detectors. The quadrupole magnet strength can be varied to ensure that the electrons that pass through the collimator reach the detector.

Each Čerenkov detector is used separately to measure the asymmetry. The signals from each Čerenkov detector are integrated over the time of a beam pulse. In order to remove any signal offset, so called pedestal beam pulses with no current, are used. The offset signals measured with pedestal beam pulses are subtracted from the signals of the detector measured with *normal* beam pulses. This helps to eliminate the offset and drift in the electronic signals. Then, the asymmetry is determined according to Equation 2.11.

The Møller polarimeter can also be operated in coincidence mode. In this case, electrons from the Møller scattering are identified by detecting scattered electrons in coincidence by both Čerenkov detectors. This method helps to eliminate the background from other processes, but a beam peak current is required to be low enough to avoid a large percentage of accidentals. Coincidence mode was not used in this experiment.

2.4 M.I.T.-Basel Loop Target

The M.I.T.-Basel Loop Target, pictured in Figure 2-8 was used in this experiment. This target system consists of two loops for cryogenic liquid as well as BeO (34.51 mg/cm^2), carbon (91.46 mg/cm^2) and a blank target.

Two loops for cryogenic liquid hold hydrogen and deuterium cells of 5 cm and 3 cm, respectively. Most of each loop is made of stainless steel. The material of the cell wall was cold-rolled Havar, the compositions of which are 42.0% Cobalt, 19.5% Chromium, 19.1% Iron, 12.7% Nickel, 2.7% Tungsten, 2.2% Molybdenum, 1.6% Manganese, and 0.2% Carbon. The loops are operated at around 18°and slightly above 1 atmosphere. They have a capacity of 1.5 liters. Each loop consisted of a heat exchanger, an internal heater,

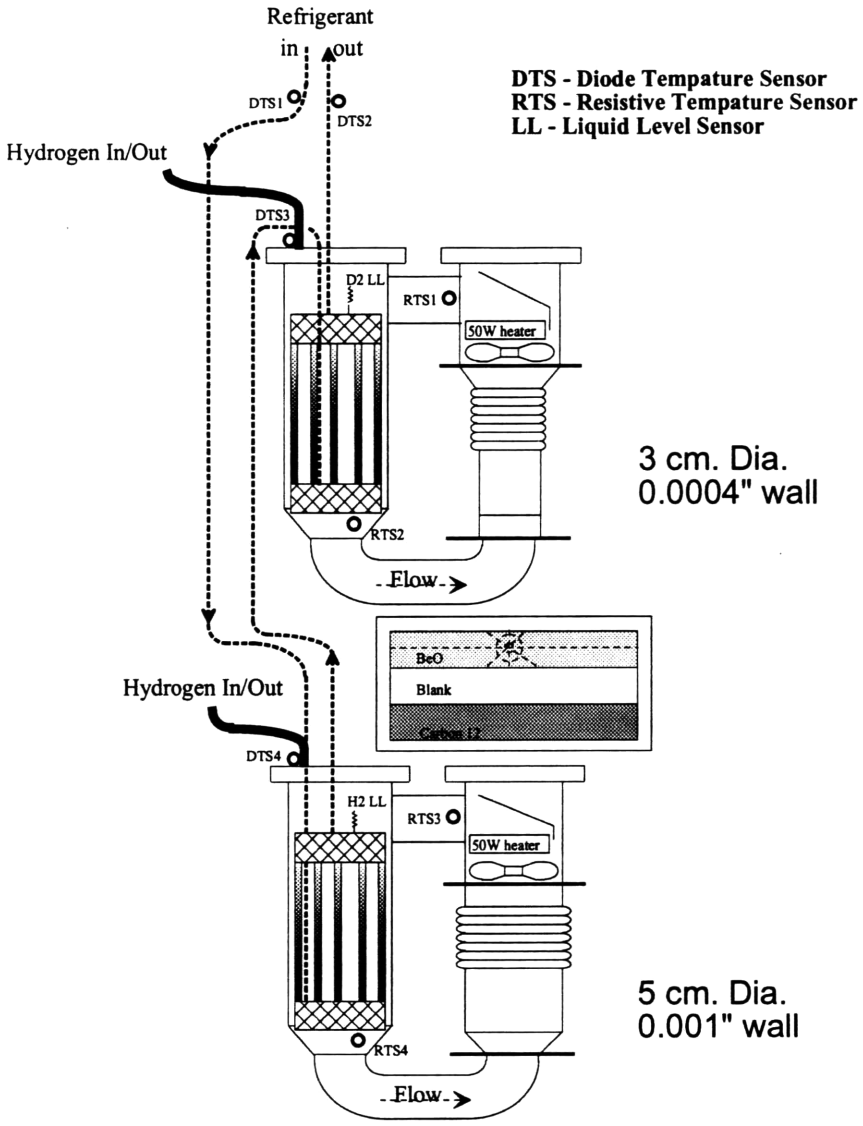

Figure 2-8: Schematic of the M.I.T.-Basel Loop Target.

	Bottom	Top
Liquid	LH_2	LD_2
Cell Diameter (cm)	5	3
Cell Wall Thickness (μm)	25.40	10.16
Cell Wall Density (g/cm^2)	0.042	0.017
Nominal Pressure (atms)	1.0	1.0
Nominal Temperature (K)	20.3	23.7
Nominal Liquid Density (g/cm^2)	0.36	0.48

Table 2.1: M.I.T.-Basel Loop Target parameters for this experiment.

two temperature sensors, and an internal fan. The two loops are cooled by gaseous He from 200 W refrigerator. The temperature of the liquid is monitored with diodes and carbon glass resistors and the pressure is monitored by pressure transducers located at the gas fill line. The internal 50 W variable heater is used to maintain a constant liquid temperature when the beam is switched on and off. An internal fan is used to cycle the liquid continually in the loop to reduce the local boiling effects and improve the cooling efficiency of the heat exchanger.

The heater is controlled, and the target temperature and pressure are monitored by an IBM PC compatible computer in the counting bay. The target temperature and pressure are recorded at 30 second intervals during filling and venting of the target, and at 30 second intervals during the data taking. Further target characteristics are summarized in Table 2.1. More details on the target system can found in Reference [28].

2.5 The Electron Spectrometer-MEPS

The Medium Energy Pion Spectrometer (MEPS) was used to detect the scattered electrons. MEPS is a QQD (quadrupole-quadrupole-dipole) spectrometer, schematically illustrated in Figure 2-9. The MEPS uses point-to-point focusing ($\langle x|\theta\rangle = 0$) in the vertical bend plane (momentum dispersion direction) and parallel-to-parallel focusing ($\langle y|y\rangle = 0$) in the transverse plane. A two-inch thick lead collimator is used to define the solid angle at the front of MEPS. The dimensions of its opening are ± 80 mr in the

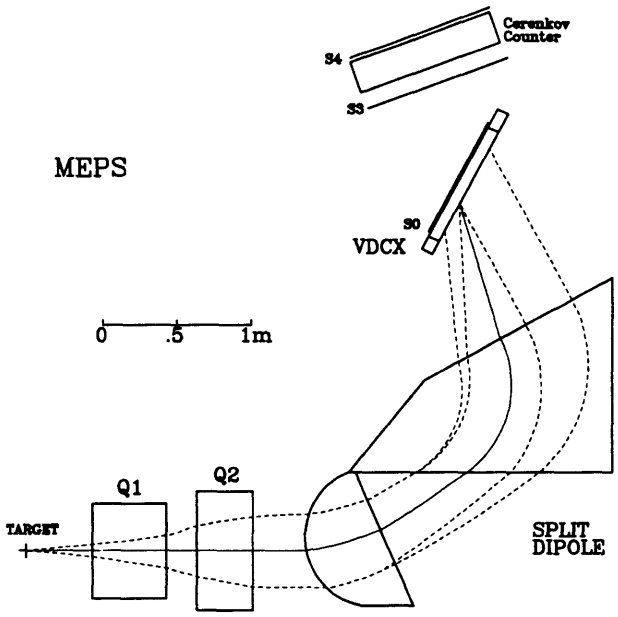

Figure 2-9: Magnet configuration with the focal plane instrumentation for the MEPS.

scattering angle and ±55 mr in the out-of-plane angle. The solid angle acceptance is 14.0 msr. Some of its design properties are listed in Table 2.2

The MEPS focal plane detector system is instrumented with three scintillators, an aerogel Čerenkov detector and a crossed vertical drift chamber (VDCX). The scintillators provid the trigger and the timing fiducial. The Čerenkov detector is discriminated between electrons and heavier particles such as pions. The VDCX measures the coordinates of the particle at the focal plane. Further information can be found in the MEPS design report, Reference [29].

2.5.1 MEPS Scintillators and Trigger Electronics

Three scintillators, MS0, MS1 and MS4, are used in the MEPS focal plane for this experiment. They are made of NE-110 plastic scintillator material. The scintillator dimensions are listed in the Table 2.3. MS0 is directly on top of the VDCX. MS3 and MS4 are just below and above the Čerenkov detector. Two photo-multiplier tubes (PMT)

Maximum Momentum	414 MeV/c
Momentum Resolution	$1.0 \cdot 10^{-3}$
Momentum Acceptance	22%
Angular Range	$35 - 140°$
Geometric Angular Acceptance	
Radial Plane (θ)	140 mr
Transverse Plane (ϕ)	240 mr
Radius of Curvature	0.75 m
Flight Path	4.7 m
Bend Angle	110°

Table 2.2: MEPS design properties.

Scintillator	Width	Length	Thickness
MS0	17.8 cm	58.4 cm	6.4 mm
MS3	20.3 cm	91.0 cm	3.2 mm
MS4	20.3 cm	91.0 cm	3.2 mm

Table 2.3: Dimensions of MEPS scintillators.

are connected to each scintillators through Lucite light guides. The PMTs on MS3 and MS4 are at the opposite ends of the scintillators but for MS0 they are mounted next each other on the side.

The logic signal MEPS pilot[2] is generated by the coincidence of three logic signals from each scintillator as shown in Figure 2-10. The signals from the PMTs for MS0 are OR'ed because each PMT covers only half of the scintillator. The signals from the PMTs for MS3 and MS4 are meantimed because the timing of the meantimed signal is nearly independent of the event position along the scintillator. The meantimed signal (MS3MT) from MS3 is delayed and the meatimed signal (MS4MT) from MS4 is widened, so that the timing of the 3-fold coincidence MEPS Pilot (MPI) be defined. The MPI is sent via 90 ohm, 100 ns cable to the OHIPS, the proton spectrometer, for use in the coincidence logic. The six analog signals from the PMTs are amplified and sent upstairs to analog-to-digital converters(ADC). The discriminated signals from the PMTs and the

[2] *Pilot* is used as *trigger* at Saclay. *Pilot* is the French word for *trigger*.

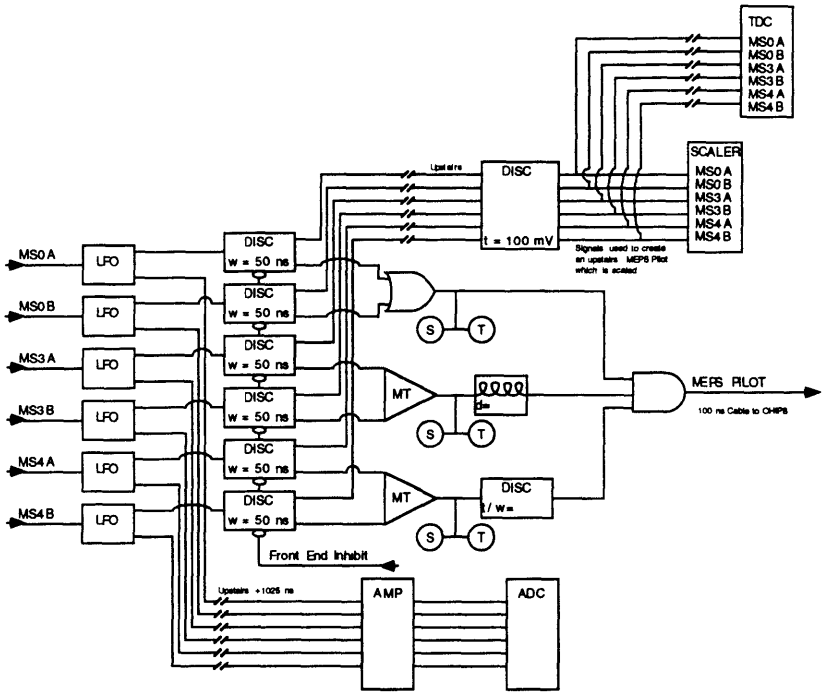

Figure 2-10: The MEPS scintillator electronics.

logic signals from the MEPS electronics are also sent upstairs where they are scaled and sent to time-to-digital converters (TDC).

2.5.2 The aerogel Čerenkov detector

An aerogel Čerenkov detector was used to differentiate electrons from pions. The aerogel has an index of refraction of 1.05 so that electrons and any other particles moving faster than 95 % the speed of light would produce Čerenkov radiation and slower particles do not. Pions would not radiate with momentum less than 430 MeV/c. The PMTs, five in a row on each side, detect the light in the diffusion cavity above the aerogel. The signals from each PMT are amplified and sent upstairs. If at least one PMT fired, a signal is sent to CAMAC to enable it to read the TDCs and ADCs.

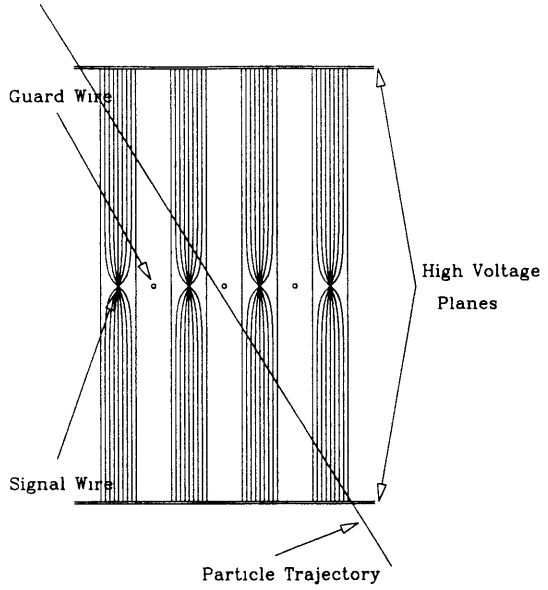

Figure 2-11: Electric field lines of a VDC. The field lines for the guard wires were left out to reduce confusion. The ratio of the vertical scale to horizontal scale was altered to emphasize the non-linear region of the field lines.

2.5.3 The MEPS VDCX

The MEPS VDCX consists of two independent planes. The wires in one plane are orthogonal to the wires in the other plane. The wires in both planes are 45°relative to the dispersive and transverse directions. The active area of each plane is 7 × 25 inches. The wire planes consist of alternatively spaced signal and guard wires. There are 128 signal wires in each plane. The signal wires are 20 μm in diameter and their spacing is 4.23 mm. The guard wires made of beryllium-copper are 50 μm in diameter. The guard wires are used to maintain a uniform field shape in the drift cells. The spacing between the two wire planes of the VDCX is 3.8 cm. The length of the drift cells is around 2.5 cm. Both sides of each plane are connected to aluminized mylar at high voltage of approximately 9.0 kV. The VDCX is operated with a gas mixture of 50% argon and 50% isobutane. When a charge particle passes through the chamber, it ionizes the gas. The ionization electrons then moves toward the signal wires along the electric field formed by the high voltage planes and the signal wires. The electric field is shown in Figure 2-11. The nominal drift velocity is 0.05 mm/ns and the maximum drift time is therefore about 250 ns.

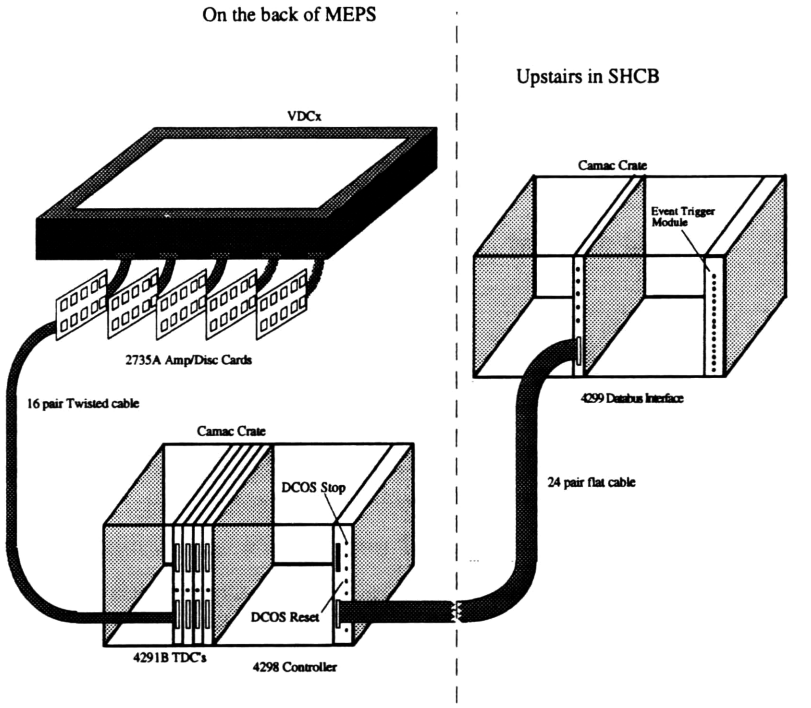

Figure 2-12: DCOS System for the MEPS VDCX.

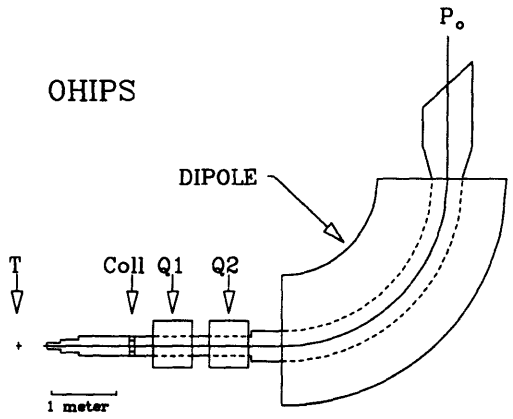

Figure 2-13: Magnet configuration of OHIPS.

The MEPS VDCX information is obtained with a LeCroy 4290 Drift Chamber Operating System (DCOS) as shown in Figure 2-12, which replaced the previously used TIRUS system. The DCOS system consists of 16 channel LeCroy 2735 amplifier/discriminator cards, 32 channel 4291B TDCs, a 4298 system controller, and a 4299 databus interface. The DCOS system provides one TDC per wire, whose timing resolution is 0.5 ns per channel. The TDCs are operated in common stop mode and drift times for all the wires fired during an event are read and therefore multiple particle trajectories could be handled. Further details of the DCOS system can be found in Reference [30].

2.6 The Proton Spectrometer-OHIPS

The One-Hundred Inch Proton Spectrometer (OHIPS) was used to detect the recoil protons. The OHIPS is a vertically bending QQD (quadrupole-quadrupole-dipole) spectrometer, schematically illustrated in Figure 2-13. It is designed to be point-to-point focusing in both the bend and the transverse planes, ($\langle x|\theta\rangle = 0$) and ($\langle y|\phi\rangle = 0$). The drift distance is 1.6 m and the quadrupoles are set in *reverse model* where first quadrupole in OHIPS has a vertical focus and second a horizontal focus. This mode provides for larger vertical acceptance, but smaller horizontal acceptance than the normal mode

where first quadrupole in OHIPS has a horizontal focus and second a vertical focus. A 5.1 cm thick lead collimator is used to define the solid angle at the front of OHIPS. The dimensions of its opening are ± 55 mr in the scattering angle and ± 80 mr in the out-of-plane angle. The solid angle acceptance is 7.0 msr. The OHIPS is also used to detect electrons, in order to calibrate and normalize the spectrometer. Some of its design properties are listed in Table 2.4. Further information on OHIPS can be found in Reference [31].

To install the FPP on top of the OHIPS, many modifications were made before this experiment. It was necessary to remove the Čerenkov detector and add reinforcements to improve the structural integrity of the spectrometer. The concrete shielding hut was rebuilt to increase safety and stability of OHIPS and was made larger to accommodate the FPP. It was necessary to add cross struts to the shielding hut platform to reduce the oscillations. An airconditioner and a dehumidifier were installed inside the shielding hut to provide a better operation environment for the FPP. A larger electronics platform was also installed to handle the additional electronics required by the FPP. The new support structure for the VDCX was built to accommodate the FPP and also allowed for better alignement between the VDCX and the dipole magnet.

Maximum Momentum	1300 MeV/c
Momentum Resolution	$1.4 \cdot 10^{-3}$
Momentum Acceptance	10%
Angular Range	$19 - 140°$
Geometric Angular Acceptance	
Radial Plane (θ)	245 mr
Transverse Plane (ϕ)	57 mr
Radius of Curvature	2.54 m
Flight Path	9.7 m
Bend Angle	90°

Table 2.4: OHIPS design properties.

The OHIPS focal plane detector system is instrumented with two scintillators, a crossed drift chamber (VDCX) and a recoil proton polarimeter as shown in Figure 2-14. The scintillators provides the trigger and the timing fiducial. The VDCX and the first two chambers measures the coordinates of the particle at the focal plane.

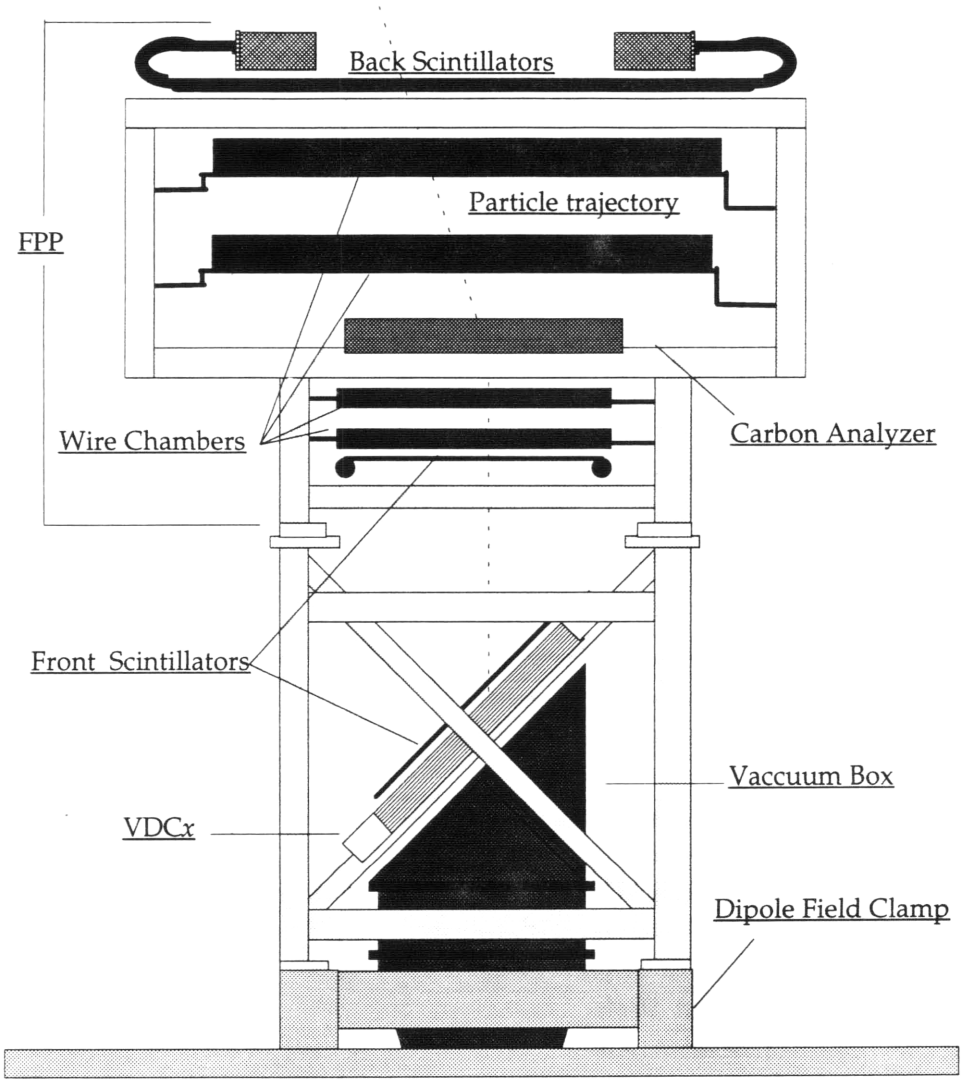

Figure 2-14: The OHIPS focal plane instrumentation.

2.6.1 OHIPS Scintillators and Pilot

Scintillator	Width	Length	Thickness
OS0	20.3 cm	65.0 cm	5.0 mm
FS1	37.0 cm	71.0 cm	6.0 mm
FS2(AB,CD,EF)	145.0 cm	32.0 cm	13.0 mm

Table 2.5: Dimensions of OHIPS scintillators.

Three scintillators, OS0, FS1 and FS2(AB,CD,EF) are used in the OHIPS focal plane for this experiment. The first scintillator, OS0, is directly above the VDCX and the second scintillator, FS1, is right below the first chamber of the FPP. The last scintillator which consists of three scintillators, FS2AB, FS2CD and FS2EF, are located directly on top of the fourth chamber of the FPP and placed side by side. The dimensions of the scintillators are summarized in Table 2.5. Each scintillators has two PMTs attached to its opposite ends via Lucite light guides.

The logic signal OHIPS pilot is generated by the coincidence of three logic signals from each scintillator as shown in Figure 2-15. For each scintillator, the signals from the PMTs on either end are discriminated and meantimed. The three FS2 meantimed signals are OR'ed because three FS2 scintillators are overlapped slightly. This OR'ed signal is AND'ed with the OS0 meantimed signal and the FS1 meantimed signal to generate the OHIPS Pilot. The individual PMT signals are sent to TDCs, ADCs and scalers to save their timing, pulse hight information and to count signals.

2.6.2 The OHIPS VDCX

The OHIPS VDCX is very similar to the MEPS VDCX. There are 128 wires in each plane, but only 110 of 128 wires are read out. The readout system is different compared with that of the MEPS. The OHIPS uses a delay line system to read out the wire position and drift time information to calculate the particle's trajectory. Each wire is connected through an amplifier/discriminator to a delay line. There are four delay lines per each plane with every fourth wire connected to same delay line.

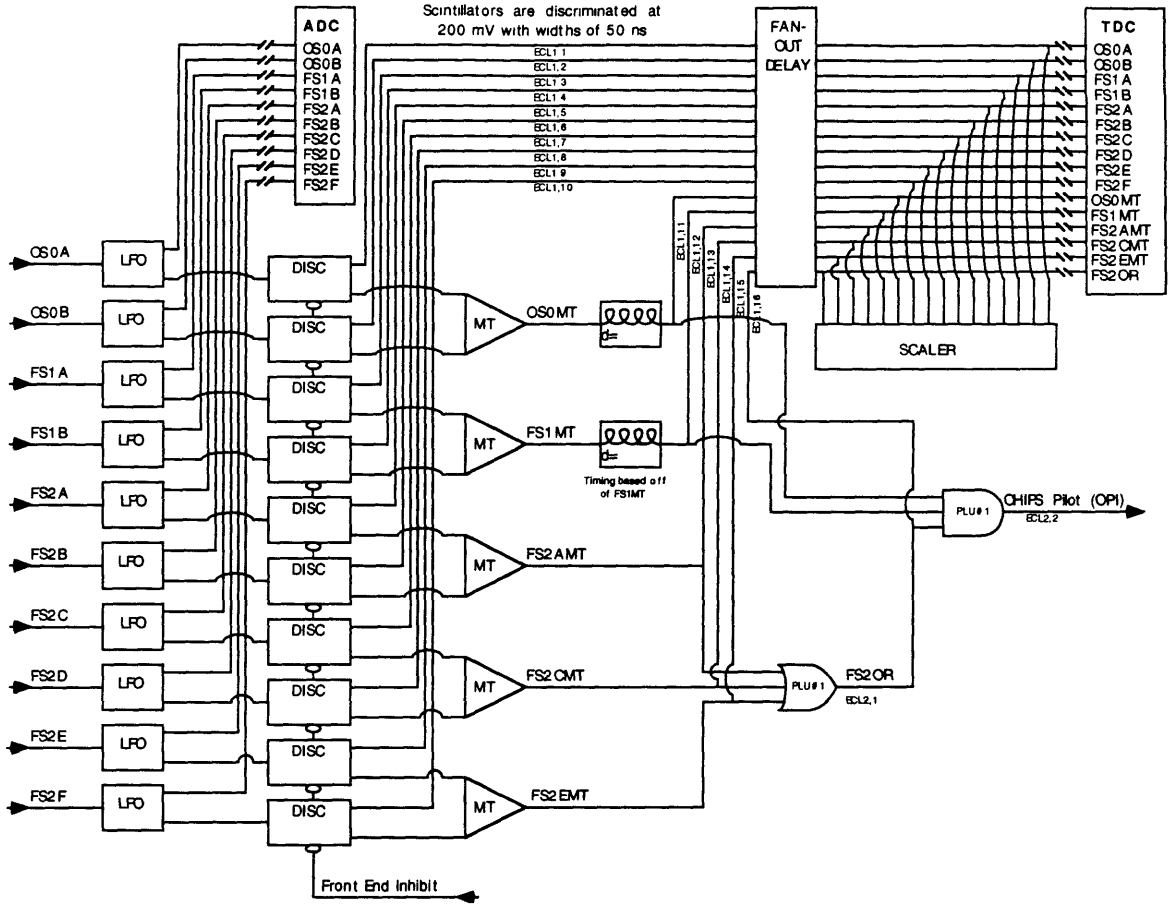

Figure 2-15: OHIPS scintillator electronics.

The TDCs are operated in common start mode and signals from the eight delay line ends formed stops. The times from the left and right ends of a delay line, t_l and t_r, determines the wire number, n, and drift time, t_d, as follows,

$$t_r = (n-1)\tau + t_d + T_0, \tag{2.13}$$

$$t_l = (N-n)\tau + t_d + T_0, \tag{2.14}$$

where T_0 is a constant delay time due to propagation of the signal to the input of the TDC, τ is the delay time between two successive wires on the delay line ($\approx$ 2.2 ns) and N is the total number of wires in the delay line. Solving Equations 2.13 and 2.14 for t_d

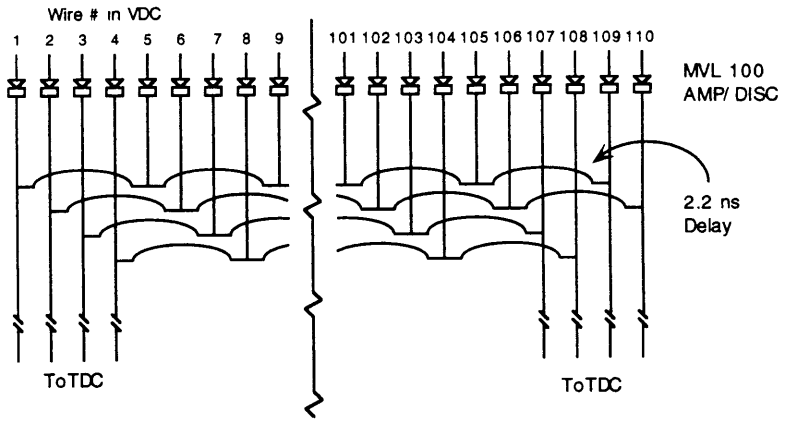

Figure 2-16: Schematic of the OHIPS delay line system.

and n giving

$$t_d = \frac{1}{2}(t_r + t_l - (N-1)\tau - T_0), \tag{2.15}$$

$$n = \frac{1}{2\tau}(t_r - t_l + (N-1)\tau). \tag{2.16}$$

With the wire numbers and drift times the particle's trajectory can be determined in the software, which will be discussed in Chapter 3.

2.7 The OHIPS Focal Plane Polarimeter

The OHIPS Focal Plane Polarimeter was used to measure the recoil proton polarization. Details of the FPP are shown in Figure 2-14. It consists of a carbon analyzer, four multi wire proportional chambers (MWPC), two scintillator planes, the readout electronics and the control electronics. The carbon analyzer is used for a secondary scattering analyzing medium. Its thickness can be varied between 0.5 cm and 30.5 cm. Two scintillator planes are used to provide the timing and trigger the readout cycle.

2.7.1 The FPP Multi Wire Proportional Chambers (MWPC)

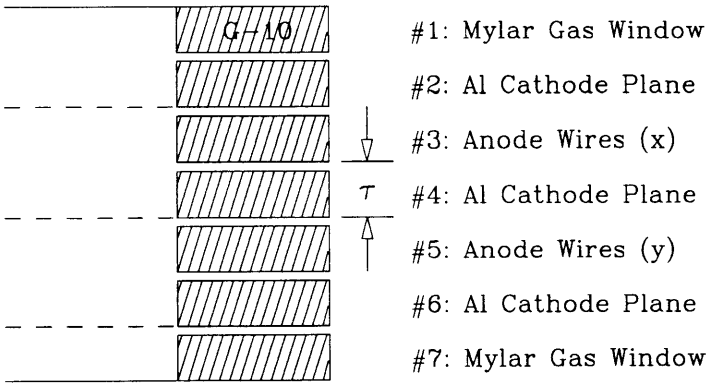

Figure 2-17: Side cross sectional view of the FPP MWPC.

	Front	Rear
Active Length	71.1 cm	142.2 cm
Active Width	37.3	88.1 cm
Wire Spacing	2.1 cm	4.2 cm
Operating Voltage	4.7 kV	4.8 kV
Wires in X	336	336
Wires in Y	176	208

Table 2.6: Properties of the FPP chambers.

The FPP has two small MWPCs before the carbon analyzer and two large MWPCs after the carbon analyzer. The frame of the chamber is made of G-10 fiberglass, the thickness of which is 1.27 cm for large chambers and 0.64 cm for small chambers. There are 7 planes in each chamber. The first and seventh planes are gas windows of 1 mm mylar. The second and sixth planes are cathode planes of 0.25 mm single sided mylar and fourth plane is a cathode plane of 0.25 mm double sided mylar. The third and sixth planes are the anode X and anode Y planes where 20μm gold-plated tungsten wires are soldered and epoxed to circuit board.

The front small chambers are designed to have a full acceptance for the OHIPS VDCX. The back large chambers are designed to accept the protons at the secondary scattering angles up to 25°. The chambers are operated with a gas mixture of 50% argon and 50% istobutane. The dimensions and operating characteristics are summarized in Table 2.6.

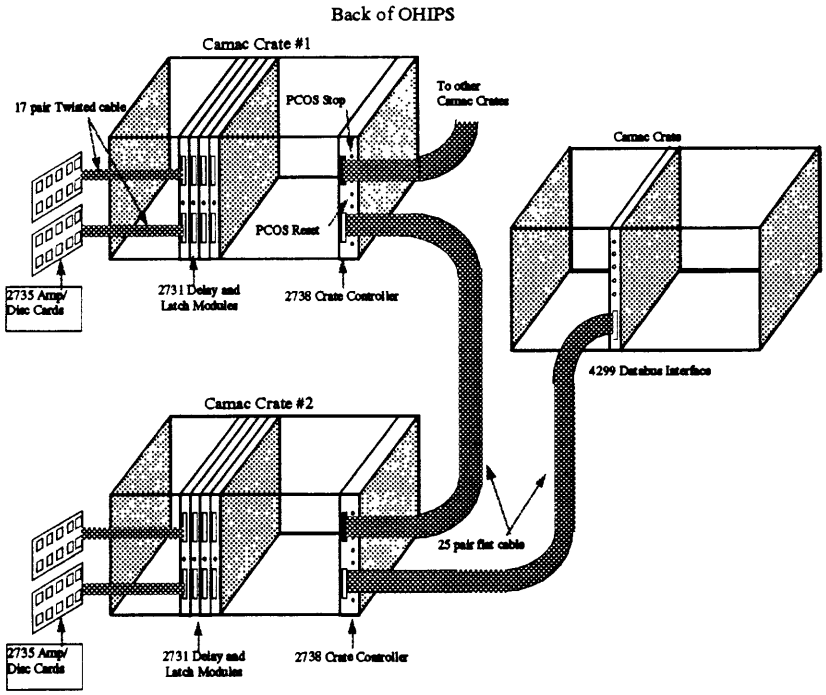

Figure 2-18: PCOS III system.

2.7.2 The FPP MWPC Readout System

The LeCroy Proportional Chamber Operating System (PCOS) III is used for the read out system for the FPP MWPCs. As shown in Figure 2-18, this system consists of 16 channel LeCroy 2735 amplifier/discriminator cards, 32 channel 2731 delay and latch modules, a PCOS III 2738 system controller, and a 4299 databus interface. Each wire of the MWPCs is connected to an amplifier/discriminator (A/D) card via insulated twisted-pair ECL cable. The sixteen channel output from a pair of cards are connected to the ECL inputs of 32 channel 2371 delay and latch modules in a CAMAC crate. These delay and latch modules in each crate are controlled by PCOS III 2738 system controller that allows for rapid readout and converts the discriminated signals in each latch channel into a preprogrammed address information about the wire number and the plane number. A

total of six CAMAC crates are required to instrument eight chamber planes. The latches for planes X_1, Y_1, X_2 and Y_2 have their own crate, but the latches for planes X_3/Y_3 and X_4/Y_4 are contained in a single crate. The output of six crate controllers is connected to a 4299 databus interface. The interface has a memory buffer to store the latched addresses until they can be transferred to the memory of the data aquisition computer during the readout cycle.

2.7.3 Small Angle Rejection System

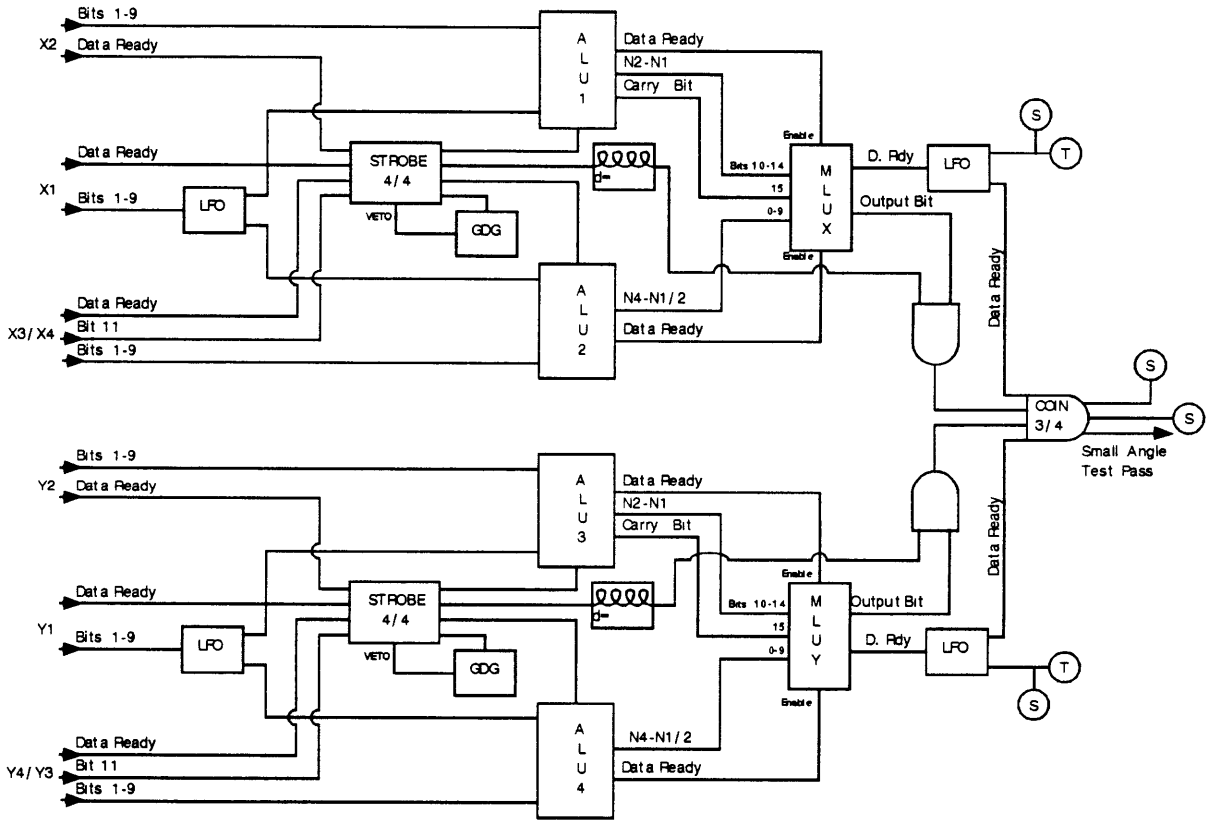

Figure 2-19: Schematic of the Small Angle Rejection System.

The Small Angle Rejection System (SARS) is designed to eliminate the events from multiple Coulomb scattering where the analyzing power is too small to produce a measurable asymmetry. The electronic diagram of the SARS is shown in Figure 2-19. The

SARS utilizes two LeCroy ECLine modules: the 2378 Arithmetic Logic Unit (ALU) and the 2372 programmable Memory Lookup Unit (MLU). The wire number information from each PCOS system crate controller goes to two 2378 Arithmetic Logic Units which can evaluate sums and differences of two data words. One unit calculates the difference, N2 − N1.[3] Another unit calculates the difference, N4 − N1/2.[4] These ALUs are strobed by the four-fold coincidence of the three data ready signals from each of the three PCOS crates and the plane bit from 3/4 plane crate which means that the hit is in plane 4.

The wire differences determined by the ALUs are then presented as addresses to the LeCroy 2372 Memory Lookup Unit (MLU). The MLU is preprogrammed so that a memory address is loaded with '1' if the address corresponds to an good scattering angle greater than the predetermined minimum angle. Otherwise, the memory address is loaded with '0' and corresponds to the event to be rejected. The predetermined angle is 3.5° for this experiment. The Small Angle Test Pass as shown in Figure 2-19 is formed by the three out of four coincidence of the Data Ready signals and the pulsed output signals of the MLUs for both X and Y planes. The Small Angle Test Pass indicates whether the final trajectory is inside or outside of a rectangular cone around the initial trajectory. The SARS generate this binary output in 140 ns once the wire number information becomes available. More details about the SARS can be found in a paper by R. Lourie et al. [33].

2.7.4 Multiple Hit Rejection System

Multiple Hit Rejection System is implemented to be able to reject events with three or more hit wires in any plane. This system is necessary because the SARS is built on the assumption that only one wire per plane is hit. Events with two hit wires are accepted because events with two adjacent hit wires can be easily reconstructed and events with two non-adjacent hit wires can be discarded in software.

The electronic diagram of the Multi-Hit Rejection System is shown in Figure 2-20. This system utilizes a LeCroy 4532 ECL Majority Logic Unit (MALU). The sixteen inputs for the MALU are three copies of the Data Ready signals from X1, X2, Y1 and Y2, and one copy of the Data Ready singal and plane bits from X3/4 and Y3/4. The

[3]N1 and N2 are hit wire numbers for plane 1 and plane 2. Likewise, N3 and N4 for plane 3 and plane 4.

[4]The factor of 2 is due to the fact that the wire density of plane 1 is twice that of plane 4.

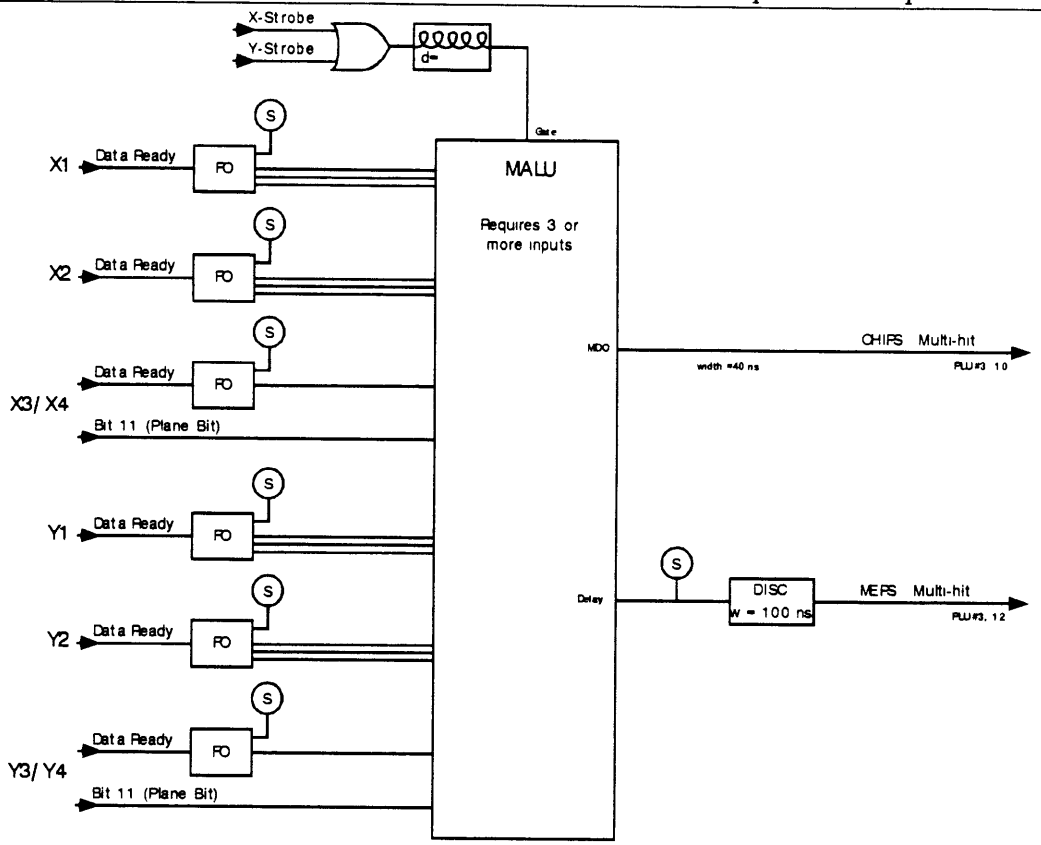

Figure 2-20: Schematic of the Multi-Hit Rejection System.

MALU is gated on a delayed version of the strobe generated in the SARS. This delay is set so that the MALU would not examine its input until after the first two hits occurred. The use of the plane bits from 3/4 planes makes it possible not to test the multi-hit events from the plane 3.

2.8 Coincidence Trigger Electronics

The coincidence trigger electronics can be divided into two sections, label 1 and label 2 electronics, as shown in Figure 2-21. Level 2 electronics includes the coincidence signals between two spectrometers and prescalers used for diagnostic purposes. In either case, data from one (or both) of the spectrometers are latched pending the decision to

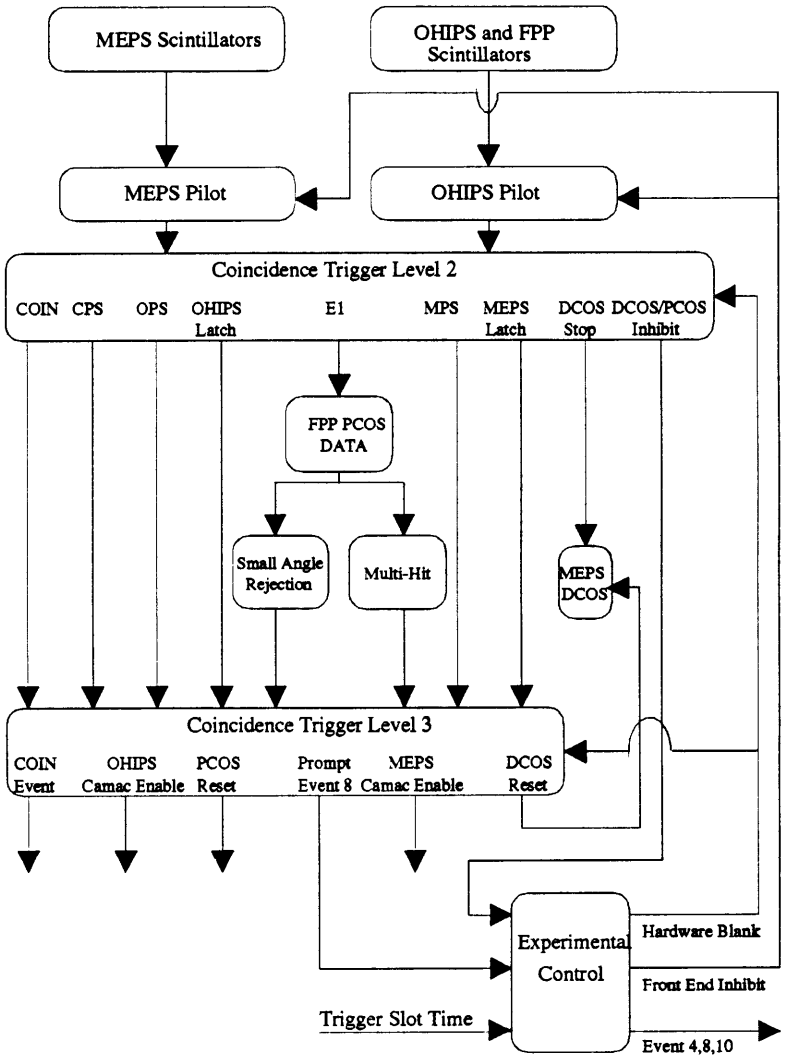

Figure 2-21: Overview of the coincidence trigger electronics.

read the data from the level 3. Level 3 electronics makes a decision to either record the event information or reset the electronics. A more detailed description can be found in Reference [32]

2.8.1 Level 2 Electronics

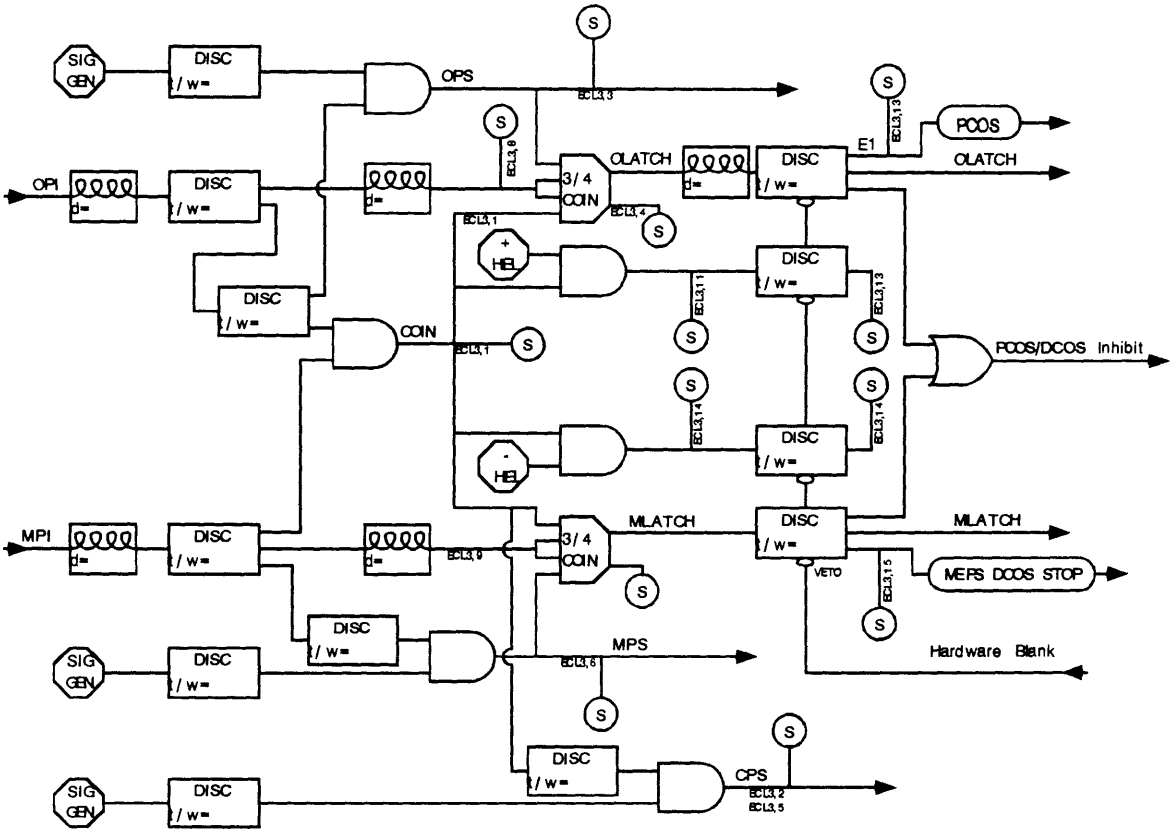

Figure 2-22: Level 2 electronics schematic.

Level 2 electronics starts with the OHIPS Pilot (OPI) and MEPS Pilot (MPI). These two pilot signals for two spectrometers are AND'ed to generate the coincidence pilot (CPI). The OPI is rediscriminated to a width of 10 ns and the MPI is rediscriminated to a width of 80 ns. The OPI is delayed so that it determines the coincidence timing and the large width of the MPI provide a large timing window. For coincidence events, each positive and negative helicity signal from the control room is AND'ed with the CPI

to be scaled in order to count the number of events for each beam helicity. The Level 2 electronics are shown in Figure 2-22.

The prescale events OPS, MPS and CPS are made by taking a logical AND of pulses from signal generators with the OPI, MPI or CPI. These events are useful to study non-coincident proton and electron events, such as diagnostic purposes as well as determining the single arm cross sections and focal plane efficiencies. The rate of prescale events can be varied by controlling the signal generators which are in the counting bay.

The OHIPS and MEPS latches, OLATCH and MLATCH, are generated by a coincidence pilot (CPI) or prescale events (OPS and MPS). The OLATCH is used as a start for the OHIPS delay line readout TDCs and generates E1 signal for latching the FPP wire signals in PCOS. A copy of the MLATCH is sent back to the MEPS to stop the DCOS.

2.8.2 Level 3 Electronics

Level 3 electronics is the last stage of trigger electronics. A schematic diagram of Level 3 electronics is shown in Figure 2-23. It performs the decision to either record the event or reset the electronics to receive the next event. It uses the delayed version of level 2 inputs as well as results from the FPP hardware test (Small angle Rejection System and Multi Hit Rejection System). The OHIPS CAMAC Enable (OCE) and the MEPS CAMAC Enable (MCE) are generated to cause the event information to be read out and recorded when the decision is made to accept the event. There are two types of events to be accepted. The first type is a coincidence event defined as a logical AND of coincidence pilot and the hardware test. The second type is the prescale event, either a MEPS prescale event, a OHIPS prescale event or a coincidence prescale event.

The PCOS and DCOS resets are generated when the event is not one of these two types of events. The resets clear the information about the stored event in the electronics so that the electronics are available to receive the next event.

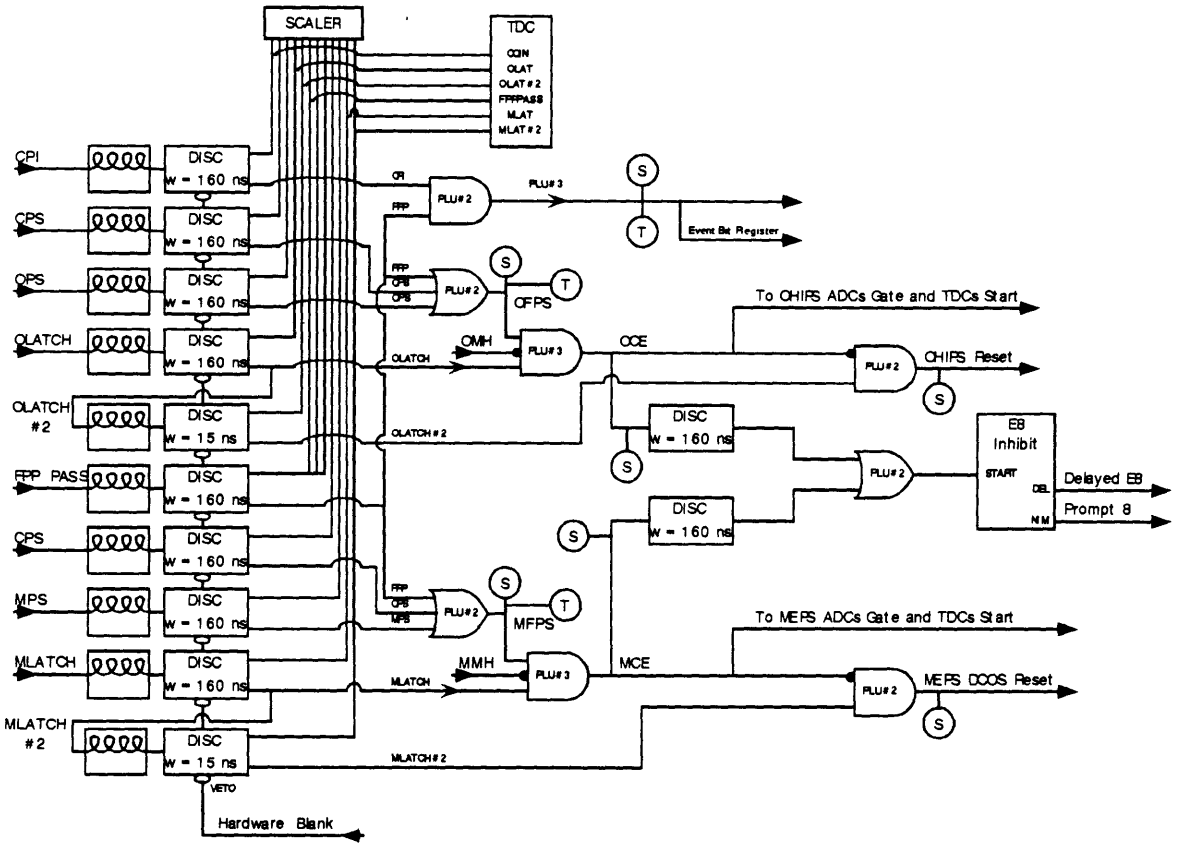

Figure 2-23: Level 3 electronics schematic.

2.8.3 Experimental Control Electronics

The experimental control electronics perform the decision on whether an event is read out or not, or how the data acquisition system is triggered when an event is read out. It generates five signals: Event 4, Event 8, Event 10, the Hardware Blank (HB) and Front End Inhibit (FEI). The event signals, Event 4, Event 8, and Event 10, trigger the data acquisition system to read the CAMAC electronic modules and record the information. The Hardware Blank (HB) and Front End Inhibit (FEI) are used to inhibit new data at different stages of trigger electronics so as not to corrupt the old data. The Experimental Controls circuit is shown in Figure 2-24.

The Event 4 signal is generated every 12 seconds by the GUN signal with gate-delay generators (GDGs) to cause the scaler information to be recorded. The Event 8 signal is generated by the first good physics event in each beam burst. Due to the long read out

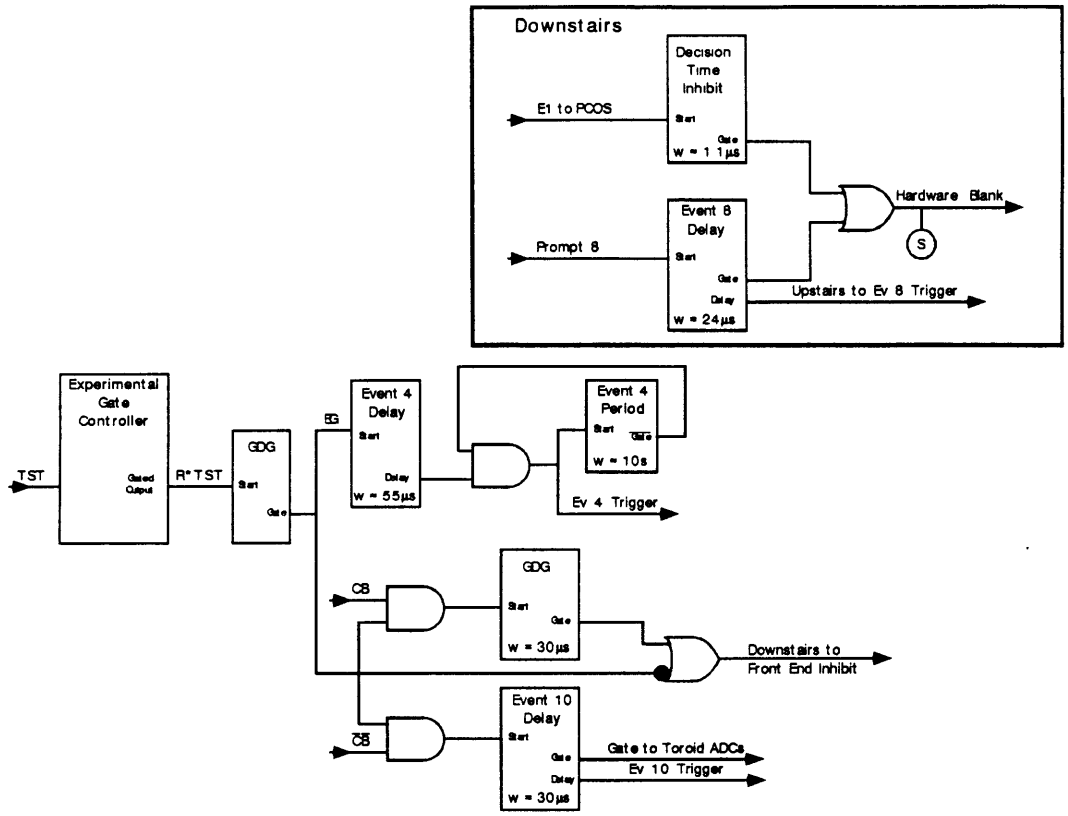

Figure 2-24: Experimental Control Electronics schematic.

times the electronics need to be inhibited at the earliest state. The readout time of the Event 8 is about 4 ms and thus for the two beam bursts subsequent to the event burst, the data acquisition is turned off until the computer is ready to accept the data. The Event 10 is triggered to cause the beam position monitors, and toroid ADCs, as well as the helicity bit to be recorded for the live beam bursts.

There are two types of inhibit in trigger electronics: Front End Inhibit (FEI) and the Hardware Blank (HB). The Hardware Blank (HB) inhibits a later stage of the electronics. As described earlier, it takes 1 μs to make a decision for the small angle rejection system. During the decision time, the HB prevents the stored data from being contaminated, but it is necessary to allow scintillators to continue to count events and beam charge to be measured because the numbers of pilot scalers need to be counted and the charge of the beam burst need to be measured, for a whole beam burst, not just the portion of the beam burst for which the electronics are not inhibited. Front End Inhibit (FEI), on the other hand, inhibit all stages of trigger electronics to prevent new data from corrupting

Event Type	Description
Event 3	Clear and reset CAMAC modules
Event 4	Read out scalers
Event 6	Read beam profile monitor
Event 8	Read out the physics data
Event 10	Read out the beam current monitor
Event 13	Read out target parameters

Table 2.7: The descriptions of Event Types.

the event. This typically inhibits the next two bursts entirely while an event is being recorded.

2.9 Data Acquisition System

The data acquisition system starts with the CAMAC crate, which contains modules such as the ADCs, TDCs and scalers. The CAMAC crate also contains LAMPF trigger module and a crate controller. A crate controller which is in the right-most slot of CAMAC crate, is connected to a Microprogrammable Branch Driver (MBD) via Branch Highway Cable. The MBD is connected to a micro-Vax III computer system on which the data acquisition software runs. The data acquisition software used in this experiment, is called Q Data Acquisition System (Q-System). [34] The Q-System was developed at LAMPF (Los Alamos Meson Physics Facility) to run on top of the VMS operating system.

The LAMPF trigger module is used to identify an event type. It contains 31 levels of event triggers with decreasing priority. Events 4 through 11 can be triggered externally with a logic pulse. The different types of events are described in Table 2.7.

The Microprogrammable Branch Driver (MBD) transfers the data from CAMAC to the computer's memory. The MBD buffers the data from the crate and passes them on to a micro-Vax III computer when the buffers are full. The MBD has a few buffers and instructed by a primitive programming language called QAL-code. [34] The QAL-code defines various CAMAC modules and contains all the instructions for each event types

which are identified by the LAMPF CAMAC trigger module. The readout order defines the structure of raw data array.

The Q-system was the data acquisition software package. [34] It controls the interactions between the MBD and the tape driver. It also provides an interactive histogramming and test package, and executes user-supplied subroutines known as the analyzer. The analyzer allows for extracting the information from raw data. A brief layout of the analyzer including all of the major components is shown in Figure 2-25.

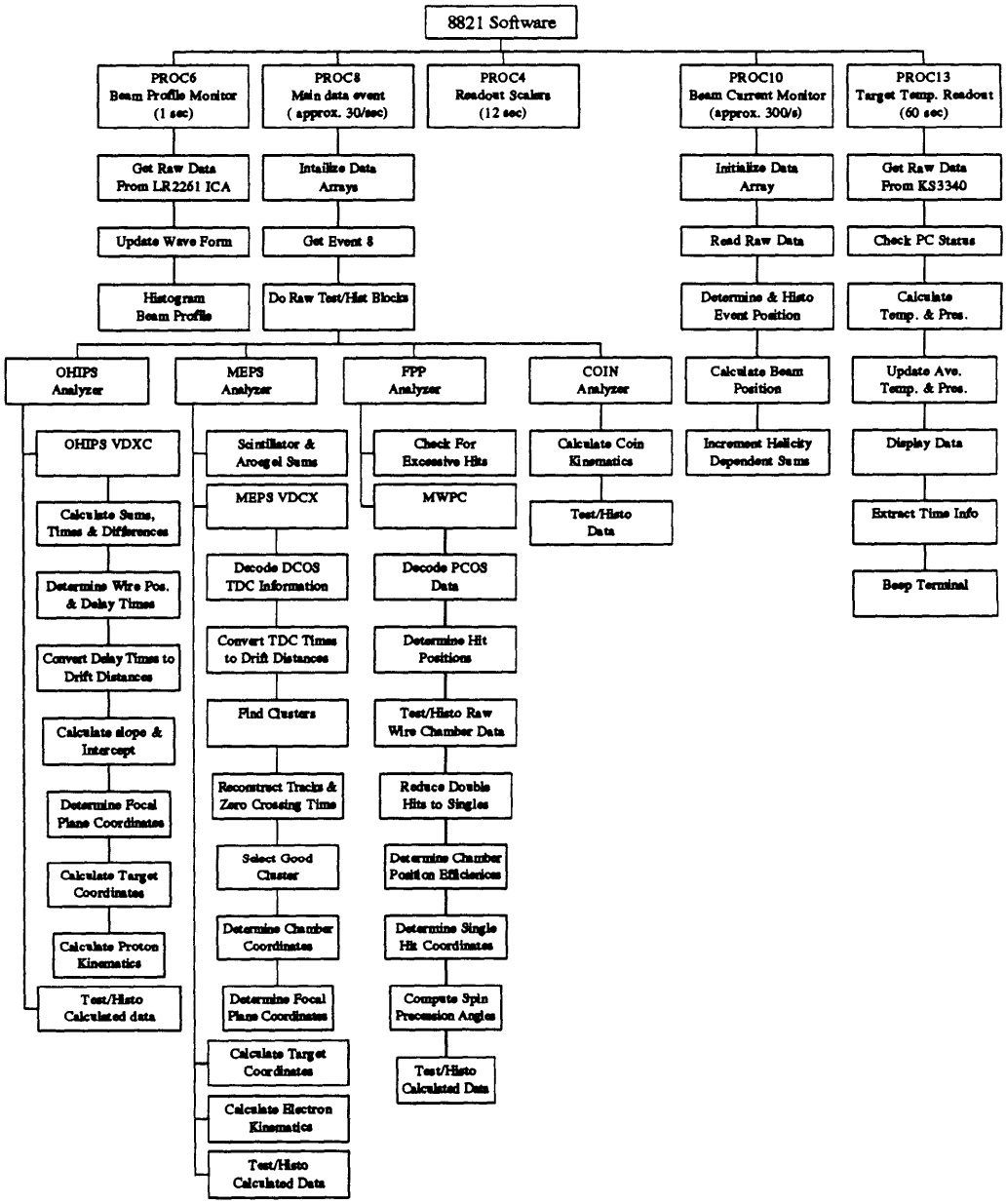

Figure 2-25: Analyzer Software Flowchart.

Chapter 3

Data Analysis

This chapter will describe the data analysis including the methods used for:

1. Extraction of information from the VDCXs of OHIPS and MEPS. Based on VDCX information, trajectories of proton and electron as well as kinematic variables are determined.
2. Analysis of FPP. Using information of FPP, proton polarizations at the focal plane are measured.
3. Spin precession in the spectrometer. Using the spin precession through the spectrometer, proton polarizations at the target are extracted from those at the focal plane.
4. Software Cuts and Background Subtraction.
5. Determination of beam polarization.

3.1 VDCX Analysis

This section presents the decoding of the VDCX wire chamber information. The measured drift times obtained from the VDCX wire chamber determine the particle trajectory at the spectrometer's focal plane. This information coupled with a knowledge of the

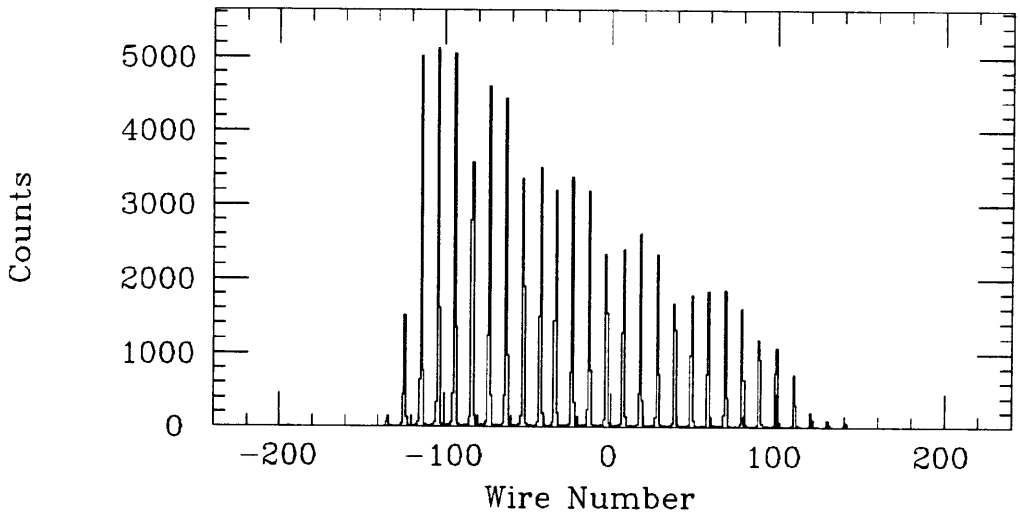

Figure 3-1: Wire Number in an OHIPS VDCX chamber.

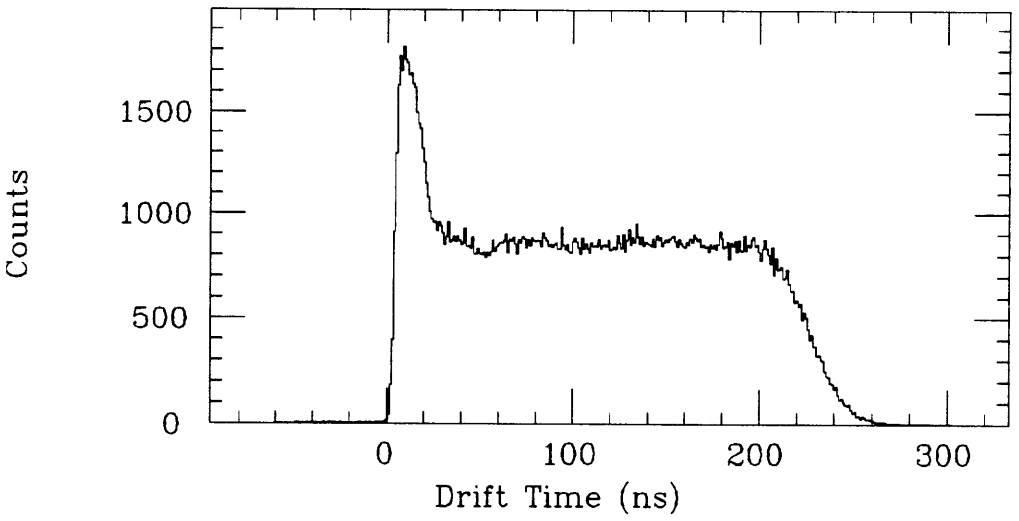

Figure 3-2: Drift Time in an OHIPS VDCX chamber.

spectrometer's optical properties permits calculation of the corresponding quantities at the target. This section gives a brief description of the method of the determining the position and angle of the particle track from the drift time information as well as the method of tracing back through the spectrometer in order to determine these quantities at the target.

The wire chamber readout systems employed by MEPS and OHIPS are quite different. The OHIPS VDCX is read out with a four delay line per wire plane system. For each event, the sixteen raw delay line times (four delay lines per chamber, two ends per delay line) are converted to wire numbers and drift times using the algorithms described in section 2.5.2. Figure 3-1 shows the wire number and the drift distance. The wire number is proportional to the TDC difference $(t_l - t_r)$ and the drift time is proportional to TDC sum $(t_l + t_r)$ from the left and right delay times. Though the MEPS VDCX chamber is quite similar to OHIPS's, the readout system is very different. Rather than a delay-line system, MEPS uses the DCOS system in which drift times for all the fired wires are read. Since one is not limited to four wires as in OHIPS, multiple particle trajectories can be read. This makes the analysis more complicated but also less corruptible.

3.1.1 Calibration of Drift time to Drift Distance

The drift distances are obtained from the drift times for each wire. The method for converting the drift times to drift distances for the different regions is based on the work of David Jordan [36] and Bates-ELSSY spectrometer users who spent much time investigating this problem.

When an energetic charged particle passes through the VDCX wire chamber, it ionizes gas molecules along its path. In the strong electric field, the ionized electrons immediately reach the terminal velocity where the isobutane damping matches the electric force. The electrons travel at this terminal velocity along the electric field lines to the wire. The drift time is the time it takes the electron to travel from the point of ionization to the wire. It has been shown that the actual drift velocity of the electrons is roughly constant at 50 μm/ns for a wide variety of voltages and gas mixtures used. [37] For this reason, the drift time is roughly proportional to the distance traveled by the electron.

For particle trajectory reconstruction purposes, the drift distance is defined as the perpendicular distance from the sense wire to the particle trajectory, as shown in Figure 3-3. The drift distance is different from the path length traveled to the wire by the ionized

electrons. It is assumed that the leading edge of the pulse is defined by the ionized electrons which followed the shortest path length along the field lines from the particle trajectory to the wire.

Figure 3-2 shows a typical drift time histogram. The drift time histogram is a plot of dN/dt, the number of events per time. The shape of the spectrum results from the geometric effects. The long flat region is formed by events passing through the parallel field area of the cell. The initial sharp peak at the beginning of the histogram, labelled I, is mostly an effective increase in drift velocity due to the change in the geometry of the field lines near the wire. [37] The real drift velocity has not changed; it is roughly constant at 50 μm/ns throughout the cell of a VDCX wire. The drift path changed. Far away from the wire, the electric field lines are very nearly parallel. Near the wire, the electric field lines turn inward toward the wire. The peak in the drift time curve is the result of the field lines changing from parallel to radial. The drop-off region is due to limitations of the delay line readout system and the chamber acceptance. The four delay line system in OHIPS makes the drop off of the drift time curve gradual. The drift velocity in this drop-off region is still constant at roughly 50 μm/ns.

To accomplish the calibration of drift time to drift distance, the local drift velocity is used to account for the apparent peak in drift velocity that results from the arrangement of the field lines to the wire. 50 μm/ns is used as the drift velocity for the flat region and the drop-off region. For the leading edge of the drift time histogram, the effective local drift velocity for i^{th} channel is:

$$v_i = 50\mu\text{m/ns}\frac{N_i}{\langle N^{flat}\rangle}, \tag{3.1}$$

where N_i is the number of counts in the i^{th} channel and $\langle N^{flat}\rangle$ is the average counts in the flat region. Then this local drift velocity is used to increment the drift distance. The drift distance for the i^{th} channel is

$$d_i = d_{i-1} + v_i\Delta t, \tag{3.2}$$

where Δt is the drift time per channel.

These drift distance values for particular drift time histogram channels are then made into lookup tables, a separate table for each VDCX wire chamber plane. Once the lookup

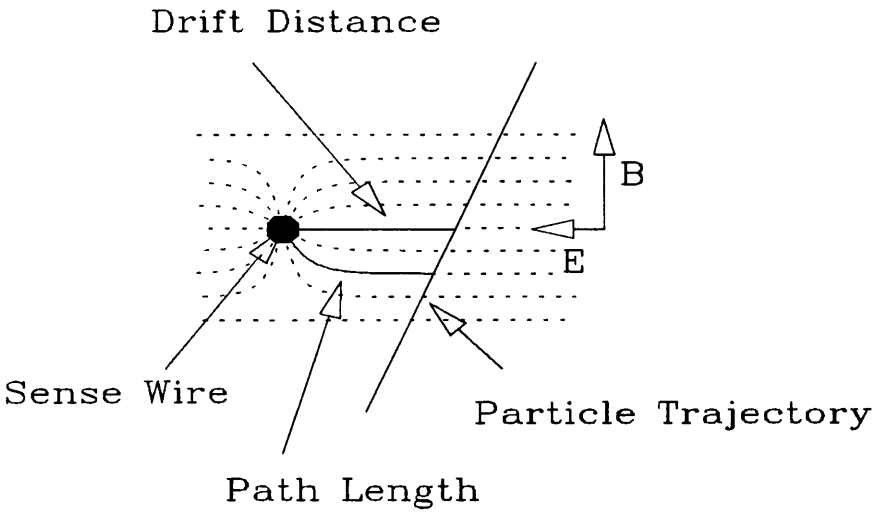

Figure 3-3: Drift paths of ionized electrons in a VDCX chamber. The dashed lines are the electric field lines.

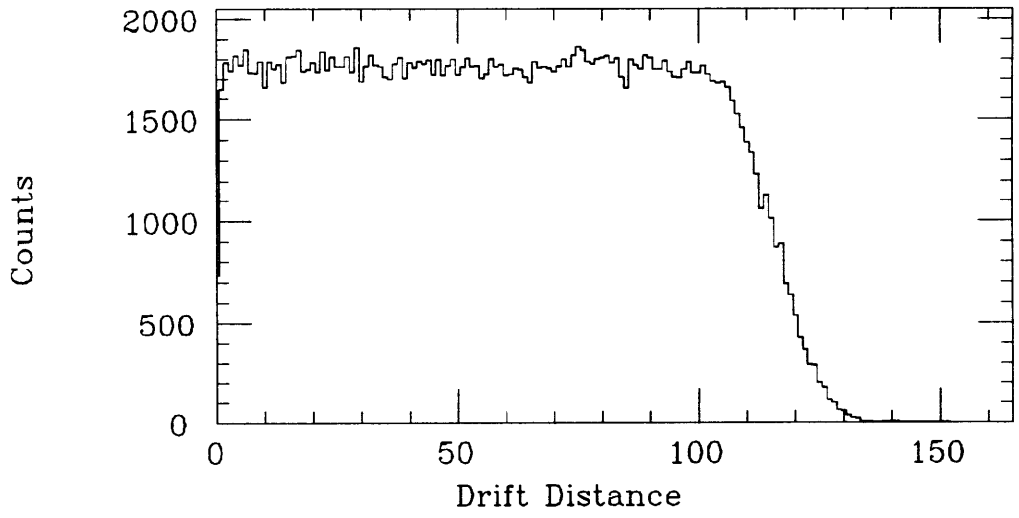

Figure 3-4: Drift Distance in an OHIPS VDCX chamber.

table has been made, any similar drift time can be converted to drift distances. Figure 3-4 shows the drift distance histogram obtained using this method.

3.1.2 Determination of Wire Plane Coordinates

After the drift distances are determined, the next step is to reconstruct the particle trajectory from the VDCX data, see Figure 3-5. The angle (α) and wire-plane intercept (u) of the particle trajectory are determined using a least squares fit.

The wire chamber information gives no indication of which side of a given wire the particle passed. However, probable rules can be established. A four-hit trajectory is most likely to be that in figure 3-5, with two on either side. It also would satisfy the relation,

$$d_3 < d_4 \qquad d_2 < d_1 \ . \tag{3.3}$$

If there are only three wires fired, the situation is likely to be as in figure 3-5 one wire left out. The two wires on either end will be on the opposite side. If the three wires are adjacent, then the middle wire is on the same side as the end wire with the longer drift distance. Otherwise it is on the same side as the adjacent end wire.

We fit u and α using the obvious geometric relations, a sample of which are given here. The angle is calculated differently for the three types of events and the equations for each are listed below:

$$\tan\alpha = \frac{2w}{d_1 - d_2 + d_4 - d_3}, \quad \text{for four wires and no gap;} \tag{3.4}$$

$$\tan\alpha = \frac{w}{d_> - d_2}, \quad \text{for three wires and no gaps;} \tag{3.5}$$

$$\tan\alpha = \frac{w}{d_n - d_2}, \quad \text{for three wires and a one wire gap;} \tag{3.6}$$

where w is the wire spacing in the chamber (= 4.23 mm) and the $d_i's$ are the individual distances, $d_>$ is the greater drift distances between d_1 and d_3, and d_n is the nearest wire position to d_2.

The wire plane intercept(u) is then calculated using the angle and the position with the following equation,

$$u = \frac{u_1 + u_3 + m(d_1 - d_3)}{2}, \tag{3.7}$$

$$m = \frac{1}{\tan\alpha}, \tag{3.8}$$

where u_1 and u_3 are the positions of the first and third wire in the VDCX and m is the slope of a particle trajectory.

Since the drift distances which are above the wire plane are indistinguishable from those which are below the wire plane, it is necessary to fit all possible combinations of the drift distances. The solution which yields the smallest χ^2 and a positive slope are used. Particle trajectories with four consecutive hits or three hits with no more than one wire gap are used in the fit. Those with $\chi^2 \leq 0.2$ are accepted. Due to the large error possible in very small drift distances [38], those wire-hits with drift distances less than 1 mm are not used.

For a good event, the slope of the trajectory should be within an acceptable range which is physically possible. A cut in software is made on the slopes for each chamber to eliminate events the slope of which is less than 30° and greater than 42°. Figure 3-6 shows the histogram for a typical run for the top and bottom chambers.

3.1.3 Calculation of Focal Plane Coordinates

Slope (m) and intercept (a) in each wire plane of the chamber are determined by the least squares fit described in the previous section. This information can then be used to determine focal plane coordinates (X_{fp}, Y_{fp}, θ_{fp}, ϕ_{fp}). Figure 3-7 shows the focal plane and wire plane coordinate systems used for both OHIPS and MEPS. The angle and intercept of the particle trajectory with the top (bottom) wire plane are denoted by α_T (α_B) and a_T (a_B) respectively. The first step is to project the intercepts from each wire plane to the plane between the chambers, using the relations

$$u'_T = -u_T - m_T\frac{D_c}{2}, \tag{3.9}$$

$$u'_B = u_B + m_B\frac{D_c}{2}, \tag{3.10}$$

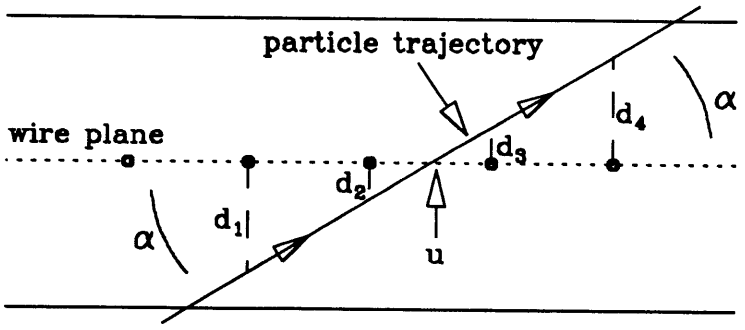

Figure 3-5: The particle trajectory calculated from the VDCX data. The drift distance for the i^{th} wire is d_i. The quantities to be determined are α and u, the angle and the intercept.

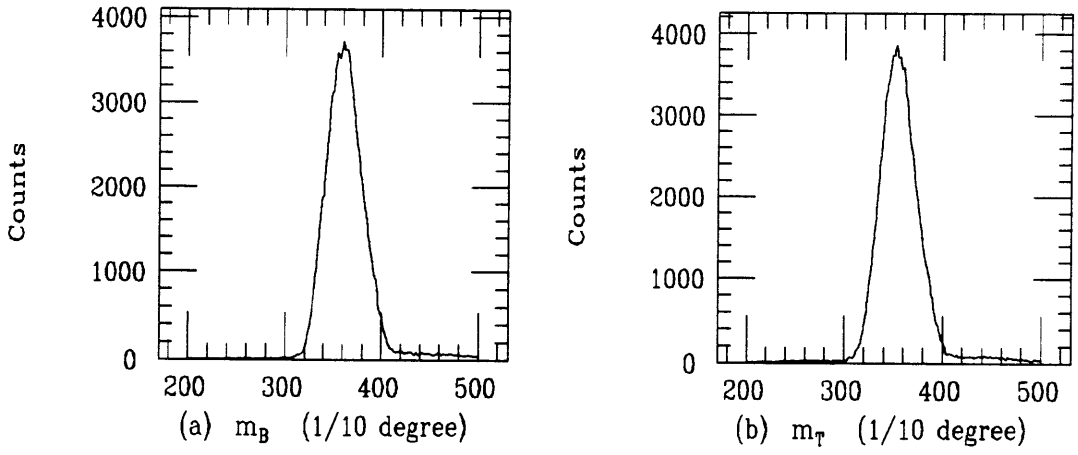

Figure 3-6: SLOPS for OHIPS VDCX chambers

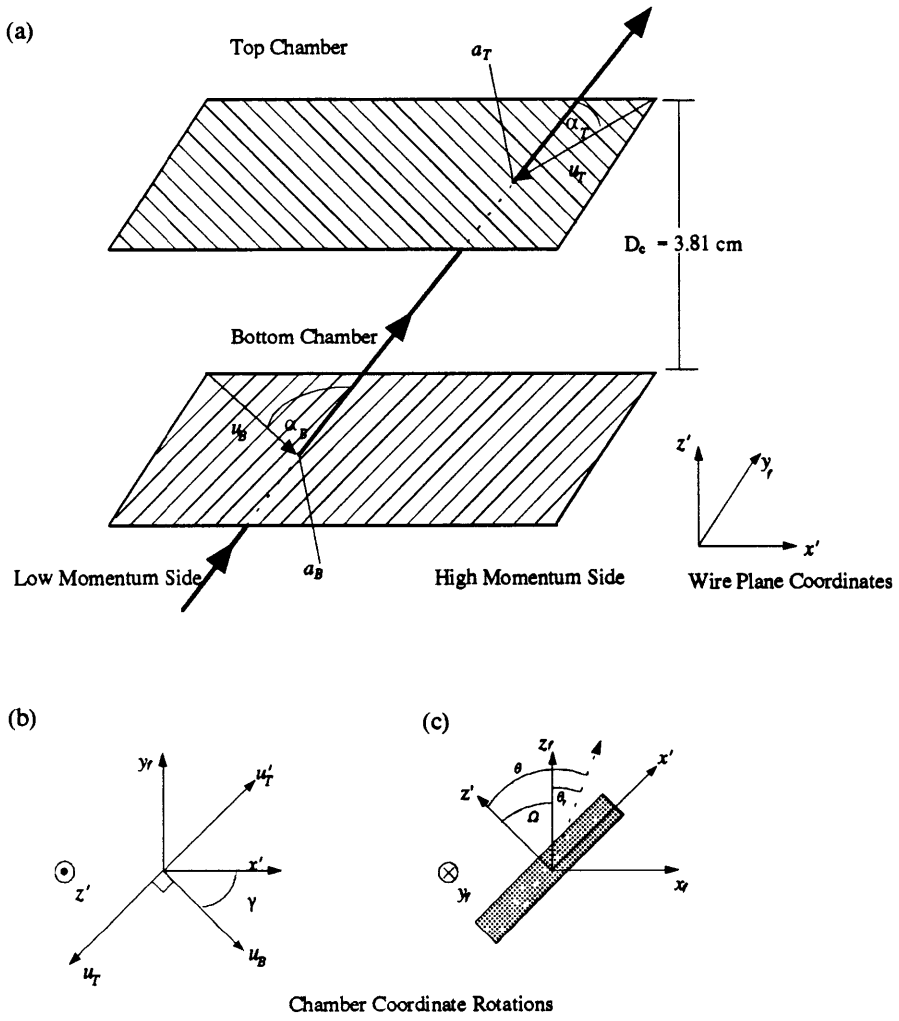

Figure 3-7: The VDCX coordinate system. (a) shows the orientation of the two planes with respect to each other. (b) and (c) show the rotations about z' and y_f, respectively.

where u_i and m_i are the intercept and slope in a VDCX plane, u_i' is a wire plane intercept and D_c is the separation between the top and bottom chambers. The next step is to rotate the projected coordinates to a system with X' towards the direction of increasing momentum, but in the plane of the wire chamber

$$\begin{pmatrix} X' \\ Y_{fp} \end{pmatrix} = \begin{pmatrix} \cos\gamma & \sin\gamma \\ -\sin\gamma & \cos\gamma \end{pmatrix} \begin{pmatrix} u_B' \\ u_T' \end{pmatrix} \qquad \gamma = 45°, \tag{3.11}$$

as shown in figure 3-7b. γ is the angle the wires makes with the momentum direction and is equal to 45°. A rotation about Y_{fp} to account for the VDCX's tilt with respect to the central momentum ray is then needed:

$$\begin{pmatrix} X_{fp} \\ Y_{fp} \\ Z_{fp} \end{pmatrix} = \begin{pmatrix} \cos\Omega & 0 & -\sin\Omega \\ 0 & 1 & 0 \\ \sin\Omega & 0 & \cos\Omega \end{pmatrix} \begin{pmatrix} X' \\ Y' \\ 0 \end{pmatrix}, \tag{3.12}$$

as shown in figure 3-7c. Ω is the focal plane tilt relative to the xz plane. For the OHIPS, it is equal to 45.3° and for the MEPS, it is 45.7°.

Two focal plane angles θ_{fp} and ϕ_{fp} are determined by the VDCX:

$$\theta_{fp} = \arctan\left(m_B\cos\gamma + m_T\sin\gamma\right) - \Omega, \tag{3.13}$$

$$\phi_{fp} = \arctan\left(\frac{-m_B\sin\gamma + m_T\cos\gamma}{(m_B\cos\gamma + m_T\sin\gamma)\sin\Omega + \cos\Omega}\right). \tag{3.14}$$

With the addition of the focal plane polarimeter on the OHIPS, it is more accurate to calculate these two angles, θ_{fp}, ϕ_{fp} using a linear fit using the VDCX position coordinates and those of the two FPP chambers in front of the carbon block. In this way, the resolution of the focal plane angles increases from a FWHM of 17 mrad for measurement from the VDCX alone, to 6 mrad for the measurement from the three chambers.

3.1.4 Momentum Calibration of Focal Plane

Since the VDCX in OHIPS lies approximately along the focal plane, there is a direct relationship between the location of the particle X_{fp} and the momentum of the particle relative to the central ray. The relative momentum of the particle, δ, is defined as:

$$\delta = \frac{(P - P_c)}{P_c} \ , \tag{3.15}$$

where P is the momentum of the particle and P_c is the central momentum of the spectrometer. To do the momentum calibration, the location of the first excited state of ^{12}C(e,e') is scanned across the focal plane by changing the magnetic field in 2.0 % steps.

The location of the first excited state at the focal plane for different values δ is measured and fitted to a second order polynomial of δ to determine the dispersion parameters. The peak locations are determined by ALLFIT [39]. The Figure 3-8 shows a histogram of X_{fp} in OHIPS for a typical ^{12}C(e,e') measurement and Figure 3-9 shows the X_{fp} and δ data along with the fit. The fitted parameters are listed in the Table 3.1.

3.1.5 Determination of Target Coordinates

Target coordinates are determined using focal plane coordinates and spectrometer optical properties. The spectrometer optical properties are approximated by a second order TRANSPORT matrix that relates the target coordinates $\{X_{tgt}, \theta_{tgt}, Y_{tgt}, \phi_{tgt}, \delta\}$ to the focal plane coordinates $\{X_{fp}, \theta_{fp}, Y_{fp}, \phi_{fp}, \delta\}$ by the equation

$$X^i_{fp} = \sum_j M_{ij} X^j_{tgt} + \sum_{j \geq k} T_{ijk} X^j_{tgt} X^k_{tgt} \ , \tag{3.16}$$

where $M_{ij}(T_{ijk})$ is the first(second) order TRANSPORT matrix. The TRANSPORT matrix that describes the spectrometer optics (i.e., it converts the target coordinates to the focal plane coordinates) can also be inverted to the target coordinates from the measured focal plane coordinates:

$$X^i_{tgt} = \sum_j (M_{ij})^{-1} X^j_{fp} + \sum_{j \geq k} (T_{ijk})^{-1} X^j_{fp} X^k_{fp} \ , \tag{3.17}$$

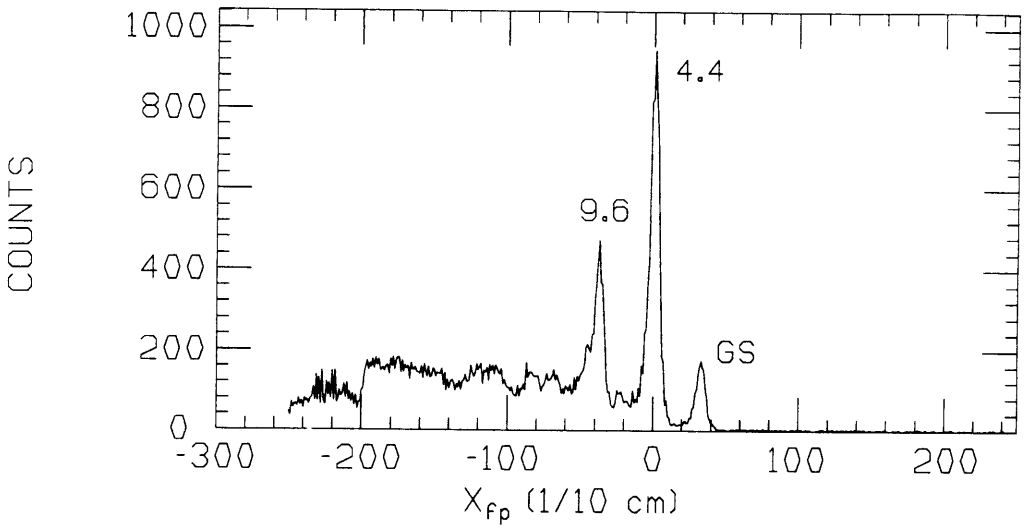

Figure 3-8: The excited states of ^{12}C(e,e') in OHIPS. The peak of the first excited state is used for the calibration.

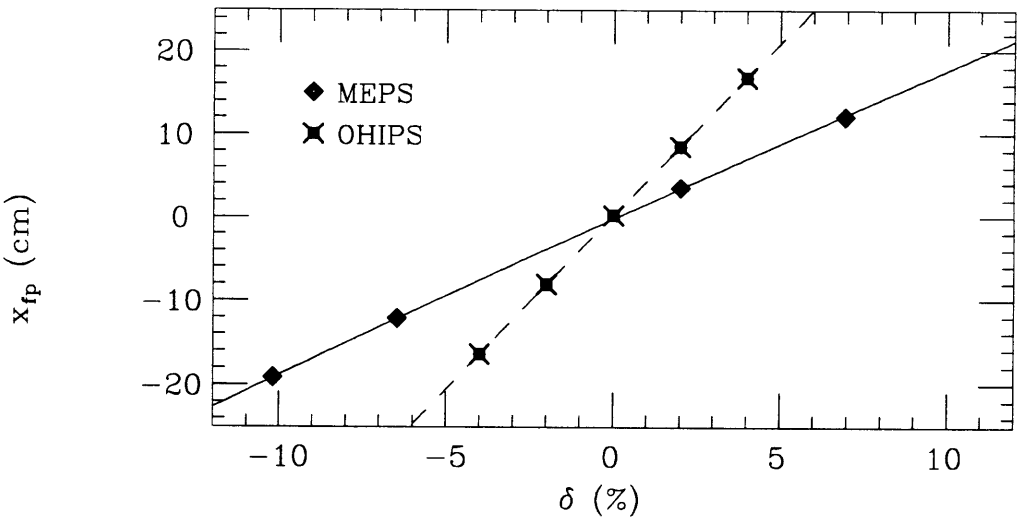

Figure 3-9: Focal plane dispersion calibration data for OHIPS and MEPS.

where $(M_{ij})^{-1}((T_{ijk})^{-1})$ is the inverse of the first(second) order TRANSPORT matrix. Figure 3-10 shows the two coordinate systems as they relate to each other. Both coordinate systems have $\hat{z}$ along the spectrometer's central momentum ray and $\hat{x}$ in the dispersion direction in the magnet's bend plane. θ and ϕ are the angles relative to $\hat{z}$ in the x and y direction, respectively.

A sieve slit is used to measure the matrix elements for both OHIPS and MEPS. This involves placing a collimator with an array of holes in the snout of the spectrometer. Particles passing through the sieve slit holes arrive at the spectrometer focal plane at locations which correspond to the angular positioning of the holes. Since the angular positions of the sieve-slit holes are known, the relation of measured focal plane variables to the target variables can be established. A polynomial expansion is used in this mapping and the coefficients of the expansion are determined from the data by a least-squares fitting procedure.

Figure 3-12 and Figure 3-11 show a histogram of ϕ_{fp}versus. θ_{fp}. The image of the sieve slit holes is clear. Note that the OHIPS sieve-slit was originally designed for the normal mode (large in-plane angular acceptance $\Delta\phi_{tgt}$ and small out-of-plane angular acceptance $\Delta\theta_{tgt}$) with a drift space of 2.0 m. This experiment was run in reverse mode (small in-plane angular acceptance $\Delta\phi_{tgt}$ and large out-of-plane angular acceptance $\Delta\theta_{tgt}$) with a drift space of 1.6 m. In this mode the outer set of holes in the in-plane angular acceptance are not seen. The first and second inverse matrix elements are given in the Table 3.1

3.1.6 Determination of Beam Energy

A determination of the beam energy is is essential to keep systematic error to a minimum for most experiments because calibration of the spectrometers is based on the precise knowledge of the beam energy.

The beam energy is determined by the Energy Compression System (ECS) chicane using an RF cavity to compress the energy spread of the beam. The dipole magnets in this ECS chicane were calibrated in a procedure similar to the Hall probe technique which is discussed in detail in Reference [41]. There are three factors contributing to the uncertainty in the beam energy as determined by the ECS [28]: (1) uncertainty in the central momentum of the chicane due to an uncertainty in the field integral of the central

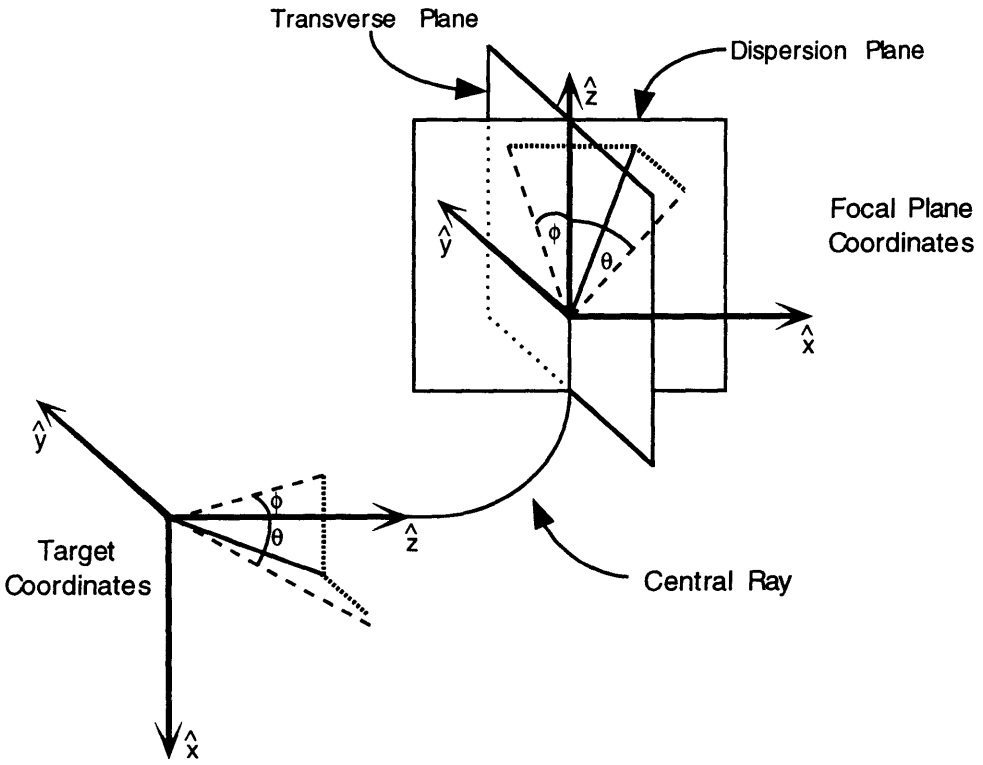

Figure 3-10: Transport Coordinate System

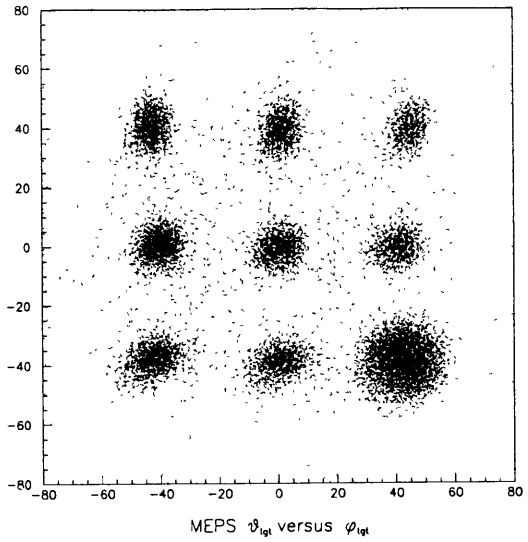

Figure 3-11: Dot plots of θ_{tgt} versus ϕ_{tgt} for MEPS.

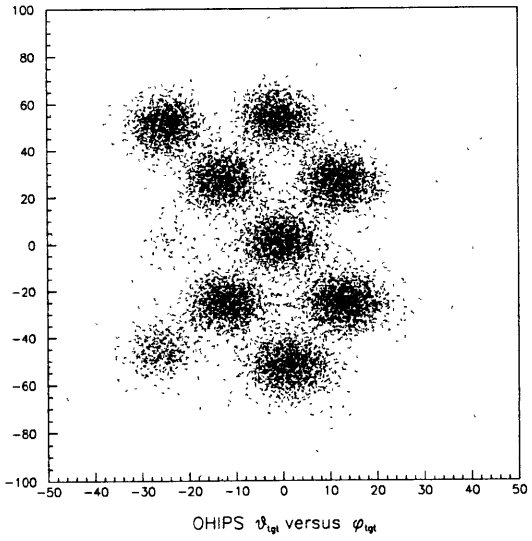

Figure 3-12: Dot plots of θ_{tgt} versus ϕ_{tgt} for OHIPS.

MEPS	
$\langle\delta\|x\rangle$	0.5467 ± 0.0017
$\langle\delta\|x^2\rangle$	0.00054 ± 0.00011
y_0	5.36 ± 0.18
$\langle y\|y\rangle$	-5.83 ± 0.11
$\langle y\|\phi\rangle$	0.782 ± 0.013
$\langle y\|x^2\rangle$	-0.0152 ± 0.0011
θ_0	-11.16 ± 0.12
$\langle\theta\|x\rangle$	0.3112 ± 0.0073
$\langle\theta\|\theta\rangle$	-0.3918 ± 0.0011
$\langle\theta\|x^2\rangle$	-0.01716 ± 0.00066
$\langle\theta\|x\theta\rangle$	0.001993 ± 0.000084
$\langle\theta\|\theta^2\rangle$	0.000328 ± 0.000016
ϕ_0	-3.77 ± 0.11
$\langle\phi\|y\rangle$	-10.741 ± 0.093
$\langle\phi\|\theta\rangle$	-0.0127 ± 0.0014
$\langle\phi\|\phi\rangle$	-0.328 ± 0.012
$\langle\phi\|xy\rangle$	0.1789 ± 0.0042
$\langle\phi\|y\theta\rangle$	0.0141 ± 0.0011
$\langle\phi\|\theta\phi\rangle$	-0.00254 ± 0.00015

OHIPS	
$\langle\delta\|x\rangle$	0.241 ± 0.00014
$\langle\delta\|x^2\rangle$	-0.000057 ± 0.000016
y_0	-1.2 ± 0.018
$\langle y\|y\rangle$	-0.78 ± 0.0024
$\langle y\|\phi\rangle$	0.00691 ± 0.00039
$\langle y\|y\theta\rangle$	0.00307 ± 0.0024
$\langle y\|\theta\phi\rangle$	-0.00091 ± 0.00022
θ_0	19.387 ± 0.066
$\langle\theta\|x\rangle$	4.8601 ± 0.0073
$\langle\theta\|\theta\rangle$	-2.0347 ± 0.0018
$\langle\theta\|x^2\rangle$	-0.04598 ± 0.15
$\langle\theta\|x\theta\rangle$	0.01509 ± 0.042
ϕ_0	8.232 ± 0.0030
$\langle\phi\|y\rangle$	0.3700 ± 0.019
$\langle\phi\|\phi\rangle$	-1.3145 ± 0.019
$\langle\phi\|x\phi\rangle$	-0.005303 ± 0.019
$\langle\phi\|\theta\phi\rangle$	-0.0470 ± 0.019

Table 3.1: Inverse matrix elements for MEPS and OHIPS. The elements are in standard TRANSPORT coordinate units, i.e. centimeters for positions, milliradians for angles and percent for δ.

	MEPS	OHIPS
Angle (deg)	120.29	31.61
Central Mom.(MeV/c) '1'	728.32	264.82
Central Mom.(MeV/c) '2'	743.73	276.28
Central Mom.(MeV/c) '3'	758.60	287.85
Central Mom.(MeV/c) '4'	773.78	299.25
Central Mom.(MeV/c) '5'	788.80	310.44

Table 3.2: Experimental Parameters for the relative focal plane efficiency for MEPS and OHIPS. The incident beam energy is 579.3 MeV.

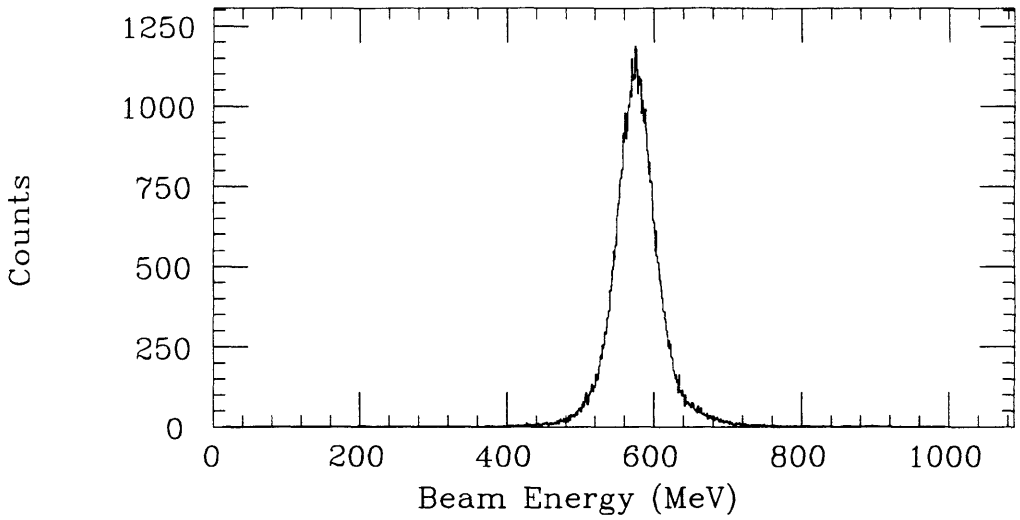

Figure 3-13: Histogram of the beam Energy as calculated using the measured scattering angles from proton elastic scattering

ray; (2) a limited range of beam energies around the central energy to pass through the chicane for the energy defining slits in the ECS; (3) an uncertainty of the phase of the beam with respect to the Radio Frequency electro-magnetic waves (RF) in the cavity after the chicane induced an uncertainty in the central beam energy. The beam energy as determined by the ECS is 579.7 $\pm$ 0.7 MeV.

The beam energy can also be determined experimentally. A technique used in this analysis utilizes the kinematic correlation in electron and proton scattering angles in $H(e,e'p)$ to determine the beam energy. The technique is described in detail in reference [36]. Given the scattering angles θ_e and θ_p of the electron and proton, respectively, in the $H(e,e'p)$ reaction, the beam energy E_{beam} can be calculated by:

$$E_{beam} = 2m_p \frac{\sin\theta_t(\sin\theta_p - \sin\theta_t)}{(\sin\theta_p - \sin\theta_t)^2 - \sin^2\theta_e}\ , \tag{3.18}$$

where $\theta_t \equiv \theta_p + \theta_e$ and m_p is the mass of the proton. Using this formula, the beam energy can be calculated on an event-by-event basis. The beam energy spectrum (shown in the Figure 3-13) has a broad peak due to the angular resolution of the two spectrometers. The beam energy as determined by this technique is 578.2 $\pm$ 5.8 MeV and agrees with the value from ECS at the 0.1% level.

3.1.7 Determination of Focal Plane Efficiencies

Corrections for variations in the focal plane efficiency as a function of δ have to be made since the population of detected particles is not uniform in δ. These variations arise from geometrical limitations of the effective solid angle contributing differently to portions of focal plane. A measurement of the relative efficiency of both the MEPS and OHIPS focal planes is necessary for averaging polarization observables over the finite acceptance of the experiment using Monte Carlo techniques.

In order to determine the relative efficiency of the focal plane, a smoothly varying cross section for several overlapping ranges of momentum is measured. A large amount of overlap between successive measurements insures that every focal plane position samples momenta differing only by small amounts. Since the cross section is slowly varying and the efficiency of a given channel is constant, this provides a determination of the shape of the spectrum being sampled. Furthermore, taking several overlapping measurements implies that the same momentum is sampled by several different channels. Any difference in the measured yield at two channels sampling the same momentum is due entirely to a difference in the efficiencies between the two channels. Thus, the relative efficiency as a function of δ can be determined.

The $^{12}C(e,e')$ cross section measurements are done for MEPS and OHIPS in a series of runs. The quasielastic region is chosen because it has a sufficiently smooth cross section. The experimental parameters used for the relative focal plane efficiency measurements are listed in Table 3.2. The resulting histograms of delta are deconvoluted by the program RELEFF [45]. This program takes the results from all the runs and then fits a polynomial curve to the experimental cross section. This curve is then used to adjust the efficiency of each bin. With the resulting new spectra this process is repeated until the χ^2 of the fit between two successive iterations changes by less than a preset limit, usually 0.001.

The relative focal plane efficiency profile and the cross section for MEPS and OHIPS are presented in Figures 3-14 and 3-15.

3.2 FPP Analysis

The purpose of the FPP analysis is to determine the angular distribution of the secondary scattering and extract proton polarizations at the focal plane. The information from the

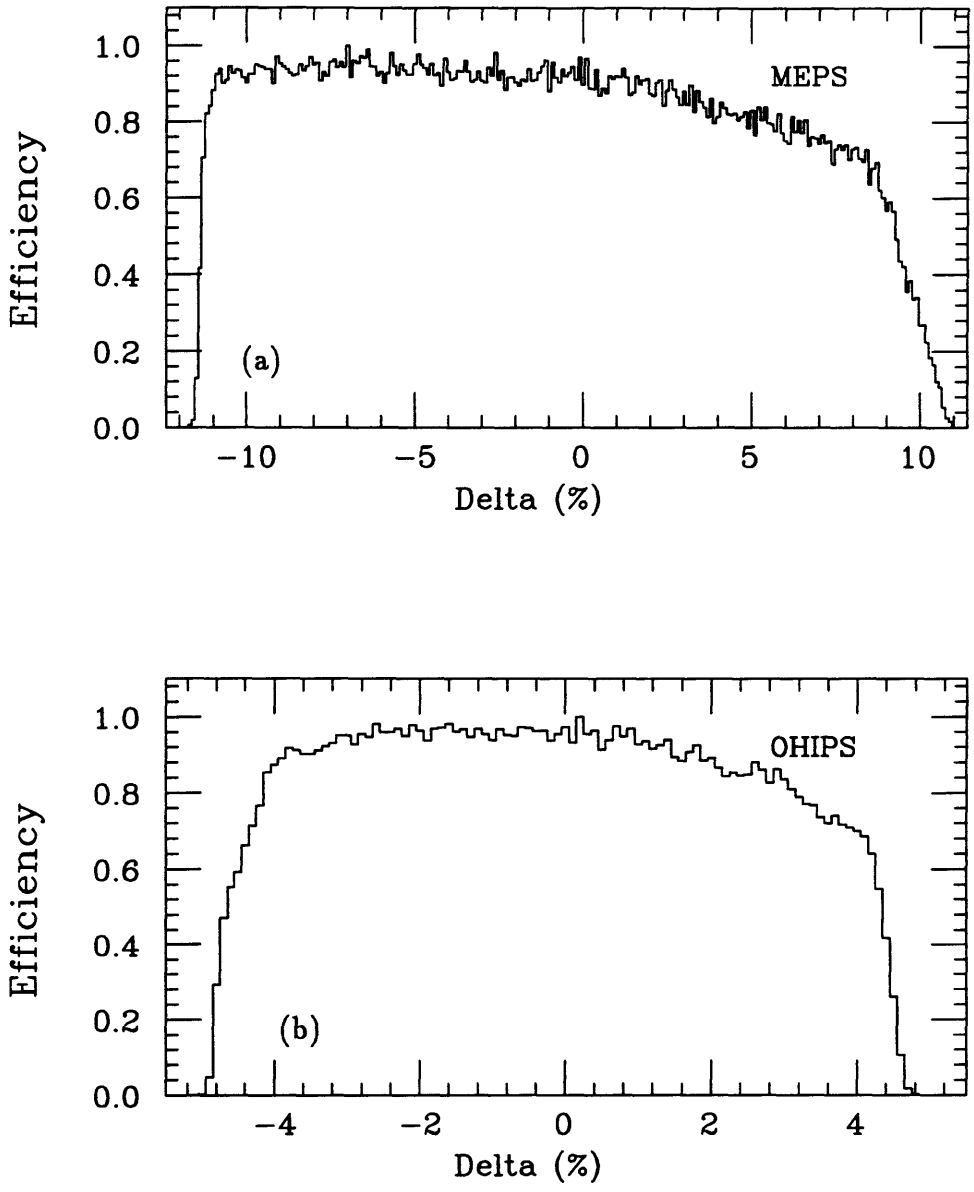

Figure 3-14: Comparison of relative focal plane efficiencies as determined by RELEFF for (a) MEPS and (b) OHIPS. The efficiency curves were scaled so that the maximum efficiency was 1.

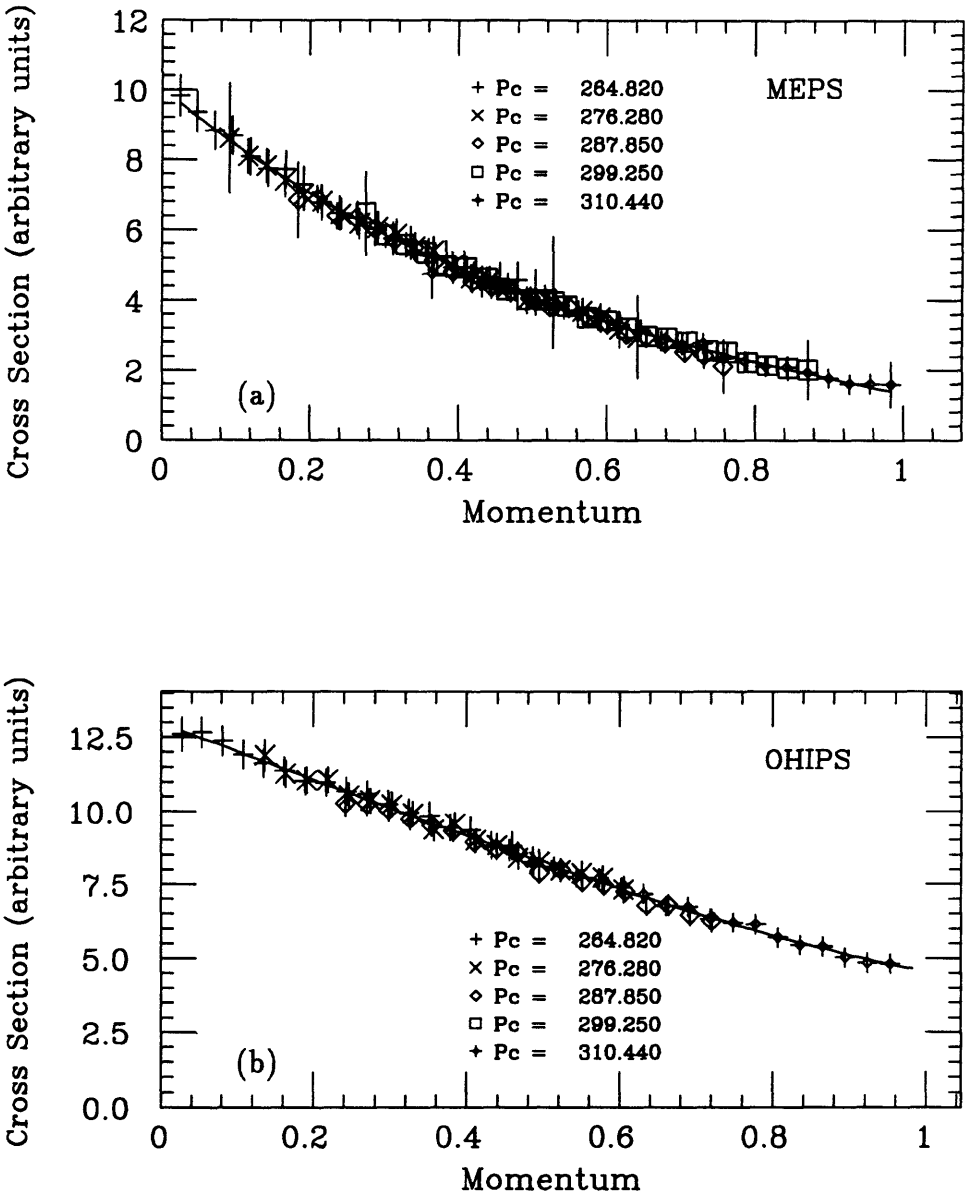

Figure 3-15: Unnormalized $^{12}C(e,e')$ quasi-elastic cross section for a) MEPS and b) OHIPS. The line is the best fit to the points as determined by RELEFF. The momentum scale was determined by setting to 0 and 1 the lowest and highest momentum sampled respectively.

front two FPP Multi-Wire Proportional Chambers(MWPC) is combined with information from the OHIPS VDCX to reconstruct the initial proton trajectory. The information from the back two FPP MWPCs is used to reconstruct the final proton trajectory. The analysis of the information from the FPP MWPCs is described in this section.

3.2.1 Determination of The Secondary Scattering Angle

There are two steps in determination of the secondary scattering angles. The first step is to determine the Cartesian angles of the initial and final trajectory, (α_i, β_i) and (α_f, β_f) once the raw PCOS data are converted into wire numbers. The second step is to convert these Cartesian angles into the polar secondary scattering angles, $\theta_{scat}$and ϕ_{scat}. The coordinate system for the FPP is shown in Figure 3-16.

From the observed chamber event positions and the known distances between the chambers, vectors parallel to the initial and final proton trajectories, $\vec{i}$ and $\vec{f}$ can be constructed. These vectors are normalized so that the third component is unity. The $\{\hat{x}, \hat{y}, \hat{z}\}$ coordinate system of the FPP, where $\hat{x}$ is along X_{fp} and $\hat{y}$ is along Y_{fp}, is chosen as shown in Figure 3-16. The initial and final trajectories are

$$\vec{i} = (\tan\alpha_i, \tan\beta_i, 1) \tag{3.19}$$

$$\vec{f} = (\tan\alpha_f, \tan\beta_f, 1)\,. \tag{3.20}$$

After initial and final trajectories are given, the secondary scattering angles, $\theta_{scat}$and ϕ_{scat} can be calculated. The polar scattering angle, $\theta_{scat}$is given by a simple formula:

$$\theta_{scat} = \cos^{-1}\left(\frac{\vec{i}\cdot\vec{f}}{\left|\vec{i}\right|\left|\vec{f}\right|}\right). \tag{3.21}$$

The determination of the azimuthal angle is more complicated because ϕ_{scat} is defined in the plane which is not parallel to the plane of the wire chamber systems. The new coordinate system, $\{\hat{x}', \hat{y}', \hat{z}'\}$ must be defined for the secondary scattering where $\hat{z}'$ lies along the initial trajectory $\vec{i}$ of the proton, and $\hat{x}'$ is perpendicular to $\hat{z}'$ and $\hat{y}$. $\hat{z}'$ is

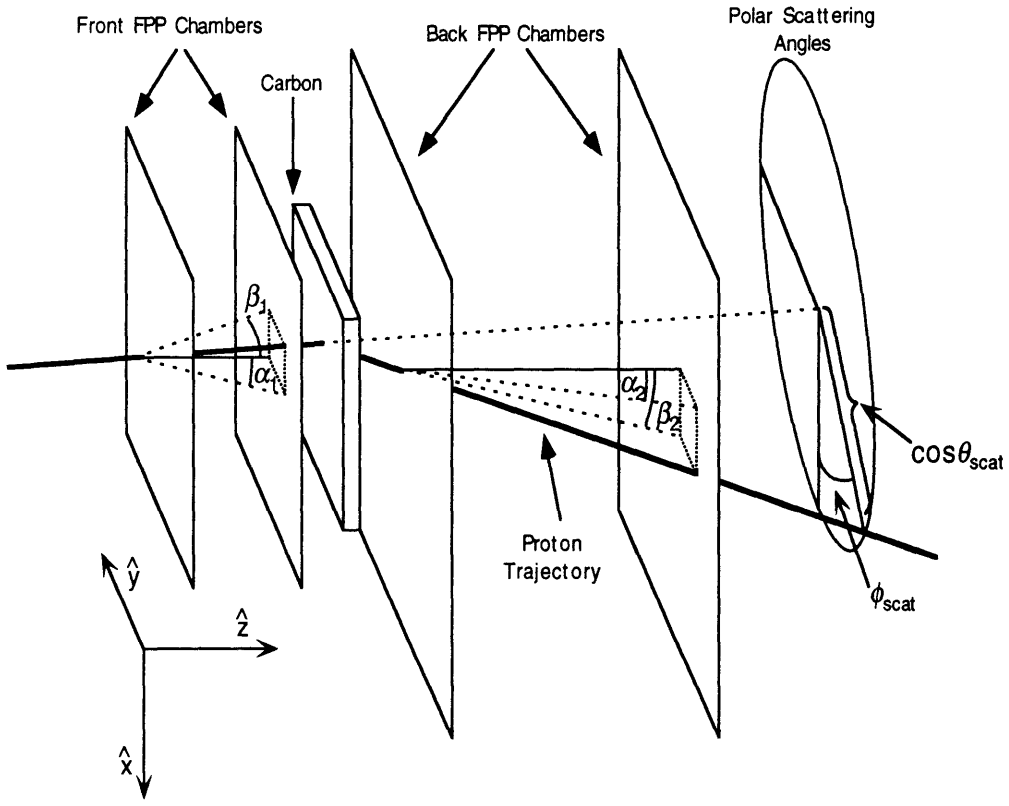

Figure 3-16: Coordinate system for the Focal Plane Polarimeter. The proton travels from the left to the right of the figure. $\hat{y}$ points in to the page.

different for each event, though the variation is small. By definition, $\phi_{scat} = 0$ along $\hat{x}'$. The unit vectors of the coordinate system of the secondary scattering are

$$\hat{z}' = \frac{\vec{i}}{\left|\vec{i}\right|} = \frac{(\tan\alpha_i, \tan\beta_i, 1)}{\sqrt{1+\tan^2\alpha_i+\tan^2\beta_i}}, \tag{3.22}$$

$$\hat{x}' = \frac{\hat{y}\times\hat{z}'}{|\hat{y}\times\hat{z}'|} = \frac{(1, 0, -\tan\alpha_i)}{\sqrt{1+\tan^2\alpha_i}}, \tag{3.23}$$

$$\hat{y}' = \frac{\hat{z}'\times\hat{x}'}{|\hat{z}'\times\hat{x}'|} = \frac{(-\tan\alpha_i\tan\beta_i, 1+\tan^2\alpha_i, -\tan\beta_i)}{\sqrt{(1+\tan^2\alpha_i+\tan^2\beta_i)(1+\tan^2\alpha_i)}}. \tag{3.24}$$

In this coordinate system, the relationships

$$\begin{aligned} \vec{f}\cdot\hat{x}' &= \left|\vec{f}\right|\sin\theta_{scat}\cos\phi_{scat}, \\ \vec{f}\cdot\hat{y}' &= \left|\vec{f}\right|\sin\theta_{scat}\sin\phi_{scat} \end{aligned} \tag{3.25}$$

lead to the azimuthal scattering angle ϕ_{scat}

$$\begin{aligned} \tan\phi_{scat} &= \frac{\vec{f}\cdot\hat{y}'}{\vec{f}\cdot\hat{x}'}, \\ &= \frac{\tan\beta_f - \tan\beta_i + \tan\alpha_i(\tan\alpha_i\tan\beta_f - \tan\beta_i\tan\alpha_f)}{\sqrt{1+\tan^2\alpha_i+\tan^2\beta_i}(\tan\alpha_f - \tan\alpha_i)}. \end{aligned} \tag{3.26}$$

3.2.2 Extraction of Polarizations at the Focal Plane

The proton polarizations at the focal plane are extracted by Fourier Analysis of the angular distribution of $\vec{p} - {}^{12}\mathrm{C}$ scattering. The angular distribution is written as:

$$I(\theta,\phi) = I_0(\theta)\left[1 + P_x^{fp}A_y(\theta)\sin\phi + P_y^{fp}A_y(\theta)\cos\phi\right], \tag{3.27}$$

where P_x^{fp} and P_y^{fp} are the normal and transverse polarization measured at the focal plane, A_y is the analyzing power and I_0 is the polarization independent term. Since the measured proton polarizations is the event-averaged value, Equation 3.27 can be written

as:

$$\langle I(\theta,\phi)\rangle = I_0\left[1+\epsilon_x\sin\phi+\epsilon_y\cos\phi\right] , \tag{3.28}$$

where the physics asymmetry is $\epsilon_{(x,y)} = P^{fp}_{(x,y)}\langle A_y\rangle$. $\langle A_y\rangle$ is the event-averaged analyzing power. The measured angular distribution is, however, a product of the event-averaged distribution for $\vec{p}\,^{-12}C$, $\langle I(\theta,\phi)\rangle$, and the instrumental asymmetries, $\xi(\theta,\phi)$. The instrumental asymmetries, $\xi(\theta,\phi)$, can be expanded as

$$\xi(\theta,\phi) = \left[1+\sum_{m\geq 1} e_m(\theta)\cos(m\phi)+\sum_{m\geq 1}\bar{e}_m(\theta)\sin(m\phi)\right] . \tag{3.29}$$

Then the measured angular distribution is

$$\begin{aligned} N(\theta,\phi) &= \langle I(\theta,\phi)\rangle\xi(\theta,\phi), && (3.30)\\ &= \langle I(\theta,\phi)\rangle\left[1+\epsilon_x\sin\phi+\epsilon_y\cos\phi\right]\times \\ &\qquad \left[1+\sum_{m\geq 1} e_m(\theta)\cos(m\phi)+\sum_{m\geq 1}\bar{e}_m(\theta)\sin(m\phi)\right], && (3.31)\\ &= \langle I(\theta,\phi)\rangle\left[1+2\sum_{n\geq 1} u_m\cos(n\phi)+2\sum_{n\geq 1} v_m\sin(n\phi)\right] , && (3.32) \end{aligned}$$

where the weighted integrals, u_n and v_n are defined as

$$\begin{aligned} u_n &\equiv \int_0^{2\pi} N(\theta,\phi)\cos(n\phi)d\phi \Big/ \int_0^{2\pi} N(\theta,\phi)d\phi, && (3.33)\\ v_n &\equiv \int_0^{2\pi} N(\theta,\phi)\sin(n\phi)d\phi \Big/ \int_0^{2\pi} N(\theta,\phi)d\phi\,. && (3.34) \end{aligned}$$

Since physics asymmetries $\epsilon_{(x,y)}$ have only $\cos\phi$ and $\sin\phi$ terms, only $n = 1$ coefficients matter in this expansion. The weighted integrals for n = 1 are

$$\begin{aligned} u_1 &= \frac{\epsilon_y(2+e_2)+\epsilon_x\bar{e}_2+2e_1}{4+2\epsilon_y e_1+2\epsilon_x\bar{e}_1}, && (3.35)\\ v_1 &= \frac{\epsilon_x(2-e_2)+\epsilon_y\bar{e}_2+2\bar{e}_1}{4+2\epsilon_y e_1+2\epsilon_x\bar{e}_1}. && (3.36) \end{aligned}$$

Equations 3.35 and 3.36 can be expressed as two linear equations with two unknowns:

$$\begin{pmatrix} \epsilon_y \\ \epsilon_x \end{pmatrix} = \begin{pmatrix} 1 - \frac{1}{2}e_2 + u_1 e_1 & -\frac{1}{2}\bar{e}_2 + u_1 \bar{e}_1 \\ -\frac{1}{2}\bar{e}_2 + v_1 e_1 & 1 + \frac{1}{2}e_2 + v_1 \bar{e}_1 \end{pmatrix} \begin{pmatrix} 2u_1 - e_1 \\ 2v_1 - \bar{e}_1 \end{pmatrix}. \tag{3.37}$$

To get the physics asymmetries $\epsilon_{(x,y)}$ from Equation 3.37, the weighted integrals, u_1 and v_1, and instrumental asymmetry terms $e_{(1,2)}$ and $\bar{e}_{(1,2)}$ need to be measured. The weighted integrals u_1 and v_1 are estimated by the polarimetry measurement:

$$u_m = \frac{1}{N}\sum \cos(m\phi), \tag{3.38}$$

$$v_m = \frac{1}{N}\sum \sin(m\phi), \tag{3.39}$$

where the sum is over the events and N is the total number of events. The instrumental asymmetry terms $e_{(1,2)}$ and $\bar{e}_{(1,2)}$ are determined by a separate analysis of elastic scattering off the proton. This procedure is discussed in more detail in the next section.

The error of the physics asymmetries can be estimated by keeping only first order terms in e_m and $\bar{e}_m$ since the instrumental asymmetries are small. The determinant of the matrix in Equation 3.37 is

$$|W| \approx 1 + v_1\bar{e}_1 + u_1 e_1. \tag{3.40}$$

To first order in the instrumental asymmetry terms, an explicit computation gives for the uncertainties of the physics asymmetries, $\sigma_{(y,x)}$,

$$\begin{pmatrix} \sigma_y^2 \\ \sigma_x^2 \end{pmatrix} = \frac{2}{N} \begin{pmatrix} \left(1 + 2u_1 e_1 + v_1\bar{e}_1 - \frac{1}{2}e_2\right)^2 & \left(u_1\bar{e}_1 - \frac{1}{2}\bar{e}_2\right)^2 \\ \left(v_1 e_1 - \frac{1}{2}\bar{e}_2\right)^2 & \left(1 + u_1 e_1 + 2v_1\bar{e}_1 - \frac{1}{2}e_2\right)^2 \end{pmatrix} \times \begin{pmatrix} 1 + u_2 - 2u_1^2 \\ 1 - u_2 - 2u_1^2 \end{pmatrix}. \tag{3.41}$$

The polarizations at the focal plane for each beam helicity and their uncertainties can be calculated using the above results:

$$P^{fp}_{(x,y)} = \frac{\epsilon_{(x,y)}}{\langle A_y \rangle}, \tag{3.42}$$

$$\sigma(P^{fp}_{(x,y)}) = \frac{\sigma(\epsilon_{(x,y)})}{\langle A_y \rangle}. \tag{3.43}$$

3.2.3 Determination of Instrumental Asymmetries

The instrumental asymmetries can result from spatial inefficiencies, residual chamber misalignment and different efficiencies among the three rear scintillators. They can be estimated by measuring the final state proton polarizations for elastically scattering unpolarized electrons off hydrogen. Since there is no spin transfer with unpolarized electrons, only the induced polarization, P_n, can be non-zero and furthermore P_n must also be zero without final-state interactions in coplanar kinematics.

In fact, these measurements were performed with polarized electrons, but an effectively unpolarized electron beam is formed by summing two beam helicities. The total charge for each beam helicity, monitored by beam toroids, differed by 0.15% while the beam helicity as measured by the Møller polarimeter was approximately 30%. The net polarization of the beam was therefore less than 0.0005.

One difficulty in using hydrogen elastic scattering data is that since the instrumental asymmetries are determined from a narrow range of the focal plane of OHIPS, there is a possibility of local variations in the instrumental asymmetries for inelastic reactions in which the focal plane of OHIPS is broadly illuminated. To understand these variations between elastic and inelastic reactions, the final state proton polarization measurement for quasielastically scattering unpolarized electrons from deuterium is used, since the induced polarization for quasielastic scattering of deuteron is non-zero, but is predicted to be small. The results of an analysis for the instrumental asymmetry terms are listed in Table 3.3. The comparison between proton and deuteron instrumental asymmetry terms appears to be consistent with statistical fluctuations. The final values for the instrumental asymmetry terms used in this analysis are the weighted averages of the proton and deuteron.

	proton	deuteron	final value
e_1 $(\cos\phi)$	0.0047 ± 0.0012	0.0021 ± 0.0025	0.0042 ± 0.0046
$\bar{e}_1$ $(\sin\phi)$	0.0019 ± 0.0012	-0.0007 ± 0.0025	0.0014 ± 0.0046
e_2 $(\cos 2\phi)$	-0.0093 ± 0.0012	-0.0115 ± 0.0025	-0.0097 ± 0.0043
$\bar{e}_2$ $(\sin 2\phi)$	0.0004 ± 0.0012	-0.0002 ± 0.0025	0.0003 ± 0.0030

Table 3.3: Instrumental asymmetry terms as measured from scattering off the proton and deuteron and the values used for this analysis.

3.2.4 Analyzing Power

The physics asymmetry $\epsilon_{(x,y)}$ measured at the focal plane is a product of proton polarization, $P^{fp}_{(x,y)}$, and the event-averaged analyzing power, $\langle A_y \rangle$. Thus the proton polarization can be extracted provided the analyzing power is known. The previous measurements of the analyzing power for the $\vec{p} - C$ reaction have been made over a wide range of proton energies between 100 MeV and 800 MeV, scattering angles between 5° and 20°, and carbon analyzer thicknesses between 3cm and 27cm. [51, 52, 53, 54, 55]

The independent calibration of the FPP was performed at the Indiana University Cyclotron Facility (IUCF), with proton beams of known polarization and energy during February 1993. [56] This calibration was done using four energies, 120, 150, 180 and 200 MeV with low intensity polarized beam ($\sim 10^5$ protons per second). The polarimeter was illuminated at different incident angles to study the spatial inefficiencies over the entire active area. The beam polarization as measured by the FPP is compared to that as measured by IUCF beam polarimeter. The ratio for 200 MeV is

$$FPP/IUCF = 0.976 \pm 0.006 , \tag{3.44}$$

where instrumental asymmetries are cancelled out by flipping the polarization of the beam. A more significant measurement which includes the instrumental asymmetries is the ratio of spin-up to spin-down polarization. This ratio as measured by the FPP compared to the IUCF polarimeter is

$$FPP/IUCF = 1.018 \pm 0.011 . \tag{3.45}$$

Thus the performance of the FPP is consistent with the design goal of 2%. A comparison of the asymmetry(proton polarization times analyzing power) measured by FPP at IUCF is also made to that measured at LAMPF [53] and SIN [51] as shown in Figure 3-17.

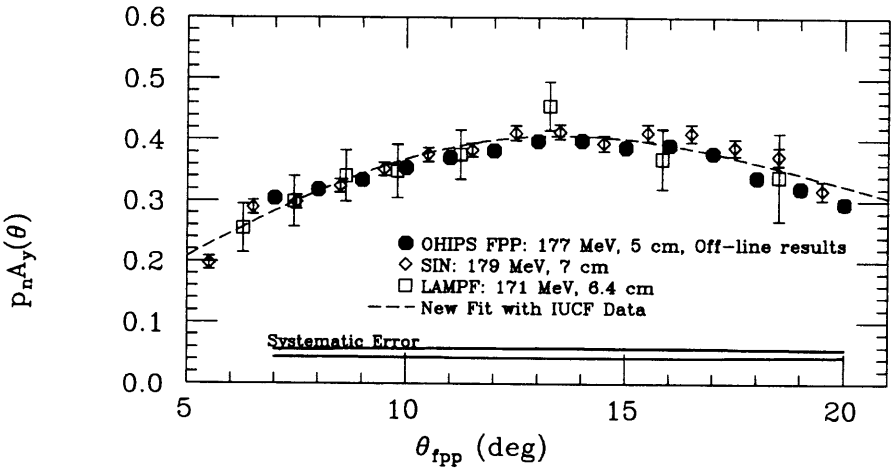

Figure 3-17: Product of Proton polarization and the analyzing power vs. θ_{scat} for the calibration of FPP of $T_p^c = 177$ MeV at IUCF. Energies listed are the kinetic energies at the center of the carbon. The SIN are data from Aprile-Giboni *et alia.* The LAMPF data are from McNaughton *et alia.*

The analyzing power is determined in this analysis from the results of a calibration of the FPP as obtained at IUCF combined with the existing world's data of the $\vec{p} - {}^{12}C$ analyzing power from the two of the most recent fits in the relevant energy range which can be found in Aprile-Giboni *et alia* [51] and McNaughton *et alia* [53]. These two fits used different functional forms to parameterize analyzing power.

The first function introduced by Ransome and used later by McNaughton depends on the scattering angle θ and the momentum of the proton at the center of the carbon:

$$A_y\left(T_p^c, \theta\right) = \frac{ar}{1 + br^2 + cr^4}, \tag{3.46}$$

where a, b and c are fourth order polynomials of $p_c' = p_c - 0.7$ GeV/c, p_c is the momentum of the proton at the center of the carbon and $r = p_c \sin\theta$. This parameterization is referred to as NIM241.

The second function introduced by Aprile-Giboni depends on the scattering angle θ and the kinetic energy $T_{central}$:

$$A_y\left(T_p^c,\theta\right) = D\left(T_p^c,\theta\right)\alpha\left[\frac{\sin(\theta)}{1+\beta\sin^2\theta+\gamma\sin^4\theta}\right], \tag{3.47}$$

where α, β and γ are fourth order polynomials of the dimensionless variable $X = (T_p^c - T_{central})/T_{range}$. For this fit, $T_{central} = 250$ MeV and $T_{range} = 100$ MeV. D is a damping factor included to produce a sharp drop in the analyzing power for small θ and low energy where spin independent multiple Coulomb scattering is dominant. This term can be ignored because there are no data below 7° and D is very close to 1 above 7°. This parameterization is referred to as NIM215.

The two databases of analyzing power are fit to each of the two functional forms. The first database is referred to as the 'wide' database and includes sets of data at T_p^c between 95 MeV and 483 MeV which was used in the fit of McNaughton et al. The SIN $T_p^c = 187$ MeV data set which used a 5 cm carbon analyzer is also added to this database. The second database referred to as 'narrow' database includes the results of the FPP calibration of $T_p^c = 177$ MeV data from IUCF but excludes data at energies outside the range of T_p^c from 155 MeV to 300 MeV. This includes the energy range covered by all experiments conducted with the FPP during 1995. The range of the polar scattering angle is restricted to the range of $5° < \theta < 20°$. The results of the fits are shown in Table 3.4.

The error of the fits is determined by using δ_{exp} defined in Aprile-Giboni to be

$$\delta_{exp} = \frac{\sum_\theta w(\theta)A_{fit}(\theta)A_{exp}(\theta)}{\sum_\theta w(\theta)A_{fit}(\theta)^2}, \tag{3.48}$$

where $w(\theta) = 1/\sigma_\theta^2$ is the statistical weight of each experiment point. This is a deviation factor (δ_{exp} = data/fit) between the measured data and fitted formula. δ_{exp} is calculated for each data set. The fitting errors, (1-δ_{exp}) are generally distributed around a mean, μ_{fit} with a width of a standard deviation, σ_{fit}. The fitting error is estimated by the sum of the mean and one standard deviation, $\mu_{fit} + \sigma_{fit}$. The errors of the fit and χ^2 per degree of freedom are listed in Table 3.4.

The four fits using two forms for two database ('wide' and 'narrow') are performed. The results of each fit for the event-averaged analyzing powers are listed in Table 3.5.

NIM215			NIM241		
	Narrow	Wide		Narrow	Wide
α_0	3.8216	3.8415	a_0	5.3902	5.4479
α_1	0.43410	0.32772	a_1	-4.5980	-3.7223
α_2	0.0	-0.22827	a_2	0.0	-15.200
α_3	0.0	0.0893140	a_3	0.0	45.891
α_4	0.0	0.0	a_4	0.0	0.0
β_0	-6.0782	-5.8801	b_0	-10.691	-9.3937
β_1	0.0	-3.0705	b_1	-92.415	-50.073
β_2	17.527	9.9698	b_2	1838.7	867.30
β_3	-15.922	-2.9130	b_3	0.0	-2731.3
β_4	-22.601	0.89766	b_4	-75781.	4137.5
γ_0	303.85	300.68	c_0	1059.6	1026.2
γ_1	274.77	283.21	c_1	3180.5	1488.5
γ_2	-126.85	-56.700	c_2	-48043	-21193.
γ_3	0.0	-33.788	c_3	-174475	44996.
γ_4	208.73	6.6796	c_4	2851120	-34560.
χ^2/d.o.f.	1.55	1.46		1.55	1.50
Error	1.4%	1.6%		1.6%	1.7%

Table 3.4: Parameters for two functional forms of NIM215 and NIM241 for the two databases. The Error shown is valid for $T_p^c > 150$ MeV only.

	$< A_y >_{true}$	$< A_y >_{accd}$
NIM215 form with Wide Database	0.5615	0.5628
NIM241 form with Wide Database	0.5632	0.5601
NIM215 form with Narrow Database	0.5621	0.5617
NIM241 form with Narrow Database	0.5645	0.5629

Table 3.5: Event-averaged analyzing power for true and accidental events. Results from the four new fits and from the published low energy fit of McNaughton are listed.

The fit to the 'narrow' database of the NIM215 form is chosen for the model of the analyzing power because the error of this fit is lowest. An additional systematic error of 0.10% is added lineally to the error of the fit to account for the model dependence of the fits of the NIM215 and NIM241 forms. The total systematic error of the model of the analyzing power is 1.50%.

3.3 Software Cuts and Background Subtraction

With an understanding of the behavior of the two spectrometers and the FPP, this section will discuss data selection and background subtraction. To make an accurate measurement of proton polarizations of the $D(\vec{e}, e'\vec{p})$ reaction, there are three types of tests applied on the data:

1. Determination of the coincidence timing.
2. Identification of the np final state.
3. Determination of a good FPP event.

Following the data selection, the subtraction for accidental coincidences is performed.

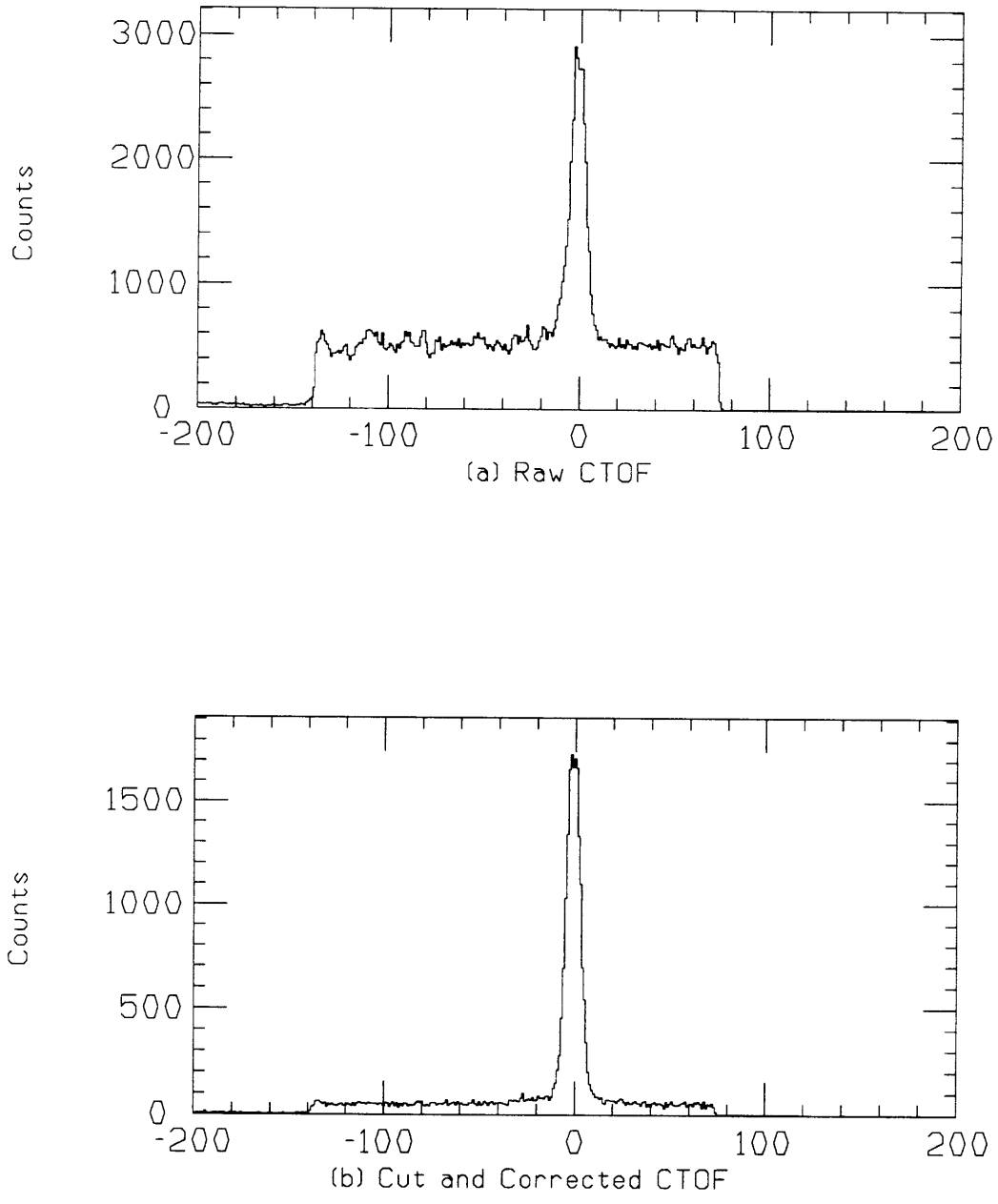

Figure 3-18: Sample histogram of CTOFs.

3.3.1 Determination of the Coincidence Timing

Coincident events between the electron and proton associated with a $D(\vec{e}, e'\vec{p})$ reaction are identified by the relative timing of triggers of the two spectrometers which is referred to as coincidence-time-of-flight (CTOF). The CTOF is started on the discriminated FS1A PMT signal and stopped on the discriminated MS3A PMT signal. Scattered electrons and protons are detected within an 80 ns timing window. The result is shown in Figure 3-18. Accidental coincidences from uncorrelated events uniformly populate a time window at low rates. True coincidences from correlated events form a peak in the spectrum and are thus distinguished from most accidental coincidences. By cutting on this peak, the contribution from accidental coincidences can significantly be reduced. These events which survive this cut are referred to as real coincidences. The real coincidences contain true coincidences and accidental coincidences.

Finding true coincidences requires a subtraction of accidental coincidences inside the timing window containing the peak. Since the average value of accidental coincidences, $\langle N_a \rangle$, is determined from events outside the timing peak, the error in the true coincidences still contains a contribution from the sampling error of accidental coincidences inside the timing peak. The number of true coincidences and the error are determined:

$$N_t = N_r - \langle N_a \rangle W_t \tag{3.49}$$

$$\Delta N_t = \sqrt{N_t} \cdot \left(1 + \frac{1 + W_a/W_a}{N_t/N_a}\right)^{1/2}, \tag{3.50}$$

where N_t is the number of true coincidences, N_r is the number of real coincidences and $N_a = \langle N_a \rangle W_t$ is the estimated number of accidental coincidences inside the window of true coincidences. W_t is the width of the timing peak and W_a is the width of the window containing only accidentals (i.e., in the flat region of the spectrum), which is used to calculate $\langle N_a \rangle$. The ratio of true coincidences to accidental coincidences is improved by minimizing the width of the timing peak, W_t.

There are several factors that tend to broaden the timing peak: (1) particle path lengths, (2) particle velocities, and (3) trigger timing response and electronic noises. The timing peak can be narrowed by making numerical corrections in which the CTOF data are fit to all focal plane coordinates and scintillator ADC and TDC information using the

TRIUMF utility PLOTDATA. The numerically corrected CTOF is calculated for each event:

$$\begin{aligned} CTOF_{corr} = CTOF &- 0.304 \cdot X^O_{fp} &&- 0.251 \cdot \theta^O_{fp} \\ &- 0.0342 \cdot X^M_{fp} &&+ 0.0154 \cdot \theta^M_{fp} \\ &+ 0.365 \cdot TDC_{O1A} &&- 0.353 \cdot TDC_{O1B} \\ &- 0.556 \cdot TDC_{M3A} &&- 0.623 \cdot TDC_{M3B}, \end{aligned} \tag{3.51}$$

where superscript "O" and "M" denote coordinates in OHIPS and MEPS. The half maximum (FWHM) is reduced from 3.8 ns to 2.7 ns by this correction, see Figure 3-18(b).

Three cuts are placed on CTOF histogram to define real coincidences and accidental coincidences as shown in Figure 3-18. The width of the timing peak cut is determined so that the error of polarization measurements is minimized. Two cuts for accidental coincidences are placed far outside the timing peak so that true coincidences be excluded.

3.3.2 Identification of the np final state

In this section, the method used to identify the np final state will be discussed. Several solutions are available, but they all essentially follow from the application of four-momentum conservation. From the four-momentum conservation, the missing energy is defined as follows:

$$E_{miss} \equiv \omega - E' - \sqrt{(\vec{p}' - \vec{q})^2 + M_n^2} + M_p + M_n, \tag{3.52}$$

is equal to the binding energy of the deuteron:

$$E_{miss} = M_p + M_n - M_d \approx 2.225 MeV. \tag{3.53}$$

Figure 3-19 is a plot of for missing energy histograms. Figure 3-19(a) is for raw coincidences, Figure 3-19(b) for real coincidences, Figure 3-19(c) for accidental coincidences and Figure 3-19(d) for true coincidences. The peak is centered around the value of the

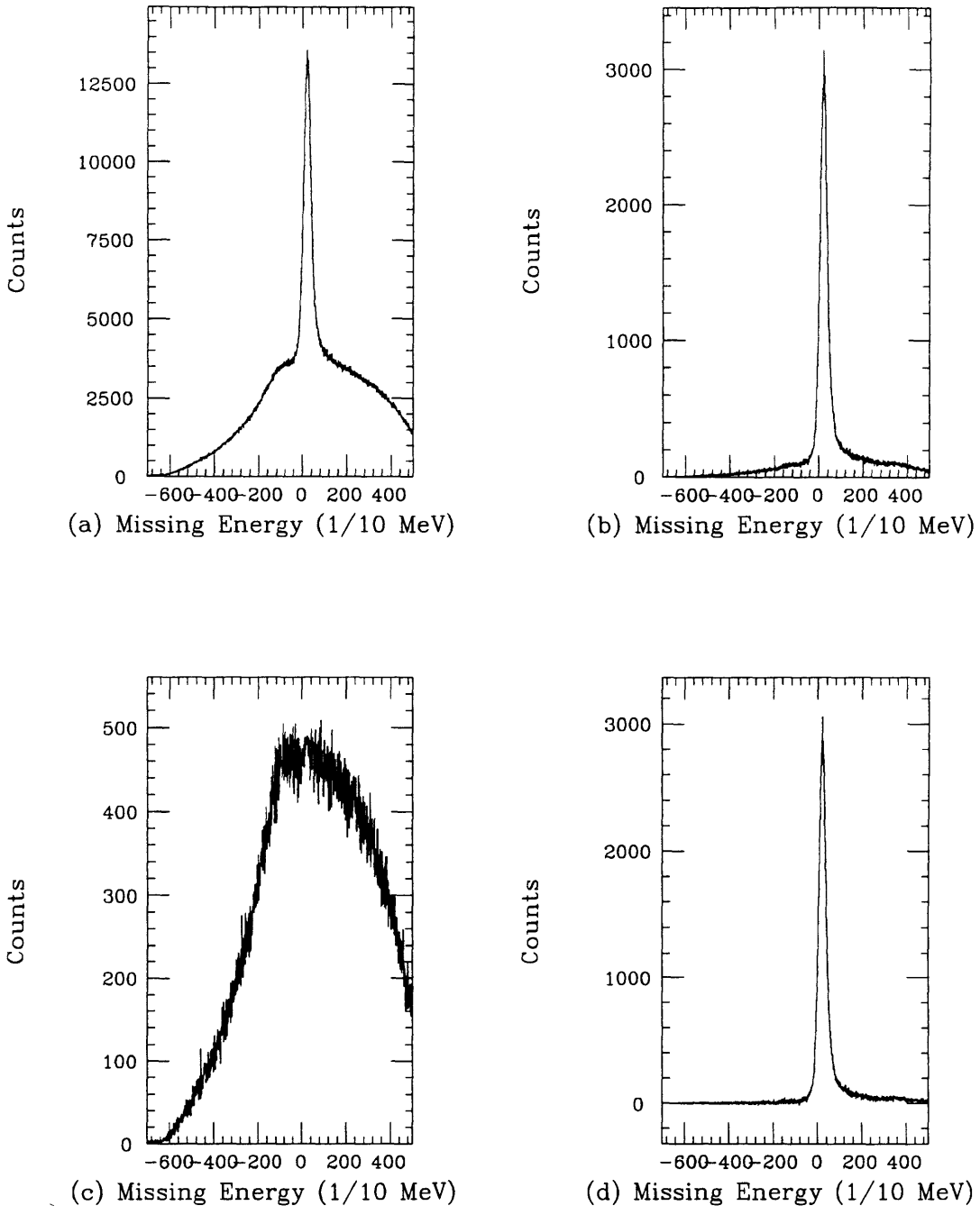

Figure 3-19: Missing Energy Spectrums: (a) Raw Coincidences (b) Real Coincidences (c) Accidental Coincidences (d) True Coincidences

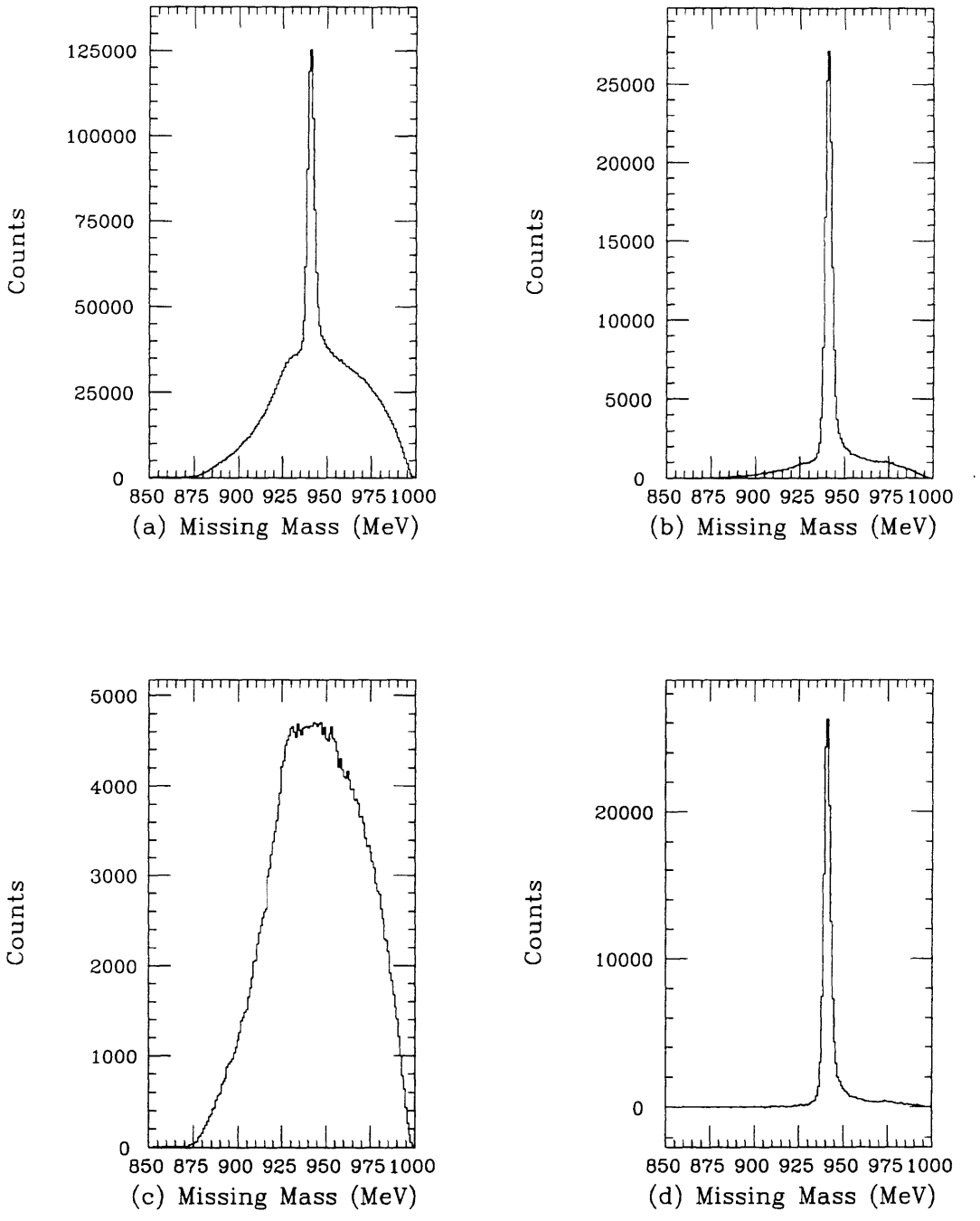

Figure 3-20: Missing Mass Spectrums: (a) Raw Coincidences (b) Real Coincidences (c) Accidental Coincidences (d) True Coincidences

binding energy of the deuteron. By placing a cut on this so called "break-up" peak in the missing energy histogram, the np final state can be identified. The cut made on missing energy is: $0 < E_m < 6.0$ MeV.

Alternatively, the missing mass, M_{miss} which is analogous to the missing energy, E_{miss}, is defined as follows:

$$M^2_{miss} = (\omega + M_d - E')^2 + (\vec{p}' - \vec{q})^2 \ , \tag{3.54}$$

where E' and $\vec{p}'$ are the total energy and momentum of recoil particle. Figure 3-20 is a plot of four missing mass histograms in the same way as that of the missing energy. The center of the peak is around the neutron mass. Another cut of $135 < M_{miss} < 145$ MeV, is placed on this peak for np final state.

3.3.3 Determination of good FPP event

There are two tests applied to determine good FPP events. (1) The polar zenithal scattering angle should be in a specified range. (2) The cone test should be satisfied. Both tests are required to introduce no bias in polarimetry measurements.

Since there is little polarization information from small angle events, the Small Angle Rejection System(SARS) in the hardware eliminated all events for which the angle of the secondary scattering is less than 3.5°. Since Cartesian Coordinates are used in SARS, a box cut is implemented whereas a circular one is required to avoid a bias in ϕ_{scat}distribution. Figure 3-21 shows a plot of x versus y where two new coordinates are defined,

$$\begin{aligned} x &= \frac{180}{\pi} \sin\theta_{scat} \cos\phi_{scat}, \\ y &= \frac{180}{\pi} \sin\theta_{scat} \sin\phi_{scat} \ . \end{aligned} \tag{3.55}$$

As shown in Figure 3-21, some events that should have been rejected are accepted and others that should have been accepted are not. This results from misalignment of the chambers. It is, therefore, necessary to find a minimum θ_{scat} to have no bias in the ϕ_{scat} distribution. To find this, x is plotted where SARS rejected events in y and vice versa,

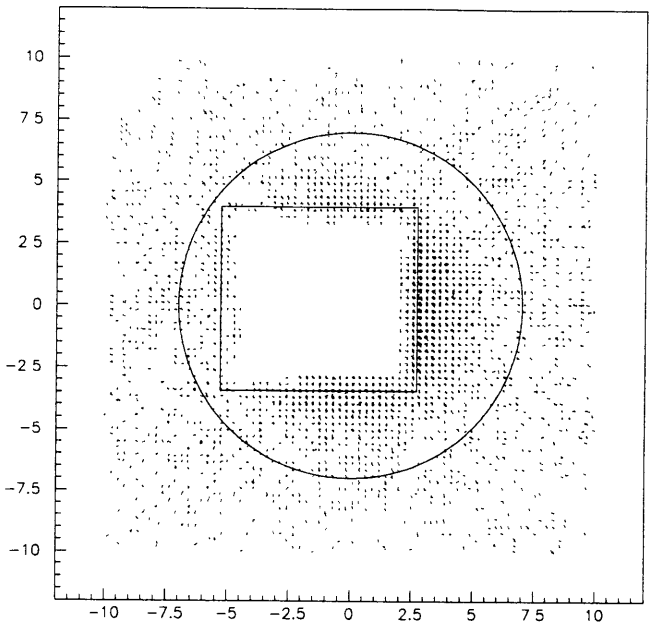

Figure 3-21: The distribution of events in the $\{x, y\}$ coordinate system. The square represents the Cartesian angle cut by the Small Angle Rejection System.

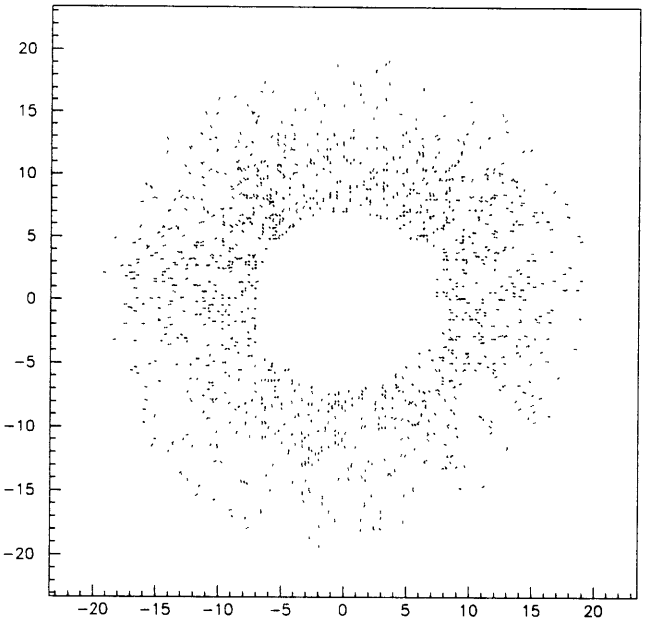

Figure 3-22: The distribution of events in the $\{x, y\}$ coordinate system after software cut is made.

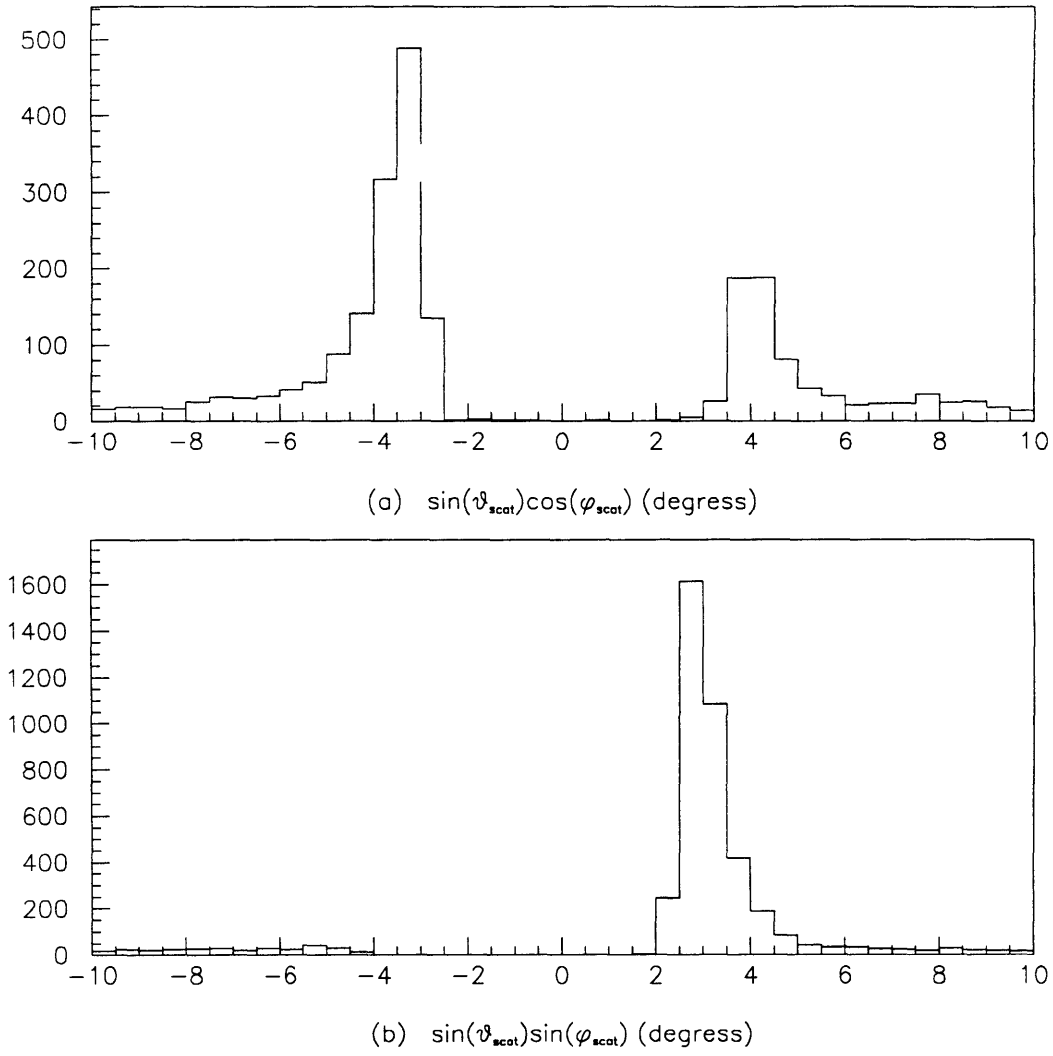

Figure 3-23: The plot of distributions of x and y. (a) shows the projection of x cut on the region y which was rejected by the Small Angle Rejection System and (b) shows vice versa.

as shown in Figure 3-23. Those areas where the distribution of events are decreasing toward zero where bias exists in the data set due to the SARS's Cartesian cut and the misalignment of chambers. Gaussian peaks are taken as the four corners of the box cut and the larger one is chosen in each direction to determine the minimum θ_{scat} which is 6.9°. Since the analyzing power has not been mapped accurately at large angles, 20° is taken to be the maximum θ_{scat} to minimize the uncertainties in the analyzing power models.

Furthermore, the events are required to pass a test on the acceptance of the secondary scattering which is the cone-test, shown in Figure 3-24. A cone is defined by rotating the final trajectory of the proton around the initial trajectory while keeping the polar zenithal scattering angle θ_{scat} fixed. The distance between the location of an actual event in the fourth chamber (the rear detector in the Figure 3-24) and where it would have been if the proton had not been scattered, is a radius of a cone's base. If part of this cone's base lies off the fourth chamber, such as for track B in the Figure 3-24, this event should be eliminated to avoid a bias in the ϕ_{scat} distribution due to the FPP acceptance.

Figure 3-22 shows a plot of x versus y after these two tests are applied.

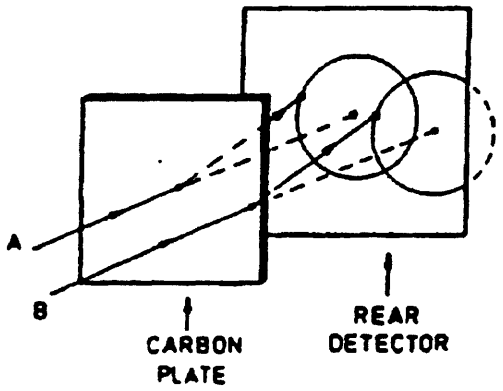

Figure 3-24: cone test

3.3.4 Background Subtraction

The proton polarizations for true coincidences can be determined from those of real and accidental coincidences where the definition of 'true', 'real' and 'accidental' terms have been discussed in the previous section. Thus, it is necessary to make separate measurements of proton polarizations for real and accidental coincidences. Since the coincidence timing window is wide enough ($\approx$ 80 ns), it is possible to measure proton polarizations for accidental coincidences.

The relations between real, true and accidental coincidences can be written

$$N^R = N^T + N^A \tag{3.56}$$
$$N^R \langle A_y \rangle^R = N^T \langle A_y \rangle^T + N^A \langle A_y \rangle^A \tag{3.57}$$
$$N^R P^R \langle A_y \rangle^R = N^T P^T \langle A_y \rangle^T + N^A P^A \langle A_y \rangle^A \,, \tag{3.58}$$

where N^i represents the number of events for i = true or accidental coincidences, P^i represents the proton polarization, and $\langle A_y \rangle^i$ represents the event-average of the analyzing power. Since the kinematic distribution of true and accidental coincidences, $\langle A_y \rangle^T$ is not equal to $\langle A_y \rangle^A$. Solving the above equations for P^T, gives

$$P^T = \frac{[1+\alpha]\, P^R \langle A_y \rangle^T - P^A \langle A_y \rangle^A}{[1+\alpha]\, \langle A_y \rangle^R - \langle A_y \rangle^A} \,, \tag{3.59}$$

where $\alpha = N^T/N^A$ is the signal to noise ratio. Equation 3.59 can be re-written in terms of measured quantities:

$$P^T = \frac{[1+\alpha]\, \epsilon^R - \epsilon^A}{[1+\alpha]\, \langle A_y \rangle^R - \langle A_y \rangle^A} \,, \tag{3.60}$$

where ϵ^R and ϵ^A are the physics asymmetries for real and accidental coincidences as measured with the FPP. The error for P^T is given:

$$\begin{aligned} \sigma^2(P^T) = & \left(\frac{[1+\alpha]}{\alpha \langle A_y \rangle^T} \right)^2 \sigma^2(\epsilon^R) + \left(\frac{1}{\alpha \langle A_y \rangle^T} \right)^2 \sigma^2(\epsilon^A) + \\ & \left(\frac{P^T}{\langle A_y \rangle^T} \right)^2 \sigma^2(\langle A_y \rangle) + \left(\frac{\epsilon^A \langle A_y \rangle^R - \epsilon^R \langle A_y \rangle^A}{\left(\alpha \langle A_y \rangle^T \right)^2} \right)^2 \sigma^2(\alpha) \,, \end{aligned} \tag{3.61}$$

where the error for $\langle A_y \rangle^R$ and $\langle A_y \rangle^A$ is assumed to be dominated by the error of the fit to the analyzing power.

3.4 Determination of Beam Polarization

The beam polarization was measured at least once per day, or whenever any changes were made for parameters of electron polarized sources. It was found that the beam polarization is sensitive to the conditions of the polarized source such as laser wavelength and the location of the laser spot on the crystal. To minimize the systematic uncertainties, beam polarization should be measured if any changes are made for the conditions of the polarized source. The final average value of the beam polarization for this analysis is determined in the following steps: (1) Interpolate the beam polarizations with respect to time between each Møller measurement. (2) Calculate the beam polarization for each run between the two measurements. (3) Take an average weighted by the total charge for each run. The individual beam polarization measurements and the interpolation between each measurment are shown in Figure 3-25.

Each measurement of the beam polarization consists of two scans of the quadrupole magnet field strength at each of the Møller target angles $+30°$ and $-30°$. The first scan, referred to as a wide scan, is taken over a wide range of magnetic field strength in order to establish the amount of background. The second scan, referred to as a narrow scan, is for higher statistics on the signal of Møller scattered electrons. In the analysis of the data, a software cut is made on the beam charge. The large beam charge variation indicates the instability of beam pulses. The cut on beam charge also eliminates the beam pulses with a large variation in beam position. Software cuts are also made for the beam position and beam halo.

The signal to noise ratio is determined using data from the wide scan of the magnetic field strength. The normalized yield is fitted to the form:

$$Y(x) = S \cdot \exp\left[\frac{\left(\frac{-|x-c|}{w}\right)^p}{p}\right] + B(x), \tag{3.62}$$

where x represents the quadrupole field strength. The first term in the function is the signal and the second term, $B(x)$, is the background. Background fits are made with both linear and exponential functions. The linear background function is chosen for the final analysis because the fits are generally better. Figure 3-26 shows a plot of a normalized yield versus magnetic field strength with its fit. The peak signal to background ratio is around 2.0 for these measurements. The variation between the signal to background ratio for the different background functions is used as an estimate for the systematic error in the signal to background fit.

The beam polarization is determined from the narrow scan with the higher statistics using the background fit from the wide scan with the lower statistics. This is done because the narrow scan run covers just a few background points. First, the total signal from the high statistics run is fitted using the background value found from the wide scan and the same functional form, Equation 3.62. This fit provides the final signal to background ratio. Figure 3-27(a) is an example. Then the pulse-pair asymmetry is fitted using that signal to background ratio. The form of this function is,

$$A = A_{meas} \cdot \left[1 + \frac{B(x)}{S(x)}\right], \tag{3.63}$$

where x is the magnetic field strength, $B(x)$ is the background function and $S(x)$ is

$$S(x) = S_0 \cdot \exp\left[\frac{\left(\frac{-|x-c|}{w}\right)^p}{p}\right]. \tag{3.64}$$

$B(x)$ and $S(x)$ take values from the fit on the total signal. Figure 3-28(b) shows the fit of a sample pulse-pair asymmetry.

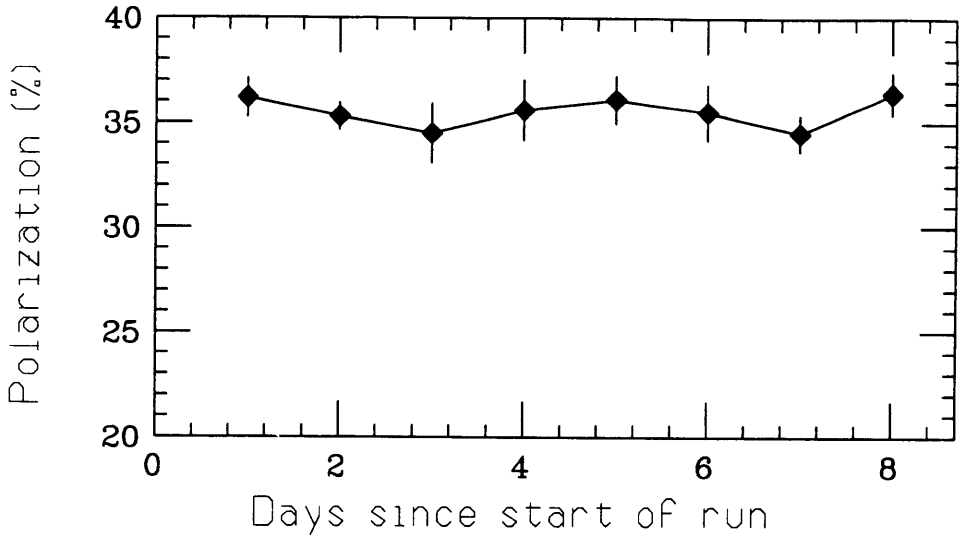

Figure 3-25: Beam polarization versus days since start of run.

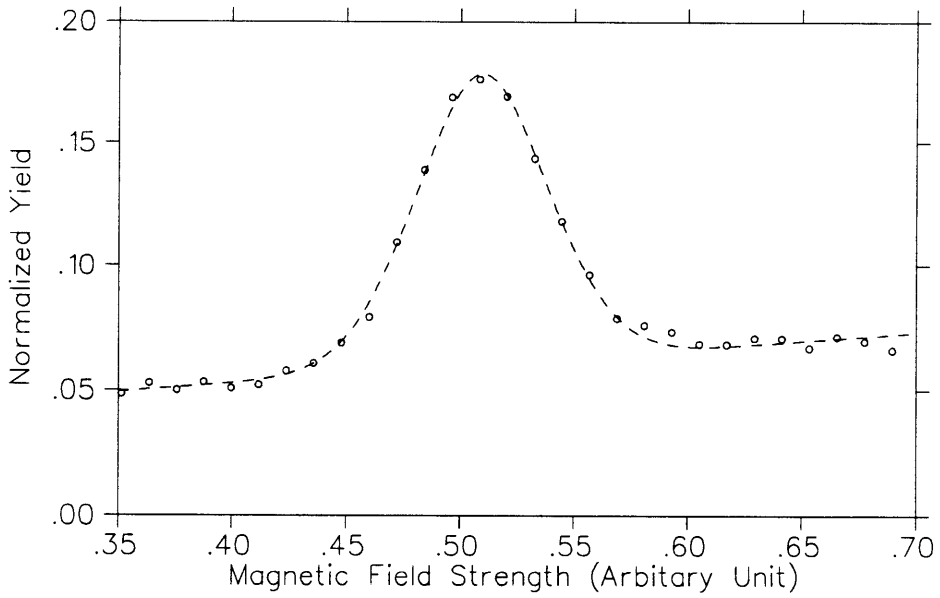

Figure 3-26: Normalized yield versus magnetic field strength for wide scan.

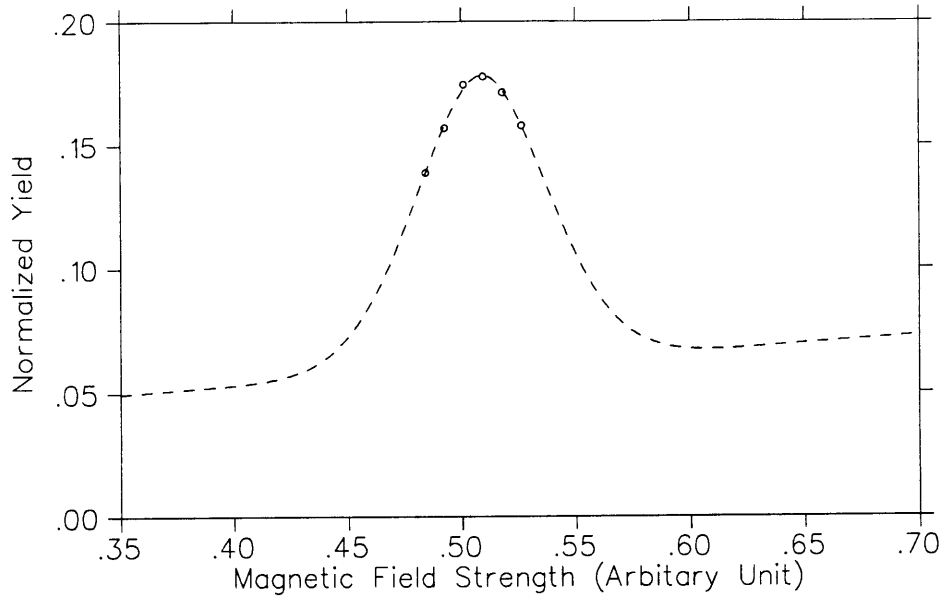

Figure 3-27: Normalized yield versus magnetic field strength for narrow scan.

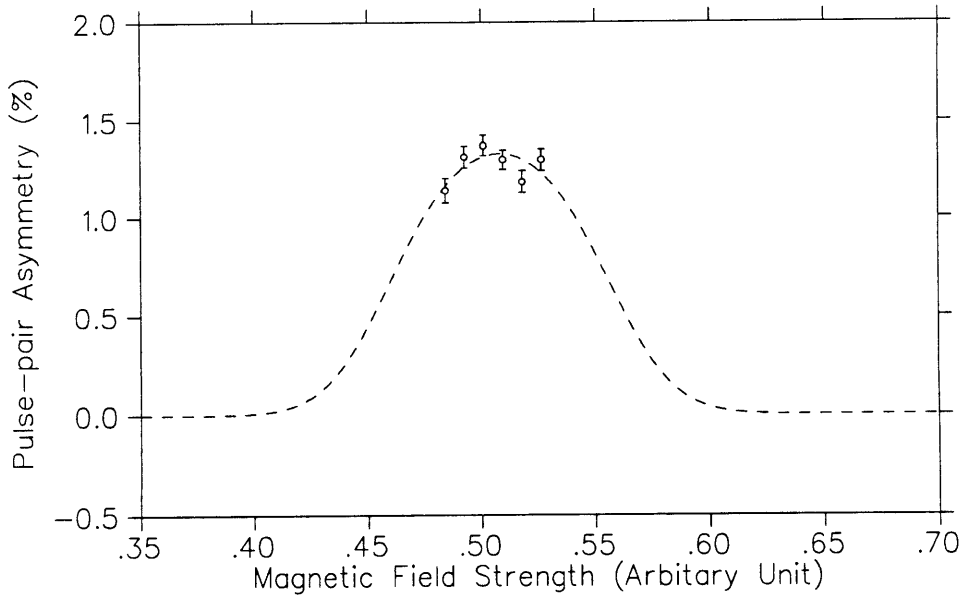

Figure 3-28: Normalized yield versus magnetic field strength for narrow scan.

Chapter 4

Results and Discussions

In this chapter, the final results of this experiment and discussions are presented in the following steps:

1. Present the procedure to transform the measured polarization components at the focal plane to those at the target.
2. Discuss the systematic uncertainties.
3. Compare the final results with theory.
4. Discuss the recoil proton polarization of the accidental coincidences.
5. Conclusions.

4.1 Spin Precession Transformation

The recoil protons from the primary scattering in the deuteron target traverse the OHIPS to its focal plane where the recoil proton polarization is measured. As these protons travel through the spectrometer magnetic elements, the spin of protons precesses with respect to their momentum. To determine the polarization at the target from measured proton polarization at the focal plane, the SPIN TRANSPORT of the OHIPS must be understood.

4.1.1 SPIN TRANSPORT matrix

The three component polarization vector at the focal plane, $\vec{P}^{fp}$, is related to the polarization vector at the target, $\vec{P}^{tgt}$, by

$$\vec{P}^{fp} = \overline{\overline{U}}\vec{P}^{tgt} , \tag{4.1}$$

where $\overline{\overline{U}}$ is a unitary matrix of rank 3 representing the SPIN TRANSPORT matrix. $\overline{\overline{U}}$ depends on the initial coordinate of the proton $\vec{X} = (X, \theta, Y, \phi, \delta)$ and can be represented by

$$U(\vec{X})_{ij} = U^{[1]}_{ij} + \sum_k U^{[2]}_{ijk} X_k , \tag{4.2}$$

where the $U^{[1]}_{ij}(U^{[2]}_{ijk})$ is a first (second) order matrix element.

If recoil protons traverse several magnetic elements, the SPIN TRANSPORT matrix, $\overline{\overline{U}}$, can be replaced by the product of the individual matrices of the magnetic elements

$$\overline{\overline{U}}(\vec{X}_1) = \overline{\overline{U}}_N(\vec{X_N})...\overline{\overline{U}}_2(\vec{X}_2)\overline{\overline{U}}_1(\vec{X}_1) , \tag{4.3}$$

where $\vec{X}_i$ is the initial coordinate of the proton for *i-th* magnetic element.

Since the OHIPS is a quadrupole-quadrupole-dipole (QQD) spectrometer, Equation 4.3 becomes

$$\vec{P}^{fp} = \overline{\overline{D}}\ \overline{\overline{Q}}_H\overline{\overline{Q}}_V\vec{P}^{tgt} , \tag{4.4}$$

where $\overline{\overline{D}}$ and $\overline{\overline{Q}}_H$ $(\overline{\overline{Q}}_V)$ are the SPIN TRANSPORT matrices of dipole and horizontal (vertical) focusing quadrupole, respectively.

4.1.2 Spin Precession in Dipole

Spin precession due to the magnetic fields is governed by the Thomas equation. [58] In the absence of an electric field, the Thomas equation becomes:

$$\frac{d\vec{s}}{dt} = \frac{e}{mc}\vec{s} \times \left[\left(\frac{1}{\gamma} + \frac{g-2}{2}\right)\vec{B} - \left(\frac{g-2}{2}\right)\left(\frac{\gamma}{\gamma+1}\right)\left(\vec{\beta}\cdot\vec{B}\right)\vec{B}\right] , \tag{4.5}$$

where g is the proton gyromagnetic ratio, β is the velocity of the proton, γ is the Lorentz factor, and $\vec{B}$ is the magnetic field. Equation 4.5 can be written in the form of Nurushev [59]:

$$\begin{aligned} \frac{d\vec{s}}{dt} &= \frac{e}{\gamma mc}\vec{s}\times\left[\frac{g}{2}\vec{B}_L+\left(\frac{1}{\gamma}+\frac{g-2}{2}\right)\vec{B}_T\right] , \\ &= \frac{e}{pc}\vec{s}\times\vec{A} , \end{aligned} \tag{4.6}$$

where $\vec{B}_L$ and $\vec{B}_T$ are the components of the magnetic field parallel and perpendicular to the velocity of the proton and p is a momentum of the proton. Assuming that the proton moves along $\hat{z}$ with a constant velocity, the yz plane is horizontal and the xz plane is vertical, a matrix equation can be written

$$\frac{ds_i}{dz} = \frac{e}{pc}\epsilon_{ijk}s_jA_k . \tag{4.7}$$

For the field of a dipole where $\vec{B}_L = 0$ and $\vec{B}_T = B_0\hat{x}$, the equation of motion for a proton is

$$\frac{d^2x}{dz^2} + \Theta^2 z = 0 , \tag{4.8}$$

where $\Theta = (1+\gamma\frac{g-2}{2})\Omega$ and $\Omega = (eB_0/pc)$. Θ is a sum of the bend angle, Ω and the dipole precession angle, χ. Thus the SPIN TRANSPORT matrix for dipole can be written

$$\overline{\overline{D}} = \begin{pmatrix} \cos\Theta & 0 & -\sin\Theta \\ 0 & 1 & 0 \\ \sin\Theta & 0 & \cos\Theta \end{pmatrix} . \tag{4.9}$$

4.1.3 Spin Precession in Quadrupole

Assuming the fields in a quadrupole can be modeled as $\vec{B}_L = 0$ and $\vec{B}_T = G_0 y\hat{x} + G_0 x\hat{y}$ for horizontal focusing(in the xz plane), the equation of motion for a proton is:

$$\begin{pmatrix} \frac{d^2x}{dz^2} \\ \frac{d^2y}{dz^2} \end{pmatrix} = \kappa^2 \begin{pmatrix} -x \\ y \end{pmatrix} , \tag{4.10}$$

where $\kappa = eG/pc$. Given initial conditions, the solution of Equation 4.10 can be determined:

$$\begin{pmatrix} x \\ \theta \end{pmatrix} = \begin{pmatrix} \cos\kappa z & \kappa^{-1}\sin\kappa z \\ -\kappa\sin\kappa z & \cos\kappa z \end{pmatrix} \begin{pmatrix} x_0 \\ \theta_0 \end{pmatrix} , \tag{4.11}$$

$$\begin{pmatrix} y \\ \phi \end{pmatrix} = \begin{pmatrix} \cosh\kappa z & \kappa^{-1}\sinh\kappa z \\ \kappa\sinh\kappa z & \cosh\kappa z \end{pmatrix} \begin{pmatrix} y_0 \\ \phi_0 \end{pmatrix} , \tag{4.12}$$

where x_0, θ_0, y_0 and ϕ_0 are initial coordinates of a proton. For vertical focusing (in the yz plane), the equation of motion for a proton becomes:

$$\begin{pmatrix} \frac{d^2x}{dz^2} \\ \frac{d^2y}{dz^2} \end{pmatrix} = \kappa^2 \begin{pmatrix} x \\ -y \end{pmatrix} . \tag{4.13}$$

Integrating Equation 4.7 for given initial coordinates gives :

$$\begin{aligned} s_x(z) &= s_x(0) - \lambda \int_0^z s_z(\zeta)x(\zeta)d\zeta , \\ s_y(z) &= s_y(0) + \lambda \int_0^z s_z(\zeta)y(\zeta)d\zeta , \\ s_z(z) &= s_z(0) + \lambda \int_0^z \left(s_x(\zeta)x(\zeta) - s_y(\zeta)y(\zeta)\right)d\zeta , \end{aligned} \tag{4.14}$$

where $\lambda = \alpha\kappa^2$ and $\alpha = 1+\gamma\frac{g-2}{2}$. Solving these equations and taking the above equations of motion into account, the matrix $\overline{\overline{Q}}_H$ for the spin transport through quadrupole fields for horizontal focusing can be determined. Each matrix elements of $\overline{\overline{Q}}_H$ is approximated

up to second order in λ:

$$\begin{aligned}
Q_{11} &\approx 1+\frac{1}{2}\alpha^2(x^2-\theta_0^2)+\alpha^2\theta_0(x-\theta_0)\\
Q_{12} &\approx \frac{1}{2}\alpha^2(xy-x_0y_0)-\frac{1}{2}\alpha^2(\theta\phi-\theta_0\phi_0)+\alpha^2\phi_0(\theta-\theta_0)\\
Q_{13} &\approx \alpha(\theta-\theta_0)\\
Q_{21} &\approx -\frac{1}{2}\alpha^2\kappa^2(xy-x_0y_0)-\frac{1}{2}\alpha^2(\theta\phi-\theta_0\phi_0)+\alpha^2\theta_0(\phi-\phi_0)\\
Q_{22} &\approx 1-\frac{1}{2}\alpha^2\kappa^2(y^2-y_0^2)+\alpha^2\phi_0(\phi-\phi_0)\\
Q_{23} &\approx \alpha(\phi-\phi_0)\\
Q_{31} &\approx -\alpha(\theta-\theta_0)\\
Q_{32} &\approx -\alpha(\phi-\phi_0)\\
Q_{33} &\approx 1-\frac{1}{2}\alpha^2((\theta-\theta_0)^2+(\phi-\phi_0)^2)\ . \qquad (4.15)
\end{aligned}$$

The matrix $\overline{\overline{Q}}_V$ for vertical focusing can be calculated in the same way as the matrix $\overline{\overline{Q}}_H$ for horizontal focusing.

4.1.4 Extraction of Polarization at the Target

The polarization measurements are statistical which means that the polarization at the focal plane is the event-averaged polarization for many events. Also can be determined only event-averaged focal plane polarization components perpendicular to the event-averaged proton momentum at the focal plane. Thus Equation 4.1 can be written

$$\left\langle \vec{P}^{fp} \right\rangle = \left\langle \mathbf{P}\overline{\overline{U}}\vec{P}^{tgt} \right\rangle\ , \qquad (4.16)$$

where $\vec{P}^{fp} = \left(P_x^{fp}, P_y^{fp}\right)$, $\overline{\overline{U}}$ is the SPIN TRANSPORT matrix and $\mathbf{P}$ is a 2×3 projection matrix given by

$$\mathbf{P} = \begin{pmatrix} 1 & 0 & 0 \\ 0 & 1 & 0 \end{pmatrix}\ . \qquad (4.17)$$

On the other hand, $\vec{P}^{fp}$ is measured independently for opposite electron helicities, $\vec{P}^{fp,+}$ and $\vec{P}^{fp,-}$. The sum and difference of $\vec{P}^{fp,+}$ and $\vec{P}^{fp,-}$ can be written

$$\left\langle \vec{P}^{fp,+} \pm \vec{P}^{fp,-} \right\rangle = \left\langle \mathbf{P}\overline{\overline{U}}[\vec{P}^{tgt,+} \pm \vec{P}^{tgt,-}] \right\rangle . \tag{4.18}$$

Since $\vec{P}^{fp,+}$ is related to $\vec{P}^{fp,-}$ by $\vec{P}^{tgt,+} = \mathbf{R}\vec{P}^{tgt,-}$ where $\mathbf{R}$ is a 3×3 reflection matrix defined by

$$\mathbf{R} = \begin{pmatrix} 1 & 0 & 0 \\ 0 & -1 & 0 \\ 0 & 0 & -1 \end{pmatrix} . \tag{4.19}$$

Equation 4.18 becomes

$$\left\langle \vec{P}^{fp,+} \pm \vec{P}^{fp,-} \right\rangle = \left\langle \mathbf{P}\overline{\overline{U}}[\mathbf{I} \pm \mathbf{R}]\vec{P}^{tgt,+} \right\rangle . \tag{4.20}$$

In general, $\left\langle \overline{\overline{U}}\vec{P}^{tgt} \right\rangle \neq \left\langle \overline{\overline{U}} \right\rangle \left\langle \vec{P}^{tgt} \right\rangle$, but for a small acceptance, Equation 4.20 can be approximated by

$$\left\langle \vec{P}^{fp,+} \pm \vec{P}^{fp,-} \right\rangle \approx \left\langle \mathbf{P}\overline{\overline{U}}[\mathbf{I} \pm \mathbf{R}] \right\rangle \left\langle \vec{P}^{tgt,+} \right\rangle . \tag{4.21}$$

There are four observed quantities at the focal plane: $\langle P_x^{fp,\pm} \rangle$ and $\langle P_y^{fp,\pm} \rangle$. The sums, Σ_i's and difference, Δ_i's of these quantities can be written:

$$\begin{aligned} \Sigma_x &= \langle P_x^{fp,+} + P_x^{fp,-} \rangle & \Delta_x &= \langle P_x^{fp,+} - P_x^{fp,-} \rangle \\ \Sigma_y &= \langle P_y^{fp,+} + P_y^{fp,-} \rangle & \Delta_y &= \langle P_y^{fp,+} - P_y^{fp,-} \rangle . \end{aligned} \tag{4.22}$$

If these new variables are arranged in a 4×1 column vector and represented as a product of a 4×3 matrix Λ and a 3×1 column vector $\vec{P}^{tgt}$, the following matrix equation is obtained,

$$\begin{pmatrix} \Sigma_x \\ \Delta_x \\ \Sigma_y \\ \Delta_y \end{pmatrix} = \begin{pmatrix} \left\langle \mathbf{P}\overline{\overline{U}}[\mathbf{I}+\mathbf{R}] \right\rangle \\ \left\langle \mathbf{P}\overline{\overline{U}}[\mathbf{I}-\mathbf{R}] \right\rangle \end{pmatrix} \begin{pmatrix} \langle P_n^{tgt} \rangle \\ \langle P_t^{tgt} \rangle \\ \langle P_l^{tgt} \rangle \end{pmatrix} = \mathbf{\Lambda} \begin{pmatrix} \langle P_n^{tgt} \rangle \\ \langle P_t^{tgt} \rangle \\ \langle P_l^{tgt} \rangle \end{pmatrix} , \tag{4.23}$$

The target polarizations can be determined by calculating the pseudo-inverse of $\mathbf{\Lambda}$:

$$\begin{pmatrix} \langle P_n^{tgt} \rangle \\ \langle P_t^{tgt} \rangle \\ \langle P_l^{tgt} \rangle \end{pmatrix} = \left(\mathbf{\Lambda}^T \mathbf{\Lambda}\right)^{-1} \mathbf{\Lambda}^T \begin{pmatrix} \Sigma_x \\ \Delta_x \\ \Sigma_y \\ \Delta_y \end{pmatrix} . \tag{4.24}$$

If all magnetic elements in the spectrometer and the central trajectory are perfectly aligned with the ideal optical axis, the quad field vanishes and only the effect of the dipole fields contributes. The expression of the proton polarization at the target for a 90° bending dipole, can be written,

$$\langle P_n^{tgt} \rangle = \frac{\langle +P_x^{fp,+} + P_x^{fp,-} \rangle}{2\cos\chi} , \tag{4.25}$$

$$\langle P_t^{tgt} \rangle = \frac{\langle +P_y^{fp,+} - P_y^{fp,-} \rangle}{2} , \tag{4.26}$$

$$\langle P_l^{tgt} \rangle = \frac{\langle -P_x^{fp,+} + P_x^{fp,-} \rangle}{2\sin\chi} . \tag{4.27}$$

'SPORT [64] is used to model the spin precession of the proton in the OHIPS. It determines the total SPIN TRANSPORT matrix $\overline{\overline{U}}$ by computing, for each event, the trajectory of the charged particle, the individual matrices $\overline{\overline{U}}_1$,$\overline{\overline{U}}_2$,...$\overline{\overline{U}}_N$ for each magnetic element and the product of the individual matrices. It calculates up to the second order of SPIN TRANSPORT matrix, $\overline{\overline{U}}^{[1]}$ and $\overline{\overline{U}}^{[2]}$. Then it calculates $\left\langle \overline{\overline{U}} \right\rangle$, the average of $\overline{\overline{U}}$ for the events over the acceptance and determines the polarization at the target by solving Equation 4.24. MCEEP [61] is used to model the distribution of events over the acceptance of the OHIPS. MCEEP generates events uniformly across the acceptance and assigns as a weight the cross section for those events. The PWIA model with relativistic corrections of Van Orden [62] is utilized for the cross section.

4.2 Systematic Uncertainties

In this section, the sources of systematic uncertainties and how theses uncertainties affect the data analysis and the final results, are discussed.

The systematic uncertainties for this experiment are associated with the following sources:

1. Acceptances and kinematics.
2. Recovery of the polarization at the target from the measured polarization at the focal plane.
3. Analyzing power.
4. Electron beam polarization.

4.2.1 Acceptances and kinematics

The sensitivity of the measured polarization to acceptances and kinematics is examined by varying input parameters in the MCEEP. The MCEEP has been modified to read a set of files which have a complete set of 18 response functions and cross section with respect to electron beam energy ε, the energy of the scattered electron ε', the scattering angle θ_e and the opening angle θ_{pq}. Since the electron beam energy was very stable during this experiment, the value is fixed at 579.5 MeV for this study. The other variables, ε', θ_e and θ_{pq} are used to form grids to extract the individual response functions and cross section by using a spline fitting interpolation routine. [63]

The changes in three components of the polarization are examined by varying individually each parameter by an uncertainty (labelled δ) and comparing to the polarization for nominal input parameters. The angular ranges are varied by 5 % for OHIPS and 10 % for MEPS. Since the uncertainty in the MEPS solid angle is larger, the larger variation is examined in the MEPS angles. The central angles of the acceptance are varied by a 4.0 mrad shift for MEPS and a 2.0 mrad shift for OHIPS. The central momentum of both spectrometers are varied by $\pm 0.3\%$ for MEPS and $\pm 0.25\%$ for OHIPS. In Table 4.1, the systematic uncertainties from acceptances and kinematics are listed for these variations.

	$\Delta\langle P_t^{tgt}\rangle/\langle P_t^{tgt}\rangle$	$\Delta\langle P_l^{tgt}\rangle/\langle P_l^{tgt}\rangle$	$\Delta\langle P_n^{tgt}\rangle/\langle P_n\rangle^{tgt}$
MEPS			
$\delta(\phi_0)$ = 4 mrad	0.75%	0.63%	0.80%
$\delta(\theta_0)$ = 4 mrad	0.04%	0.03%	0.02%
$\delta(\Delta\phi)$ = 13 mrad	0.07%	0.13%	0.04%
$\delta(\Delta\theta)$ = 11 mrad	0.08%	0.09%	0.56%
$\delta(p_0)$ = 0.93 MeV/c	0.87%	1.05%	1.05%
OHIPS			
$\delta(\phi_0)$ = 1.3 mrad	0.24%	0.57%	0.36%
$\delta(\theta_0)$ = 1.3 mrad	0.32%	0.23%	0.31%
$\delta(\Delta\phi)$ = 5.5 mrad	0.12%	0.26%	0.08%
$\delta(\Delta\theta)$ = 2.3 mrad	0.10%	0.73%	0.16%
$\delta(p_0)$ = 1.7 MeV/c	0.92%	0.90%	1.60%

Total Uncertainty	1.54%	1.82%	2.21%

Table 4.1: The first table lists the uncertainties in the polarization components due to uncertainties in the acceptance and kinematics. The second table lists the contributions to the total systematic uncertainty.

4.2.2 Analyzing Power

Since the polarization components at the target are linear in terms of those at the focal plane, the relative uncertainties in $\langle P_n^{tgt} \rangle$, $\langle P_t^{tgt} \rangle$ and $\langle P_l^{tgt} \rangle$ due to the uncertainty in the analyzing power is determined by fitting errors of analyzing power such that

$$\frac{\Delta \langle P_i^{tgt} \rangle}{\langle P_i^{tgt} \rangle} = \frac{\Delta \langle A_y \rangle}{\langle A_y \rangle} = 1.5\% \quad ; i = n, t, l \ . \tag{4.28}$$

The fitting errors of analyzing power have been discussed in Chapter 3 and more details can be found in other Reference. [28].

4.2.3 Recovery of the polarization at the target

As discussed in the previous section, a model of the spectrometer optics is required to determine the SPIN TRANSPORT matrix. This model depends on kinematic quantities. 'SPORT [64] is used to address sensitivity of the model to the kinematic quantities by varying individually each parameter and comparing to the polarization for nominal input parameters. There are four parameters used in this study:

1. the vertical beam position displacement (d_v) at the target with respect to the axis of the quadrupoles.
2. the horizontal beam position displacement (d_h) at the target with respect to the axis of the quadrupoles.
3. the OHIPS central momentum (p_c).
4. the transport angle θ_0^{fp} corresponding to the proton momentum $p = p_c$ and target angles $\theta_0^{tgt} = \phi_0^{tgt} = 0$.

In Table 4.2, the systematic uncertainties due to recovery of the polarization at the target are listed.

	$\Delta\langle P_t^{tgt}\rangle/\langle P_t^{tgt}\rangle$	$\Delta\langle P_l^{tgt}\rangle/\langle P_l^{tgt}\rangle$	$\Delta\langle P_n^{tgt}\rangle/\langle P_n\rangle^{tgt}$
$\delta(d_v) = 1.50$ mm	0.25%	2.40%	9.28%
$\delta(d_h) = 1.50$ mm	1.50%	0.81%	-
$\delta(p_c) = 0.50$ MeV/c	-	0.69%	-
$\delta(\theta_0^{fp}) = 3.00$ mrad	-	1.30%	-

Total Uncertainty	1.52%	2.93%	9.28%

Table 4.2: The first table lists the uncertainties in the polarization components due to uncertainties in recovery of the polarization at the target. Negligible variations are indicated by a dash. The second table lists the contributions to the total systematic uncertainty.

4.2.4 The electron beam polarization

The most significant systematic error source for electron beam polarization measurement is beam position instability. Fluctuations in the beam position change the scattering angle measured. The x position has the largest effect. An x beam position that is not centered also produce differences between the two detectors. A shift in the y and z directions also affects the measurements, but very little. The estimated systematic error from beam fluctuations is 2.5%.

The signal to background ratio uncertainty is the second most significant component of the error in the polarization measurement. Since the form of the background underneath the signal cannot be directly ascertained, the form of the background is taken to be an extrapolation of that where the signal is not present. To estimate the systematic variation in the signal to background ratio caused by the choice of a background function, the yield curve is fitted with several different background functions. The variation in the signal to background ratio with different background fitting functions is taken as an estimate of the systematic error. Another possible source of uncertainty in the signal to background ratio is any change in the background between the wide scan and the narrow scan. Since the background fit from the wide scan is used to fit a asymmetry of the narrow scan, a change in the background would alter the measurement. The combination of these sources for uncertainty in the signal to background ratio leads to a 1.8% error in the polarization.

Description	$\Delta P_e/P_e$
Beam position fluctuation	2.5%
Signal to background ratio uncertainty	1.8 %
Target polarization uncertainty	1.3%
Target angle uncertainty	1.5%
Systematic diff. between 2 detectors	1.5%
Helicity correlated uncertainty	0.2%
Electron Fermi-motion at atomic shells	0.3%
Total systematic error	4.0%

Table 4.3: Sytematic uncertainties in electron beam polarization.

There is a systematic difference between the measurements of the two Čerenkov detectors. The two Čerenkov detectors make separate independent measurements of the beam polarization. The signal characteristics of the two detectors should have a negligible effect because the asymmetry is being measured, not any absolute signal. The error source is not well understood. The estimated systematic error is 1.5%.

The target polarization uncertainty contributes 1.3% error to the final polarization. This uncertainty mainly comes from the separate measurement of the target polarization before the experiment. Another possible source of error is a change in the target polarization caused by the electron beam. Discussed in Arrington, et al. [27] is the effect of the beam lowering target polarization by heating the target. Misalignment of the target angle leads to an additional uncertainty in the fraction of target polarization in the z direction. This uncertainty in target angle introduces 1.5% error to the final polarization.

There are several other sources of error that have little contribution to the measured polarization or its error. One contribution is the beam position shift and the beam charge variation that are correlated with the helicity of the beam. Another systematic correction is needed for the electron Fermi-motion at atomic shells [60], but it is believed to be negligible for the measurement of the single-arm integration mode. [65]

These above errors are listed in Table 4.3 and all errors are added in quadrature giving a total systematic error of 4.0%.

4.2.5 Summary of systematic uncertainties

The following is the list of the summary of systematic uncertainties with statistical uncertainty.

	$\Delta\langle P_t^{tgt}\rangle/\langle P_t^{tgt}\rangle$	$\Delta\langle P_l^{tgt}\rangle/\langle P_l^{tgt}\rangle$	$\Delta\langle P_n^{tgt}\rangle/\langle P_n^{tgt}\rangle$
Acceptances and Kinematics	1.54%	1.82%	2.21%
Analyzing Power	1.45%	1.45%	1.45%
Recovery of $\vec{P}^{tgt}$	1.52%	2.93%	9.28%
Electron Beam Polarization	4.00%	4.00%	0.00%
Total Systematic Uncertainty	4.82%	5.54%	9.62%

Statistical Uncertainty	4.12%	9.88%	50.3%

4.3 Results and Comparison with Theory

4.3.1 Numerical Results

Polarization and its statistical uncertainty at the focal plane

	$\langle P_y^{fp,+} \rangle$	$\langle P_y^{fp,-} \rangle$	$\langle P_x^{fp,+} \rangle$	$\langle P_x^{fp,-} \rangle$	$\Delta\langle P \rangle$	$\langle A_y \rangle$
Reals	-0.1795	$+0.1818$	$+0.0752$	-0.0813	± 0.0125	0.5616
Accidentals	-0.1313	$+0.12858$	$+0.1607$	-0.0497	± 0.0207	0.5628
Trues	-0.1852	$+0.1880$	$+0.0652$	-0.0966	± 0.0113	0.5617

Unnormalized Polarization at the target

	$h\langle P_t^{tgt} \rangle$	$h\langle P_l^{tgt} \rangle$	$\langle P_n^{tgt} \rangle$
Trues	-0.1887 ± 0.0078	$+0.2073 \pm 0.0204$	$+0.0171 \pm 0.0086$
Accidentals	-0.1314 ± 0.0205	$+0.1421 \pm 0.0375$	-0.114 ± 0.016

Polarization at the target normalized to measured beam helicity

	$\langle P_t^{tgt} \rangle$	$\langle P_l^{tgt} \rangle$	$\langle P_n^{tgt} \rangle$
Trues	-0.5337 ± 0.0220	$+0.5862 \pm 0.0579$	$+0.0171 \pm 0.0086$

4.3.2 Comparison with Theory

In this section, the measured $\left\langle \vec{P}^{tgt} \right\rangle$ is compared with the calculations of Arenhövel. To compare with theory, the measured $\left\langle \vec{P}^{tgt} \right\rangle$ need to be corrected for the effect of the

	$\langle P_t^{tgt} \rangle$	$\langle P_l^{tgt} \rangle$	$\langle P_n^{tgt} \rangle$
λ_{point}	1.011	0.992	-0.871
Corrected	$-0.5396 \pm 0.022 \pm 0.022$	$0.5815 \pm 0.056 \pm 0.031$	$-0.014 \pm 0.008 \pm 0.001$

Table 4.4: Corrected proton polarization and λ_{point}

measuring over a finite acceptance. This correction factor, λ_{point} can be defined as

$$\lambda_{point} = \frac{\left\langle \vec{P}^{tgt} \right\rangle \text{ for a point acceptance}}{\left\langle \vec{P}^{tgt} \right\rangle \text{ for experimental acceptance}} . \tag{4.29}$$

The MCEEP is used to include all response functions which contribute to $\left\langle \vec{P}^{tgt} \right\rangle$ measured over a finite acceptance. In Table 4.4, the corrected polarization at the target is listed and the λ_{point}'s for three components of polarization are also listed.

In Figure 4-1, a theoretical calculation by Arenhövel [74] with the measured $\left\langle \vec{P}^{tgt} \right\rangle$ is plotted as a function of the angle, θ_{pq} between the proton momentum and momentum transfer $\vec{q}$ in the laboratory frame. The three curves represent different reaction mechanisms:

1. PWBA+RC (Dotted line):
   PWBA with Relativistic Corrections.
2. Normal+RC (Dashed line):
   PWBA, Relativistic Corrections, and Final State Interactions.
3. Normal+RC+MEC+IC (Solid line):
   PWBA, Relativistic Corrections, ,Final State Interactions, Meson Exchange Currents and Isobar Configurations.

A brief overview of theoretical approach has been already discussed in Section 1.4. Presented in Figure 4-1, is the sensitivity of three components of the polarization to the inclusion of meson exchange currents and isobar configurations, and finally to the role of relativistic corrections at the kinematics of this experiment. The measured $\langle P_n^{tgt} \rangle$, $\langle P_t^{tgt} \rangle$ and $\langle P_l^{tgt} \rangle$ are represented by a solid square, an open circle and an open square,

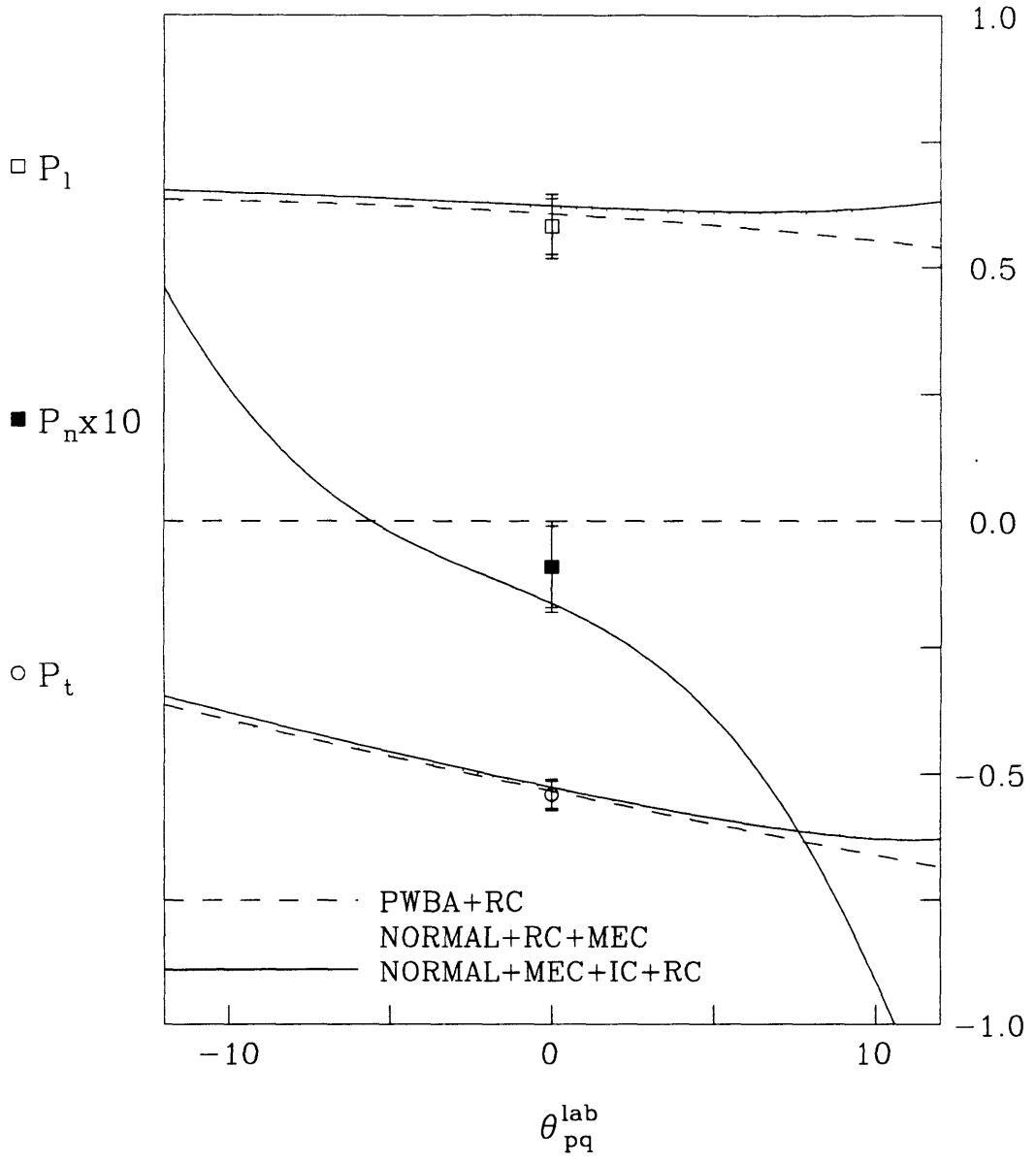

Figure 4-1: Comparison of calculations of Arenhövel for recoil proton polarization with measured results.

respectively. The data shown are corrected by the effect of finite acceptances. The inner error bars are statistical while the outer ones are statistical and systematic in quadrature. Note that, for the normal component, data, uncertainties, and theory have been magnified ten times.

4.4 Proton Polarization in Accidental Coincidences

Since large polarization, expecially the normal component of the polarization is measured in accidental coincidences, it is worthwhile to study possible reactions which contribute to the polarization in accidental coincidences. In this section, the following topics are discussed:

1. Reactions in the accidental coincidences.
2. Polarized photons from polarized electrons.
3. d($\vec{\gamma}$,$\vec{p}$)n.

4.4.1 Reations in the accidental coincidences

The reaction mechanisms contributing to the proton single arm (e,p) cross section includes:

1. virtual photon absorption by deuteron, d(γ,p)n.
2. virtual photon absorption for pion production from bound nucleon producing proton, d(γ,p)π^0n, or d(γ,p)π^-p.
3. quasifree nucleon knockout by electron scattering.

Virtual Photon Absorption

The angular distribution of the virtual photon spectrum by electron scattering is highly peaked at near 0°. When the reaction mechanism by electron scattering produces a

corresponding real photon absorption, the forward peaking approximation (FPA) can be used to write the (e,p) cross section as the product of the (γ,p) cross section and a factor corresponding to the virtual photon flux:

$$\frac{d^2\sigma}{d\Omega_p dE_p} = \frac{N_e(\omega)}{\omega} R \frac{d\sigma_\gamma}{d\Omega_p} , \tag{4.30}$$

where $N_e(\omega)$ is the virtual photon spectrum, R is a recoil factor and ω is the energy transfer in the FPA.

For d(γ,p)n channel, the cross section is taken from a phenomenological fit to deuteron photodisintegration data. [66] The virtual photon spectrum for two-body break-up is given in Reference [67].

For d(γ,p)nπ^0 and d(γ,p)pπ^-, the cross section is estimated using the SAID program [68]. The virtual photon spectrum is taken from Reference [69].

Quasifree nucleon knockout by electron scattering

The quasifree nucleon knockout by electron scattering cannot be approximated by virtual photon abortion theory since there exists no analogy of real photon mechanism. The expression for $\frac{d^5\sigma_{(e,e'p)}}{d\sigma_e d\sigma_p dE_p}$ is taken from Reference [70, 71] which used the one-photon-exchange approximation. The inclusive cross section is then obtained by the angular integration over the unobserved electron,

$$\frac{d^3\sigma_{(e,p)}}{d\sigma_p dE_p} = \int_0^\pi \sin\theta d\theta \int_0^{2\pi} d\phi \frac{d^5\sigma_{(ee'p)}}{d\sigma_e d\sigma_p dE_p} . \tag{4.31}$$

The EPC program [72] is used to estimate the cross section.

In Table 4.5, the summary of the reaction mechanisms and their relative contributions are listed. In Figure 4-2, the cross sections for each reaction mechanisms are plotted as a function of the recoil proton momentum.

Description	Relative Contribution (%)
$d(\gamma,p)n$	52 %
Quasifree Nucleon	32 %
$d(\gamma,p)n\pi^0$ and $d(\gamma,p)p\pi^-$	16 %

Table 4.5: Systematic errors relative to beam polarization.

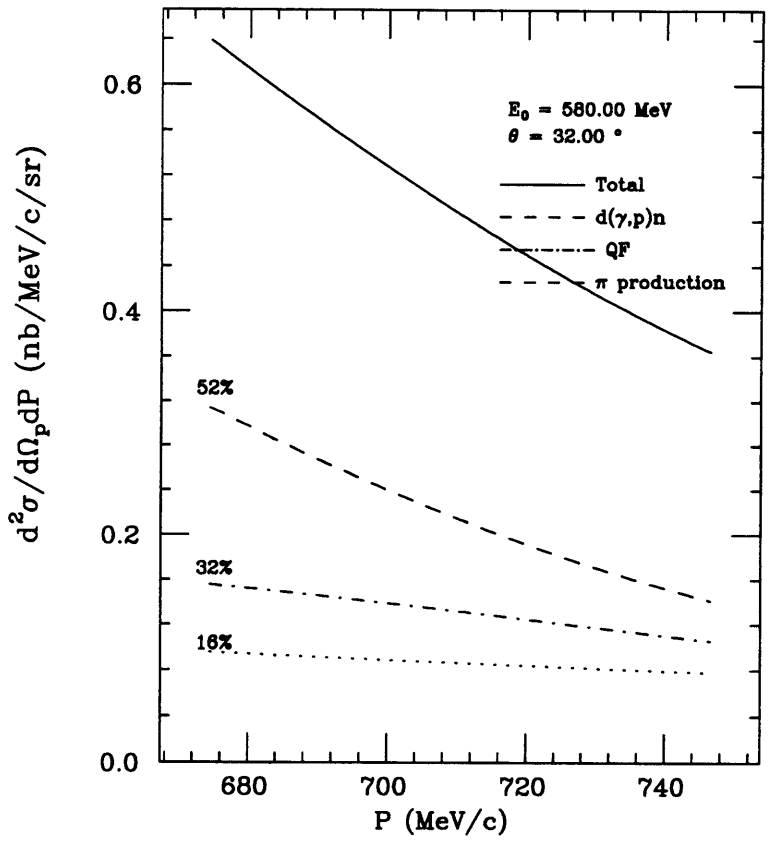

Figure 4-2: The proton single arm inclusive cross section with individual contributions from each reaction mechanism.

4.4.2 Polarized photons from polarized electrons

When longitudinally polarized electrons scatter off a target, circularly polarized photons are produced. When the polarization of electrons is transferred to the polarization of photon, the degree of the photon polarization, P_γ, is given by [73]

$$P_\gamma(f) = P_e \left[\frac{f(4-f)}{1-2f+3(1-f)^2} \right] \quad , \tag{4.32}$$

where f is the ratio of the photon energy (E_γ) to the incident electron energy (E_e) and P_e is the electron beam polarization. The ratio of photon circular polarization (P_γ) to electron beam polarization (P_e) is plotted as a function of f, the ratio of photon energy (E_γ) to incident electron beam energy (E_e) in Figure 4-3. At the endpoint, $f = 1$, the photon beam polarization is a maximum and $P_\gamma \approx P_e$ since in the limit where the photon takes all the electron momentum, it must conserve the helicity of the initial state.

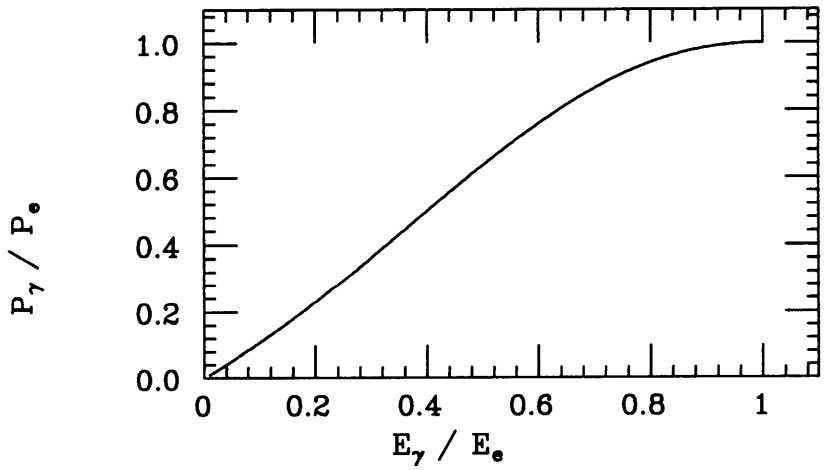

Figure 4-3: The ratio of photon circular polarization to electron beam polarization plotted as a function of f, the ratio of photon energy (E_γ) to incident electron beam energy (E_e).

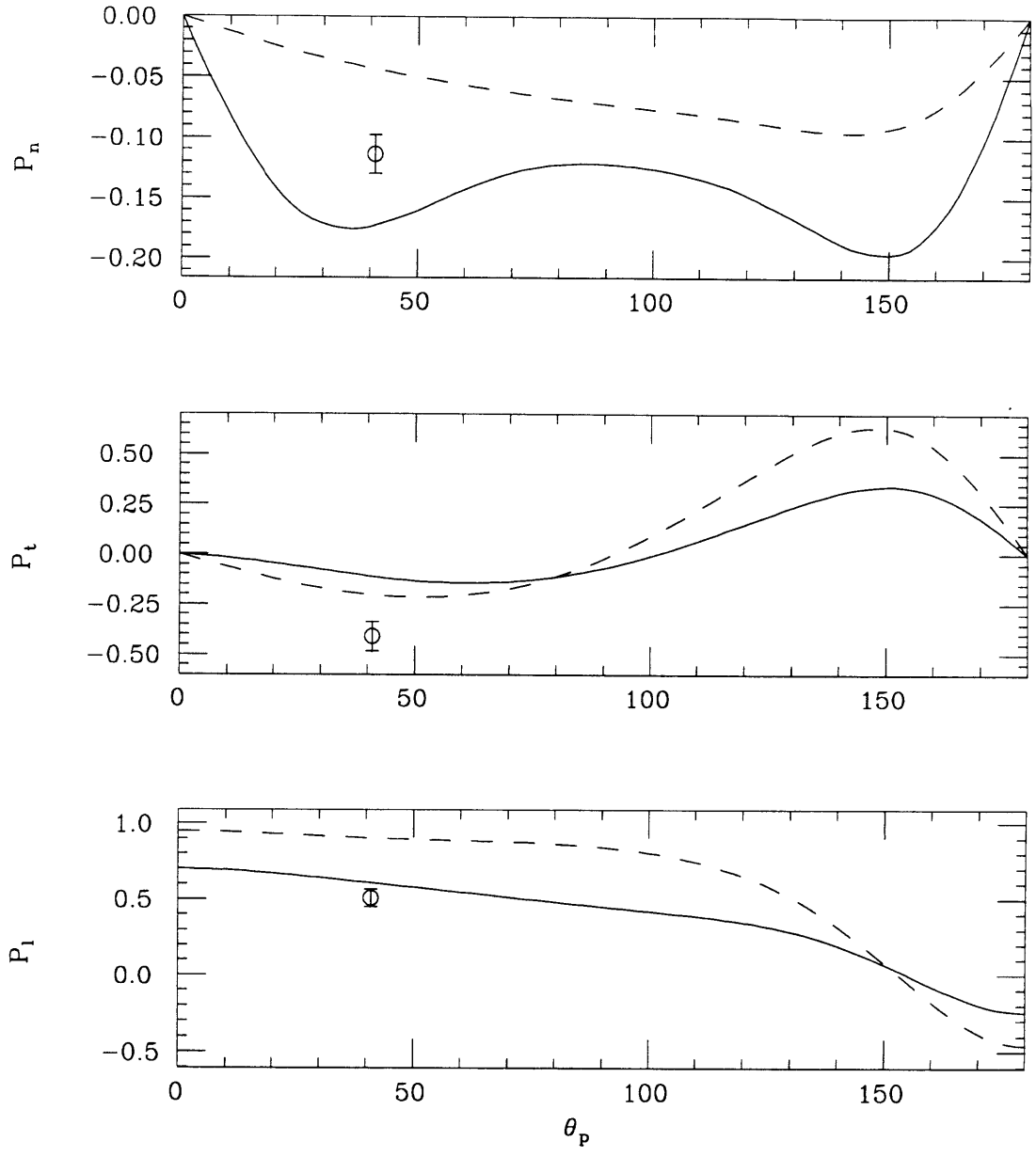

Figure 4-4: The calculations of Arenhövel for recoil proton polarization from d($\vec{\gamma}$,$\vec{p}$)n at E_γ = 347 MeV. θ_p is in the center of mass frame.

	$\langle P_t^{tgt} \rangle$	$\langle P_l^{tgt} \rangle$	$\langle P_n^{tgt} \rangle$
Unnormalized	-0.1314 ± 0.0205	$+0.1421 \pm 0.0375$	-0.114 ± 0.016
normalized	-0.4693 ± 0.0732	$+0.5075 \pm 0.0571$	-0.114 ± 0.016

Table 4.6: Polarization at the target normalized to measured beam helicity.

4.4.3 d($\vec{\gamma}$,$\vec{p}$)n

Since d($\vec{\gamma}$,$\vec{p}$)n is the most dominant reaction mechanism in the proton single arm inclusive cross section, let's assume that all accidental coincidences are from d($\vec{\gamma}$,$\vec{p}$)n. The differential cross section for d($\vec{\gamma}$,$\vec{p}$)n is given by

$$\begin{aligned} \frac{d\sigma}{d\Omega_\gamma} &= \frac{d\sigma_0}{d\Omega_\gamma}\{(R_T + \mathcal{S}_n R_T^n) + P_\gamma^l[(R_{TT} + \mathcal{S}_n R_{TT}^n)\cos 2\phi + \left(\mathcal{S}_l R_{TT}^l + \mathcal{S}_t R_{TT}^t\right)\sin 2\phi] \\ &\quad + P_\gamma^c\left(\mathcal{S}_l R_{TT'}^l + \mathcal{S}_t R_{TT'}^t\right)\} \ , \end{aligned} \tag{4.33}$$

where P_γ^l is the degree of linear polarization of real photon, ϕ is the angle of the polarization vector relative to the reaction plane, and P_γ^c is the degree of circular polarization of real photon. If real photon is completely linearly polarized with polarization vector normal to the reaction plane, $P_\gamma^l = 1$, $\phi = 0$, and $P_\gamma^c = 0$. On the other hand, if real photon is right (left) circularly polarized, then $P_\gamma^c = 1(-1)$ and $P_\gamma^l = 0$.

As discussed in the previous section, circularly polarized photons are created by polarized electrons. Futhermore, the helicity of circular polarization is controlled by the helicity of electrons. Therefore, proton polarization can be measured using the focal plane polarimeter (FPP) in the same way as in $(\vec{e}, e'\vec{p})$.

Since the scattering angle and momentum of the protons are measured by the spectrometer, the kinematics for d($\vec{\gamma}$,$\vec{p}$)n is well defined. For $\theta_p = 32.0°$ and the proton momentum, $p_p = 713$ MeV, the corresponding incident photon energy, E_γ, is 347 MeV. The degree of the circular polarization of the photons from 36 % polarized electrons is 27 % according to Equation 4.32. Listed in Table 4.4.3, are the proton polarization from the accidental coincidences unnormalized and normalized to circular polarization of the photons.

In Figure 4-4, theoretical calculations by Arenhövel [74] with the measured $\left\langle \vec{P}^{tgt} \right\rangle$ are plotted as a function of a proton angle, θ_p^{cm} in the center of mass of the final np state. The error bars are only statistical. Two curves of theoretical calculations represent two different models:

1. Impulse Approximation (IA) (Dotted Line).
2. Coupled Channel Approach (CC) (Dashed Line).

In IA, the NN wave functions, Φ_{NN}, are generated by using a realistic potential $\hat{V}_{NN}$ from

$$\left(\frac{\vec{p}^2}{2\mu_{NN}} + \hat{V}_{NN} - E_{NN} \right) \Phi_{NN} = 0 \ , \tag{4.34}$$

where μ_{NN} is the reduced mass of the NN system and $\hat{V}_{NN}$ contains implicitly the dispersive contributions of the isobar channels. In the other hand, in the CC approach, the equation for the NN wave functions is given by

$$\left(\frac{\vec{p}^2}{2\mu_{NN}} + V_{NN} - E_{NN} \right) \Phi_{NN} = - \sum_{N_1 N_2 \neq NN} V_{NN,N_1N_2} \Phi_{N_1N_2} \ , \tag{4.35}$$

where N_i enumerates the various intrinsic states of the nucleon ($N = N(939)$, $\Delta = \Delta(1232)...$) and the contributions of the isobar channels are not contained in V_{NN}. In the Impulse Approximation (IA), the NN wave function can be calculated for a given potential. Once the NN wave function is given, the isobar configurations are calculated. The disadvantage of this approach is that isobar degrees of freedom are only considered implicitly. The IA works well only in an energy region where the NN configurations is dominant. This is generally not the case in the Δ resonance region which is considered here.

Any conclusion can be hardly made by this analysis, but the large polarization in the accidental coincidences can be explained very well qualitatively, especially the exceptionally large normal component of the polarization compared with that of true coincidences.

4.5 Conclusions

The experiment described in this thesis focuses on measuring polarization observables from the deuteron electrodisintegration in the dip region using the focal plane polarimeter (FPP). This novel detection system which has been developed at M.I.T.-Bates measures the polarization of recoil protons scattered by polarized or unpolarized electrons.

The deuteron plays a special role in the investigation of the dynamics of the nuclear constituents in the nuclear medium; it is, in fact, the only bound two-nucleon system in nature. The interaction between two nucleons is commonly described by so-called realistic potentials. Once this has been fixed, calculations for electrodisintegration can be actually performed exactly, including final state interactions, meson exchange currents and isobar configurations.

Shown in Figure 4-5, are comparisons of the plane wave Born approximation (PWBA) of Arenhövel [74] to calculations with the different choice of reaction mechanism or potentials for all three components of the recoil proton polarization as a function of θ_{np}^{cm}. The difference between the calculation of PWBA and that of NORMAL indicates a possible sensitivity of the recoil proton polarization to final state interactions. On the other hand, the difference between the calculation of NORMAL and that of NORMA+MEC+IC indicates the effects of meson exchange currents and isobar configurations. Even though the dip region has long been recognized as having substantial strength from other mechanisms, the data show that the quasifree hypothesis is still valid in the parallel kinematics. To distinguish between various models, the kinematics must be chosen at very large proton scattering angle, hence high recoil momentum. Since the scattering cross section decreases rapidly with increasing recoil momentum, measurements there requires electron beam of high duty factor and high polarization. These requirements can be achieved in the near future at M.I.T.-Bates.

The study on the recoil proton polarization in accidental coincidences indicates the possible experiments measuring polarization observables from deuteron photodisintegration. The kinematics must be chosen to prevent the contamination from the pion productions. The recoil proton polarization technique is useful in testing the descriptions of impulse approximation and couple channel approach.

Finally, the experiment described in this thesis is the first of its kind and represents a good starting point to explore the details of reaction mechanisms for a large kinematic range.

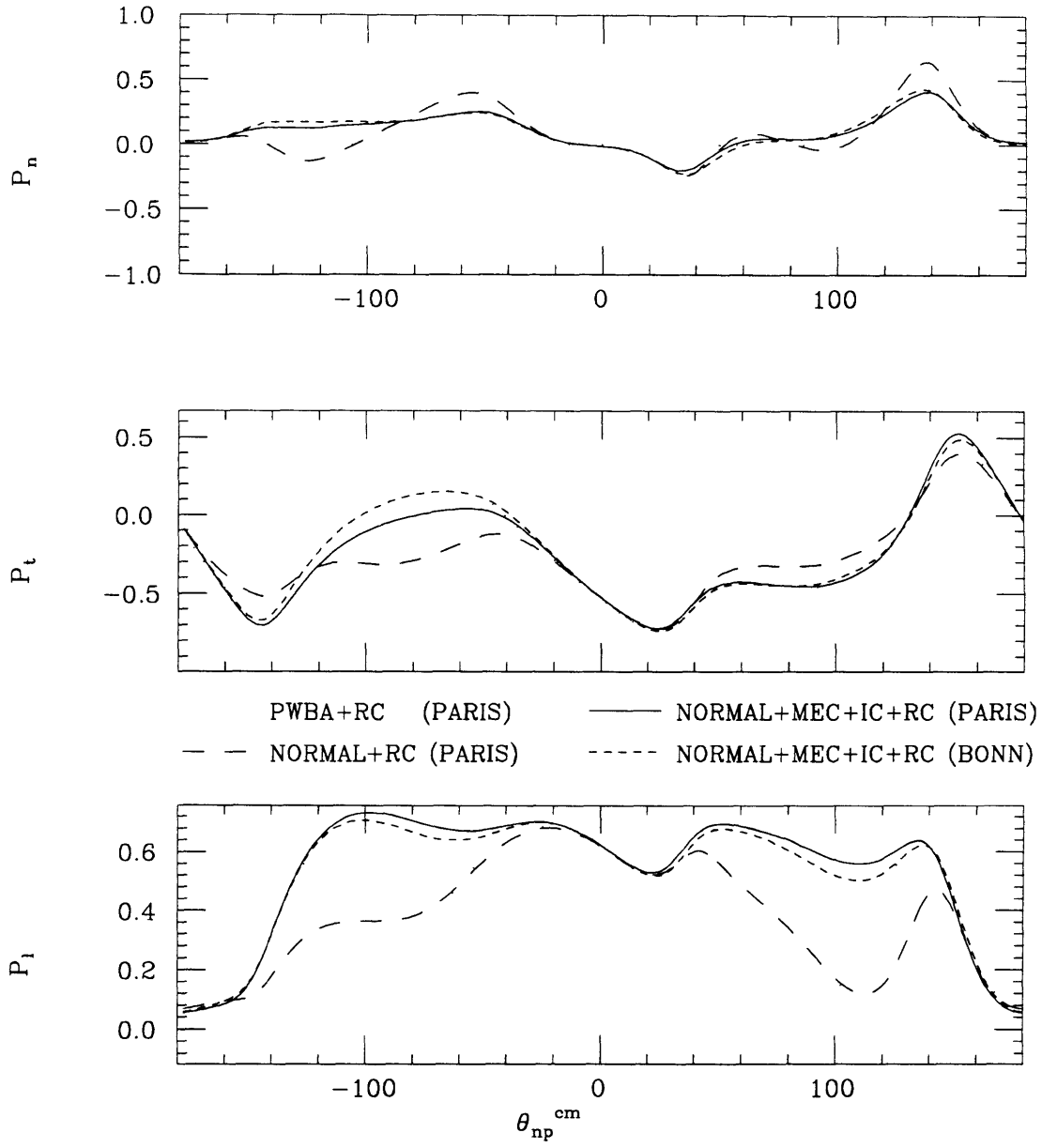

Figure 4-5: The calculations of Arenhövel for recoil proton polarization from $D(\vec{e}, e'\vec{p})$ at $\varepsilon_i = 580$ MeV, $\omega = 248$ MeV and $\theta_e = 80°$.

Appendix A

d(γ,p)n Kinematics

In this appendix, some formulae useful for d(γ,p)n kinematic calculations are presented. The photon strikes the deuteron target, mass m_d, which is at rest in the laboratory frame. The recoil proton, a mass m_p, is detected at angle θ_p with the undetected neutron, a mass m_n, at angle θ_n.

Given the rest masses m_d, m_p and m_n, and the angle, θ_p, total energy, E_p and momentum, p_p, the energy of the photon, E_γ is given by

$$E_\gamma = \frac{1}{2}\frac{m_d^2 + m_p^2 - m_n^2 - 2E_p m_d}{E_p - m_d - p_p \cos\theta_p} \; . \tag{A.1}$$

On the other hand, for a given photon energy, E_γ, the total energy of the recoil proton, E_p, is given by

$$E_p = \frac{E_T B \pm \sqrt{A(B^2 - 4m_p^2(E_T^2 - A^2)}}{2(E_T^2 - A^2)} \; , \tag{A.2}$$

where E_T is the total energy, $m_d + E_\gamma$, and $A = E_\gamma \cos\theta_p$ and $B = E_T^2 - E_\gamma^2 + m_p^2 - m_n^2$.

The energy, E_n, and angle, θ_n, of the undetected neutron are given by

$$E_n = E_T + m_d - E_p \; , \tag{A.3}$$

$$\tan\theta_n = \frac{\sin\theta_p}{\cos\theta_p - E_\gamma/p_p} \; . \tag{A.4}$$

Now let's consider the angle and solid angle transformations between the lab and center of mass frames. Let $\mathcal{B}$ and Γ represent the boost parameters between these two frames. $\mathcal{B}$ is the velocity of the deuteron in the center of mass frame, and is given by

$$\mathcal{B} = \frac{E_\gamma}{E_\gamma + m_d} \quad . \tag{A.5}$$

The angle of the detected proton in the center of mass frame, θ_p^{cm}, is given by

$$\tan\theta_p^{cm} = \frac{\sin\theta_p}{\Gamma(\cos\theta_p - \mathcal{B}/\beta)} \ , \tag{A.6}$$

where $\beta = p_p/E_p$. The solid angle Jacobian that converts a laboratory cross section $d\sigma/d\Omega$ to a center of mass cross section $d\sigma/d\Omega^{cm}$ is given by

$$\frac{d\Omega}{d\Omega^{cm}} = \Gamma^2\sqrt{C}(1 - r\cos\theta_p) \ , \tag{A.7}$$

where $C = 1 - \mathcal{B}^2 - 2r\cos\theta_p + r^2 + \mathcal{B}^2\cos^2\theta_p$, and $r = \mathcal{B}/\beta$.

Appendix B

Data File Structure

In this appendix, the raw data structures for event 8, event 4 and event 10 are listed in three tables, B.1, B.3 and B.5, respectively.

1	Event Type Bit Pattern
2	Trigger TDC Flag
3	OHIPS Pilot TDC
4	MEPS Pilot TDC
5	OHIPS Prescale TDC
6	MEPS Prescale TDC
7	COIN TDC
8	FPP Pass TDC
9	OHIPS Latch TDC #1
10	OFPS TDC

Table B.1: Event 8 Data Structure (continued on next page)

11	MEPS Latch TDC #1
12	MFPS TDC
13	Downstairs CTOF
14	OHIPS CAMAC Enable TDC
15	MEPS CAMAC Enable TDC
16	Upstairs CTOF
17	COIN Prescale TDC
18	Hardware Blank TDC
19-20	Beam Position Monitor
21	OHIPS Delay Line TDC Flag
22-31	OHIPS Scintillator ADCs
32-41	OHIPS Scintillator TDCs
42-46	OHIPS Meantimer TDCs
47	FS2OR TDC
48-63	OHIPS Delay Line TDC
64	MEPS Scintillator ADC Flag
65-70	MEPS Scintillator ADCs
71-80	MEPS Aerogel ADCs
81	MEPS Aerogel Sum ADC
82-87	MEPS Scintillator TDCs
88	MEPS S0OR TDC
89-90	MEPS Scintillator MT TDCs
91-100	MEPS Aerogel TDCs
101	MEPS Aerogel Sum TDC
102	MEPS DCOS Flag
103-127	MEPS DCOS Words
128	FPP TDC Flag
129-130	PCOS MLU Data Ready TDCs
131-136	PCOS Crate Data Ready TDCs
137	FPP PCOS Flag
138-183	PCOS Wire Chamber Words

Table B.2: Event 8 Data Structure (continued from previous page)

1-6	MEPS Scintillators
7	MEPS S0 OR
8	MEPS MS3 Meantimer
9	MEPS MS4 Meantimer
10	BT3
11	MPI Upstairs
12	Blank
13-22	MEPS Aerogel's
23	MEPS Aerogel Sum
24	Gun
25	Gun AND Computer Not Busy
26	Gun AND Computer Not Busy AND Helicity Plus
27	Gun AND Computer Not Busy AND Helicity Minus
28	Gun
29	Gun AND Computer Not Busy
30-39	OHIPS Scintillators
40-44	OHIPS Meantimers
45	FS2OR
46	COIN
47	COIN Prescale
48	OHIPS Prescale
49	OHIPS Latch
50	COIN Prescale
51	MEPS Prescale
52	MEPS Latch
53	MEPS Pilot
54	MEPS DCOS Stop
55	OHIPS PCOS Start (E1)
56	COIN and Helicity Plus
57	COIN and Helicity Minus
58	1/burst COIN and Helicity Plus
59	1/burst COIN and Helicity Minus
60	Hardware Blank
61	OHIPS Pilot
62	1/burst COIN
63	FPP Pass
64	FPP Pass
65	1/burst COIN Prescaler

Table B.3: Event 4 Data Structure (continued on next page).

66	1/burst OHIPS Prescaler
67	1/burst FPP Pass
68	1/burst COIN Prescaler
69	1/burst MEPS Prescaler
70	1/burst OHIPS Latch
71	1/burst MEPS Latch
72	1/burst OHIPS Latch #2
73	1/burst OHIPS CAMAC Enable
74	1/burst MEPS CAMAC Enable
75	1/burst MEPS Latch #2
76	1/burst OFPS
77	1/burst MFPS
78-93	OHIPS Delay Lines
94	Prompt 8
95	COIN Event
96-101	PCOS Crate Data Readies
102-103	PCOS MLU Data Readies
105	PCOS Small Angle Pass
106	OHIPS Reset
107	MEPS Reset
108	OHIPS Pilot τ
109	OHIPS Pilot 2τ
110	MEPS Pilot τ
111	MEPS Pilot 2τ
112	COIN Pilot τ
113	COIN Pilot 2τ

Table B.4: Event 4 Data Structure (continued from previous page).

0	ADC Flag
1	Helicity Word
2	Timeslot Scaler
3	BT1 ADC
4	BT2 ADC
5	MøllerX BPM ADC
6	MøllerY BPM ADC
7	Target X BPM ADC
8	Target Y BPM ADC
9	MøllerHalo ADC
10	Target ADC
11-14	Raw Coincidence TDC

Table B.5: Event 10 Data Structure.

Bibliography

[1] T. de Forest Jr. and J. D. Walecka, *Adv. Phys.*, **15**, 1 (1966).

[2] J. D. Bjorken and S. D. Drell. *Relativistic Quantum Mechanics.* McGraw-Hill,Inc., New York, 1964.

[3] A. S. Raskin and T. W. Donnelly *Ann. Phys.*, **191**, 78 (1989).

[4] A. Picklesimer and J. W. Van Orden *Phys. Rev. C*, **35**, 266 (1987).

[5] W. Fabian and H. Arenhövel *Nucl. Phys.*, **A314**, 253 (1979).

[6] H. Arenhövel *Nucl. Phys.*, **A384**, 287 (1982).

[7] H. Arenhövel, W Leidemann and E. L. Tomusiak *Z. Phys.*, **A331**, 123 (1988).

[8] H. Arenhövel, W Leidemann and E. L. Tomusiak *Phys. Rev. C*, **46**, 455 (1992).

[9] G. Beck and H. Arenhövel *Few-body Systems*, **13**, 165 (1992).

[10] M. Lacombe et al. *Phys. Rev. C*, **21**, 861 (1980).

[11] R. Machleidt, K. Holinde, and C. Elster *Physics Reports*, **149**, 1 (1987).

[12] H. J. Weber and H. Arenhövel *Physics Reports*, **36**, 277 (1978).

[13] H. G. Miller, Universität Frankfurt, Habilitationsschrift, unpublished (1974).

[14] W. Fabian, Universität Mainz, Doctoral Thesis, unpublished (1975).

[15] P. Wilhelm, W. Leidemann and H. Arenhövel *Few-body Systems*, **3**, 111 (1988).

[16] T. Wilbois, G. Beck and H. Arenhövel *Few-body Systems*, **15**, 39 (1993).

[17] B. D. Milbrath, University of Virginia, Ph.D. Thesis, unpublished (1996).

[18] J. I. McIntyre, College of William and Mary, Ph.D. Thesis, unpublished (1996).

[19] D. H. Barkhuff, University of Virginia, Ph.D. Thesis, unpublished (1997).

[20] P. Barreau et al. *Nuclear Physics* **A402**, 515 (1983).

[21] J. W. Van Orden and T. W. Donnelly *Ann. Phys.*, **131**, 145 (1980).

[22] T. W. Donnelly, J. W. Van Orden, T. deForest Jr. and W. C. Herman *Phys. Lett.*, **76B**, 393 (1978).

[23] R. W. Lourie et al. *Phys. Rev. Lett.*, **56**, 2364 (1986).

[24] R. D. Ransome et al. *Nucl. Inst. Meth.*, **201**, 309 (1982).

[25] C. Y. Prescott et al, *Phys. Lett.*, **B77**, 347(1978).

[26] J. Kessler, *Polarized Electrons*, 2nd edition (Springer-Verlag, Berlin) (1985).

[27] J. Arrington et al. *Nucl. Inst. Meth.*, **A311**, 39 (1992).

[28] G. A. Warren, Massachusetts Institute of Technology, Ph.D. Thesis, unpublished (1997).

[29] K. I. Blomqvist, *MEPS Design Report*, Bates Internal Report 78-02 (unpublished) (1978).

[30] C. S. Tripp, *DCOS Operator's Manual*, RPI, (unpublished) (1993).

[31] R. S. Turley, Massachusetts Institute of Technology, Ph.D. Thesis, unpublished (1984).

[32] J. I McIntyre, G. A. Warren, *A Brief Guide to the FPP Trigger Electronics*, Bates Technical Report 94-01 (unpublished) (1994).

[33] R. W. Lourie et al. *Nucl. Inst. Meth.*, **A306**, 83–88 (1991).

[34] Group MP-6, Los Alamos National Laboratory, *Q: User Information Manual*, (1989).

[35] Application Software Group, Computing and Networks Division, CERN, *Physics Analysis Workstation: An Introductory Tutorial*, CERN Program Library Long Writeup Q121 (July, 1994).

[36] D. V. Jordan, M. Holtrop and W. Schmitt, Bates Internal Report 92-03 (unpublished) (1992).

[37] W. Bertozzi *Nucl. Inst. Meth.*, **141**, 457 (1977).

[38] S. D. Penn, Massachusetts Institute of Technology Ph.D. Thesis, unpublished (1993).

[39] J. J. Kelly, Massachusetts Institute of Technology, Ph.D. Thesis, unpublished (1981).

[40] M. Holtrop *et alia*, Interal Report B/IR 92-04, Bates Linear Accelerator Center (unpublished).

[41] K. A. Dow and M. Farkhondeh, *Magnetic Measurements of the Extraction Line and Energy Compression System Dipoles*, Bates/SHR 92-07 (unpublished).

[42] K. Jacobs, private communication.

[43] T. Zwart, private communication.

[44] T. Zwart *et alia*, A Precise Electron Beam Energy Calibration for use in Nuclear Physics, to be published.

[45] D. V. Jordan, Private Communication.

[46] L. B. Weinstein, Massachusetts Institute of Technology, Ph.D. Thesis, unpublished (1988).

[47] P. E. Ulmer, Massachusetts Institute of Technology, Ph.D. Thesis, unpublished (1981).

[48] G. A. Warren and J. I. McIntyre, Bates Internal Report 96-01, unpublished (1996).

[49] D. Besset *Nucl. Inst. Meth.*, **166**, 515 (1979).

[50] H. Arenhoevel, W. Leidmann, and E. L. Tomusiak *Phys. Rev. C*, **46**, 455 (1992).

[51] E. Aprile-Giboni et al. *Nucl. Inst. Meth.*, **215**, 147 (1983).

[52] D. Besset et al. *Nucl. Inst. Meth.*, **166**, 379 (1979).

[53] M. W. McNaughton et al. *Nucl. Inst. Meth.*, **A241**, 435 (1985).

[54] R. D. Ransome et al. *Nucl. Inst. Meth.*, **201**, 309 (1982).

[55] A. Waters et al. *Nucl. Inst. Meth.*, **153**, 401–408 (1978).

[56] R. W. Lourie et al.

[57] D. Liu, California State University, Los Angles, Master's Thesis, unpublished (1995).

[58] J. D. Jackson, Classical Electrodynamics 2nd Edition, John Wiley and Sons, New York (1975).

[59] S. Nurushev *Nucl. Inst. Meth.*, **141**, 457 (1977).

[60] L.G. Levchuk *Nucl. Inst. Meth.*, **A 345**, 496 (1994).

[61] P. E. Ulmer, *MCEEP - Monte Carlo for Electro-Nuclear Coincidence Experiments*, CEBAF-TN-91-01 (1991).

[62] A. Picklesimer and J. W. Van Orden *Phys. Rev. C*, **35**, 266 (1987).

[63] W. H. Press, B. P. Flannery, S. A. Teukolsky, W. T. Vetterling *Numerical Recipes, The art of Scientific Computing* Cambridge University Press. New York, 1990.

[64] B. H. Barkhuff, *A Spin Transport Modeler*, Bates Internal Report 97-01, unpublished (1997).

[65] A. Afanasev, private communication.

[66] A. E. Thorlacius and H. W. Fearing, *Phys. Rev. C*, **33**, 1830 (1986).

[67] L. E. Wrihgt and L. Tiator *Phys. Rev. C*, **26**, 2349 (1982).

[68] R. A. Arndt, Z. Li, L. D. Roper, R. L. Workman, and J. M. Ford *Phys. Rev. D*, **43**, 2131 (1991).

[69] L. Tiator and L. E. Wright *Nucl. Phys.*, **A379**, 407 (1982).

[70] W. E. Kleppinger and J. D. Walecka *Ann. Phys.*, **146**, 349 (1983).

[71] W. E. Kleppinger and J. D. Walecka *Ann. Phys.*, **151**, 497 (1983).

[72] J. W. Lightbody, Jr. and J. S. O'connell *Computers in Physics*, 57 (1988).

[73] J. Bellanca and R. Wilson *Proc. of the Conference in Parity Violation in Electron Scattering*, edited by E. J. Beise and R. D. Mckeown World Scientific, Singapore, 1990.

[74] H. Arenhövel, private communication.

Acknowledgements

This thesis could never have been completed without the effort and support of many individuals.

First, I would like to thank my advisor, Bill Bertozzi, for showing me his insight and ability to reach a deeper understanding of physics during my graduate career at M.I.T. It has been a pleasure and a priviledge to be his student. Even days when things were tough, he always found the right way to bring my motivation back.

I thank Robert Lourie for his leadership during the FPP experiments. Without his presence, the successful completion of the FPP experiments would not have been possible. He was always willing to explain points of confusion and answer numerous questions.

The members of the Nuclear Interactions Group at M.I.T. deserve my warm thanks. I thank Shalev Gilad for many stimulating discussions, critical questions and helpful comments. I thank Dan Dale for his patience and assistance during the tough days. I also thank Scott van Verst for his efforts of running the FPP experiments smoothly.

I acknowledge my fellow graduate students, David Barkhuff, Brian Milbrath, Justin McIntyre and Glen Warren with whom I struggled for many years to complete these experiments. I especially thank David Barkhuff and Glen Warren for discussing the physics and details of our experiments on many occasions. I also thank Christoph Mertz, Costas Vellidis and Rhett Woo for their valuable help during the experiments.

I thank Bill Donnelly and Bill Turchinetz for many interesting discussions and valuable comments.

I thank Bates staff who worked hard to deliver the polarized electron beam on target and eventually made things happen for the FPP experiments.

Lastly, I would like to express my deepest appreciation to my parents who made my dream of studying in the United States possible. They have constantly given me courage and support throughout this long journey. I thank my wife, Sooyeon, and my son, Seungjae for their everlasting love and support in the final and most difficult times.